Background Studies for the COBRA Experiment Concerning the Natural Decay Chains and ^{113}Cd

Diplomarbeit
Institut für Experimentalphysik
der Universität Hamburg

Universität Hamburg
DER FORSCHUNG | DER LEHRE | DER BILDUNG

vorgelegt von
Stefanie Kietzmann
Hamburg, November 2010

Background Studies for the COBRA Experiment Concerning the Natural Decay Chains and ^{113}Cd

Abstract

In this thesis, the background spectrum of the COBRA experiment is investigated with respect to contributions from the natural decay chains and ^{113}Cd. The COBRA experiment aims at clarifying the fundamental nature of the lightest elementary particle, the neutrino. A special focus lies on the reduction of the background signal arising from natural decay chains by the use of timing-coincidence analysis. For this purpose, datasets taken with detectors that were not flushed with nitrogen as well as datasets taken with detectors with nitrogen flushing are analyzed. The necessity for a constant nitrogen flushing system in order for the COBRA experiment to achieve the desired half-life sensitivity is demonstrated. Intrinsic contamination limits of the detectors with different isotopes arising from the natural decay chains are determined. By exploiting simulations, the intrinsic contamination limits are projected on the energy region of interest, where a possible $0\nu\beta\beta$-decay is expected. In order to enhance the efficiency of background reduction, the necessity for an improvement of the ADCs currently in use and an enrichment of the detectors with ^{116}Cd is discussed.
The analysis of the low-energy part of the spectrum provides access to the physics of the four-fold forbidden, non-unique β-decay of ^{113}Cd. A χ^2-test is performed to compare the measured spectrum to a recent theoretical model. In addition, an independent method that adjusts the model to the data by the expected event rate is introduced. Both methods independently show that the model systematically underestimates the data. The difference between the model and the data is shown to possibly arise from an additional, unidentified background source. An independent measurement with detectors enriched in ^{113}Cd in order to draw final conclusions on the correctness of the theoretical model is proposed.

Untergrundstudien für das COBRA Experiment bezüglich der natürlichen Zerfallsreihen und ^{113}Cd

Abstract

In dieser Arbeit wird das Untergrundspektrum des COBRA-Experiments untersucht. Das COBRA-Experiment soll die Natur des leichtesten Teilchens des Standardmodells, des Neutrinos, bestimmen. Der Fokus liegt auf der Reduktion des Untergrundes mittels Timing-coincidence Analyse, welcher aus Zerfällen der natürlichen Zerfallsreihen resultiert. Zu diesem Zweck werden Datensätze von Detektoren ohne Stickstoffspülung sowie Datensätze von Detektoren mit Stickstoffspülung untersucht. Die Notwendigkeit einer konstanten Stickstoffversorgung zum Erreichen der gewünschten Sensitivität auf die Halbwertszeit des $0\nu\beta\beta$-Zerfalls wird herausgestellt. Die intrinsische Kontamination der Detektoren mit verschiedenen Elementen der natürlichen Zerfallsreihen wird bestimmt. Mit Hilfe von Simulationen wird der Beitrag der intrinsischen Kontaminationen zum Energiebereich des $0\nu\beta\beta$-Zerfalls bestimmt. Um eine bessere Effizienz der Timing-coincidence Analyse zu erzielen, wird die Notwendigkeit einer Verbesserung der derzeitig verwendeten ADCs aufgezeigt und eine Anreicherung der Detektoren mit ^{116}Cd diskutiert.
Die Analyse des niederenergetischen Teils des Spektrums ermöglicht die Untersuchung des vierfach-verbotenen, non-unique β-Zerfalls von ^{113}Cd. Ein χ^2-Test wird durchgeführt, um das gemessene Spektrum mit einem theoretischen Modell zu vergleichen. Unabhängig davon wird das gemessenen Spektrum mit dem theoretische Modell verglichen, indem dies auf die erwartete Zerfallsrate normiert wird. Beide Vergleiche zeigen unabhängig voneinander, dass das Modell die Daten systematisch unterschätzt. Es wird diskutiert, dass der Unterschied zwischen Modell und Messung seinen Ursprung wahrscheinlich in einer weiteren, bisher unidentifizierten Untergrundquelle hat, dessen spektrale Form graphisch dargestellt wird. Eine Messung mit ^{113}Cd angereicherten Detektoren wird vorgeschlagen, um zu klären, ob das Modell den Zerfall akkurat beschreibt und ob Abweichungen zwischen Messung und Modell tatsächlich von einer weiteren Untergrundquelle herrühren.

Contents

Chapter 1

Introduction

Since the postulation of the neutrino by Pauli in 1930 [Pau78] and its experimental proof in 1956 by Reines and Cowan [RC56], the nature of the lightest particle in the standard model, being either a Dirac- or a Majorana-particle, has been a mystery. As the neutrino neither carries strong nor electromagnetic charge, the only channel for investigating the neutrino is the weak interaction.
In the Standard Model, neutrinos are believed to have a vanishing rest-mass. In 1957, Pontecorvo [Pon58] and in 1962, Maki, Nakagawa and Sakata [MNS62] independently proposed the existence of oscillations between the neutrino flavor eigenstates. Neutrino flavor oscillations imply a non-vanishing neutrino rest-mass without determining the absolute neutrino mass but only the squared mass differences. The existence of neutrino oscillations was investigated by several experiments and experimentally confirmed in 2001 by the SNO[1] experiment [AAA$^+$01]. The knowledge of the finite neutrino mass immediately raised the question for the nature of the neutrino, being either a Dirac- or a Majorana-particle. In the case of Dirac particles, neutrino and anti-neutrino would be two different particles whereas in the case of Majorana particles, neutrino and anti-neutrino would be two different helicity states of the same particle.
According to the Schechter-Valle theorem [SV82], the occurrence of a neutrinoless double-beta decay, which was postulated in 1939 by Furry [Fur39], always implies the Majorana-nature of the neutrino. Therefore, proving or refuting the existence of a neutrinoless double-beta decay is considered to be the "Golden Channel" for solving the two questions concerning the nature of the neutrinos and, in case of its existence, the determination of the absolute value of the neutrino masses.
In 2001, evidence for the neutrinoless double-beta decay in ^{76}Ge was claimed by a part of the Heidelberg-Moscow experiment [KKDHK01], and confirmed in 2006 [KKK06].
In order to both confirm the existence of neutrinoless double-beta decay and exclude the possibility that the signal observed by the Heidelberg-Moscow exper-

[1] **S**udbury **N**eutrino **O**bservatory

iment arose from a yet unknown, germanium-specific background, the COBRA[2] experiment has been proposed in 2001 [Zub01]. The COBRA experiment searches for neutrinoless double-beta decay with CdZnTe semiconductor detectors and is still in the Research and Development (R&D) phase. As neutrinoless double-beta decay is a rare process with an expected half-life of the order of 10^{26} years, sophisticated background reduction techniques and a complete understanding of the full energy spectrum are required in order for the experiment to succeed.
In this thesis, the method of timing-coincidence analysis is applied to the datasets taken at the LNGS[3] in Italy with four CdZnTe detectors with colorless passivation[4] during 2008 and 2009 in order to identify and reduce certain contributions from the natural decay chains to the total background spectrum. Moreover, the low-energy part of the spectrum is investigated.

In the second chapter of this thesis, a short introduction to the subject of elementary particle physics and nuclear physics is given. This is followed by a detailed description of the current setup of the COBRA experiment in chapter three. The first part of chapter four is involved with the application of timing-coincidence analysis to real datasets, showing the necessity of a nitrogen flushing system for background reduction and giving estimates and upper limits for the intrinsic contamination of the detectors with selected isotopes from the natural decay chains. A special focus lies on the bismuth isotopes ^{214}Bi and ^{212}Bi, as the major background contribution from the natural decay chains is produced by these two isotopes. The intrinsic contamination limits and the efficiency of this method are determined with the help of simulations. The second part of chapter four deals with the investigation of the low-energy part of the spectrum, which is dominated by the decay of ^{113}Cd - a fourth-forbidden, non-unique β-decay with a Q-value of 320 keV and an experimentally determined half-life of $(8.2 \pm 0.2(\text{stat})^{+0.2}_{-1.0}(\text{sys})) \cdot 10^{15}$ [GJK$^+$05] years. The spectral shape of this decay is compared to a theoretical model based on the microscopic quasiparticle-phonon model [MAS06, MAS07, MS07] using two different methods: A first comparison is performed by the use of the χ^2-method, followed by a comparison by manually adjusting the normalization of the theoretical curve to the properties of the measurement. In chapter five, a short summary of the results is given, conclusions are drawn and a future outlook is given.

[2] **C**admium-Zinc-Telluride **0**-neutrino double-**B**eta **R**esearch **A**pparatus
[3] **L**aboratori **N**azionali del **G**ran **S**asso
[4] The colorless passivation is developed by eV-PRODUCTS, its composition is kept secret

Chapter 2

Fundamentals

In this chapter, a basic introduction to elementary particle physics and nuclear physics is provided.

2.1 Elementary Particle Physics

The aim of elementary particle physics is to describe the whole variety of existing particles as compositions of only a few fundamental particles and their interactions. At the end of the 19^{th} century, the smallest indivisible particles were believed to be atoms. Rutherford modified this picture in the beginning of the 20^{th} century by proving that atoms consist of a dense nucleus surrounded by an electron cloud. The discovery of the neutron in 1932 provided the knowledge of the nucleus consisting of protons and neutrons.
In 1930, Pauli postulated the existence of an additional, uncharged particle to restore energy-, momentum- and spin-conservation during β-decay. The existence of the neutrino has been experimentally confirmed by Reines and Cowan in 1956 [RC56].
Additional particles were discovered in accelerator experiments that had similar properties as protons and neutrons. These particles were named hadrons. In 1964, the Quark-Model was proposed by Murray Gell-Mann and George Zweig [GM64] to explain similarities between the hadrons. Six fundamental particles, the quarks, were introduced, and the hadrons were found to be a combination of two (mesons) or three (baryons) of these fundamental particles. So far, no evidence for an inner structure of the quarks could be found, indicating that these particles are fundamental.
In addition, two particles with properties similar to those of the electron were found: The muon (μ) was found in 1937 by Carl D. Anderson [NA37] in cosmic rays, and the tauon (τ) was found in 1975 by Martin L. Perl in e^+e^--collisions [P^+75]. Together with the electron and the three corresponding neutrinos, these particles are called leptons [PRSZ06].

2.1.1 The Standard Model

The investigations of the past century have led to a better understanding of the structure of matter. Out of this knowledge arose the Standard Model of particle physics. The Standard Model of particle physics describes the properties of the leptons and quarks and the interactions that they are subject to, with the exception of gravity. Both leptons and quarks are spin-1/2 particles and therefore Fermions. They can – depending on their type – undergo up to four different types of interactions. One of these is gravitation, which does not play a role in the subatomic range due to its weakness compared to the other interactions [PRSZ06] and will therefore not be discussed. The other three interactions are listed in Table 2.1. They are carried out by vector bosons which carry spin 1. Particles are

Table 2.1: The three fundamental interactions of the Standard Model [PRSZ06].

Interaction	Charge	Mediator	Mass (GeV/c^2)
Strong	Color	8 gluons	0
Electromagnetic	Electromagnetic	Photon (γ)	0
Weak	Weak	$W^{\pm}$, Z^0	80 / 91

subject to an interaction if they carry the corresponding charge. The interaction understood best is the electromagnetic interaction. The vector bosons that are exchanged in electromagnetic interaction are photons. All particles that carry electromagnetic charge can undergo electromagnetic reactions. According to Tab. 2.1, all of the quarks and three out of six leptons carry electromagnetic charge. Photons do not carry electromagnetic charge and therefore do not interact with each other. Moreover, photons have a vanishing rest mass and the range of the electromagnetic interaction is infinite.
In the case of weak interaction, the charge of the participating particles is the weak charge. According to Tab. 2.1, all fundamental fermions (quarks and leptons) participate in the weak interaction. In contrast to the electromagnetic interaction, the bosons of the weak interaction, $W^{\pm}$ and Z^0, are weakly charged themselves. Therefore, they show interactions among each other. Moreover, the bosons of the weak interactions have a large mass of $m_{W^{\pm}} = 80\,GeV/c^2$ and $m_{Z^0} = 91\,GeV/c^2$. Consequently, the range of the weak interaction is limited to distances below 10^{-3} fm [PRSZ06].
The theory of the strong interaction is called quantumchromodynamics. The strong interaction is carried out by Gluons. Gluons couple to color charge, therefore only quarks can undergo strong interaction since leptons do not exhibit color charge (see Table 2.2). The Gluons carry color charge themselves and therefore interact with themselves. Even though Gluons have a vanishing rest-mass, their range is still limited to distances as small as 1 fm due to confinement: At a distance of about 1 fm, the energy carried out by the color field, which grows with

increasing distance, becomes large enough to generate quark anti-quark pairs. Due to this process, the isolation of single quarks is impossible.

The leptons and quarks are subdivided into families with increasing particle masses. The lepton and quark families are shown in Table 2.2 [PRSZ06]. There

Table 2.2: Leptons and quarks in the Standard Model along with their properties such as electromagnetic and color charge and spin [PRSZ06].

Fermions	Family 1 2 3	Electromagnetic Charge	Spin	Color
Leptons	ν_e ν_μ ν_τ e μ τ	0 -1	1/2	—
Quarks	u c t d s b	+2/3 -1/3	1/2	r, b, g

are six leptons in total: The three leptons that carry electromagnetic charge are the electron e, the muon μ and the tauon τ. The remaining three leptons are the corresponding neutrinos ν_e, ν_μ, ν_τ which do not carry electromagnetic charge. Additionally, six quarks exist: The up (u) quark, down (d) quark, charm (c) quark, strange (s) quark, top (t) quark and bottom (b) quark. Every quark carries one out of three color charges (**r**ed, **g**reen, **b**lue) due to strong interaction that ensures the validity of Pauli's principle for the quarks inside the hadrons: Hadrons consist of either two or three quarks to guarantee color charge neutrality. Hadrons consisting of two quarks are called mesons, those consisting of three quarks are named baryons. Pauli's Principle forbids an overlap of the wave functions of two or more fundamental particles with exactly the same quantum numbers. Accordingly, a hadron can only consist of several quarks of the same type if these quarks differ in at least one quantum number. This quantum number is the color charge.
Table 2.3 shows the weak isospin T of the Fermions in the Standard Model. In the formalism of the weak isospin, every family of left-handed leptons and quarks is described as Isospin-doublet of Fermions that can transfer into each other by the exchange of a charged W-boson. Accordingly, the electromagnetic charge e of the two states of each weak isospin doublet differs by one unit. Each left-handed fermion and each right-handed anti-fermion is assigned the weak isospin T=1/2, with the third component $T_3 = \pm 1/2$. Until now, only neutrinos with a positive third component of the isospin have been observed. Accordingly, the charged leptons that participate in the weak interaction have a negative third component of the isospin. Right-handed anti-fermion-doublets have the opposing sign of T_3 and electromagnetic charge compared to the corresponding fermion-doublets. As right-handed fermions and left-handed anti-fermions do not participate in the weak interaction and therefore do not couple to W-bosons, they are described

as weak isospin singlets with $T=T_3=0$ [PRSZ06]. The weak isospins of the fermion-doublets and singlets are shown in Table 2.3. The quarks d', s' and b'

Table 2.3: Fermion-multiplets in the weak isospin formalism with the accordant weak isospin T, the third component of the weak isospin T_3 and the electromagnetic charge z_f [PRSZ06]. As no right-handed neutrinos have been observed, they are assumed not to have a right-handed weak isospin. The remaining Fermions form right-handed isospin singlets with T=0 as they do not participate in the weak interaction.

Fermion-multiplets			T	T_3	z_f
$\begin{pmatrix} \nu_e \\ e \end{pmatrix}_L$	$\begin{pmatrix} \nu_\nu \\ \mu \end{pmatrix}_L$	$\begin{pmatrix} \nu_\tau \\ \tau \end{pmatrix}_L$	1/2	+1/2 -1/2	0 -1
e_R	μ_R	τ_R	0	0	-1
$\begin{pmatrix} u \\ d' \end{pmatrix}_L$	$\begin{pmatrix} c \\ s' \end{pmatrix}_L$	$\begin{pmatrix} t \\ b' \end{pmatrix}_L$	1/2	+1/2 -1/2	+2/3 -1/3
u_R	c_R	t_R	0	0	+2/3
d'_R	s'_R	b'_R	0	0	-1/3

are the Cabbibo-rotated quarks due to a mixing of the quark eigenstates in the weak interaction. As the weak interaction does not exactly conserve the quark family, the quark eigenstates d, s and b are not the "weak interaction partners" of the quark eigenstates u, c and t. Instead, linear combinations of those three quark eigenstates, named d', s' and b', are the weak interaction partners of u, c and t. d', s' and b' can be determined by multiplying the three quark generations with the Cabbibo-Kobayashi-Maskawa matrix u. Its elements U_{ij} describe the transition probability from one quark q_i into another quark q_j.
A strong isospin, I, can be defined analogously to the weak isospin T. The operator of the strong isospin transforms quarks within one quark family into each other. Accordingly, d, s and b are the exact interaction partners of u, c and t in the strong interaction. Cabbibo-rotation of the weak isospin operator yields the strong isospin operator.

2.1.2 Conservation Laws

According to Noether's theorem, every invariance of a system under certain coordinate transformations results in a conserved quantity [Kuy05]. In classical physics, homogeneity in time results in energy conservation, invariance under translation results in momentum conservation and rotational invariance causes angular momentum conservation [Kuy05]. In non-relativistic quantum mechanics, invariance

under mirror imaging is added to the classical continuous coordinate transformations. Invariance under mirror imaging causes conservation of a new quantity called parity P. Mathematically, parity indicates the behavior of the wave function under a flip of the sign of its spatial coordinate. A change in the sign of the wave function assigns a negative parity to the wave function, no change in its sign assigns a positive parity to the wave function. In interactions, parity is conserved if the transition matrix element solely consists of either vectors or axial vectors. A superposition of both, as it occurs in the weak interaction results in a violation of parity. The relativistic quantum mechanics assign an intrinsic parity to every particle and antiparticle. Complex many-body systems such as hadrons or even nuclei have a well-defined parity if their components have well-defined parities. In that case, the parity P of the many-body system is a product of the parities p_i of its j components:

$$P = (-1)^l \prod_{i=1}^{j} p_i. \tag{2.1}$$

The term $(-1)^l$ accounts for the angular momentum of the many-body system. The charge conjugation operator C is introduced to describe the transformation of a particle into its own antiparticle. The previously mentioned weak isospin is another example of a quantity that is conserved in the weak interaction. Moreover, a quantum number called strangeness S is assigned to the strange quark and a quantum number called charm C is assigned to the charm quark. Baryons have a quantum number called baryon number B which is 1 for baryons and -1 for antibaryons. The lepton families have lepton family numbers, L_e, L_μ and L_τ and a total lepton number of $L = L_e + L_\mu + L_\tau$.
Not all interactions of the Standard Model conserve all quantum numbers. The quantum numbers that are conserved in all interactions are energy, momentum, angular momentum, charge, baryon number and, the lepton family numbers and the total lepton number. Additionally, the strong and the electromagnetic interaction conserve the parity, the C-parity (charge conjugation) and the product of both, the CP-parity as well as the third strong isospin component, strangeness and charm of the quarks. Solely the strong interaction conserves the absolute value of the strong isospin I. Table 2.4 shows a summary of the conservation laws with respect to weak, strong and electromagnetic interactions.
The CPT-parity, which is a product of CP-parity and the Time-operator, is conserved in all known interactions.

2.1.3 The Weak Interaction

Weak interactions can take place by the exchange of an electromagnetically charged boson - the $W^{\pm}$-boson, or by the exchange of an electromagnetically neutral boson - the Z^0-boson. If a $W^{\pm}$-boson is exchanged, the process is called charged current weak interaction. In that case, an electromagnetic charge of $\pm 1e$ is exchanged and

Table 2.4: Conservation laws that are fulfilled by the strong, weak and electromagnetic force in the Standard Model [PRSZ06].

	Strong	Electromagnetic	Weak
Energy E, Momentum **p**, Angular Momentum **L**, Charge Q	✓	✓	✓
Baryon Number B, lepton family Numbers L_e, L_μ, L_τ	✓	✓	✓
Parity P, C-Parity C	✓	✓	XX
CP-Parity CP	✓	✓	XX
CPT-parity	✓	✓	✓
3^{rd} component of Isospin I_3	✓	✓	XX
Strangeness S, Charm C	✓	✓	XX
Strong Isospin I	✓	XX	XX

the identity of the involved quarks or leptons is changed during the interaction process. Three types of charged current weak interactions are possible: Leptonic processes, where no quarks are involved, semileptonic processes, with the involvement of a combination of quarks and leptons and non-leptonic processes, which occur without leptons. The weak interaction is usually illustrated by the use of Feynman-diagrams. The real particles are described as solid lines, the interaction is carried out by a virtual interaction boson illustrated as dashed line. Figure 2.1 shows Feynman-diagrams for the three possible types of a charged current weak interaction.

In addition to the charged current weak interaction, neutral current weak interaction is possible. In that case, no electromagnetic charge is exchanged and the identity of the involved quarks and leptons is not changed. This type of weak interaction is carried out by an electromagnetically neutral boson, the Z^0, that was discovered in 1973 at CERN[1] [Sci79].

The strength of the weak interaction is parametrized by the Fermi-constant G_F. G_F is proportional to the squared weak charge g, analogously to the coupling constant of the electromagnetic interaction α, which is proportional to the electromagnetic charge e [PRSZ06]

$$\alpha = \frac{e^2}{4\pi\epsilon_0\hbar c}\,. \tag{2.2}$$

Accordingly, G_F is associated with the weak charge g as follows [PRSZ06]

$$\frac{G_F}{\sqrt{2}} = \frac{\pi\alpha}{2}\cdot\frac{g^2}{e^2}\cdot\frac{\hbar c^3}{M_W^2 c^4}\,, \tag{2.3}$$

[1] **C**onseil **E**uropéen pour la **R**echerche **N**ucléaire, located in Geneva, Switzerland

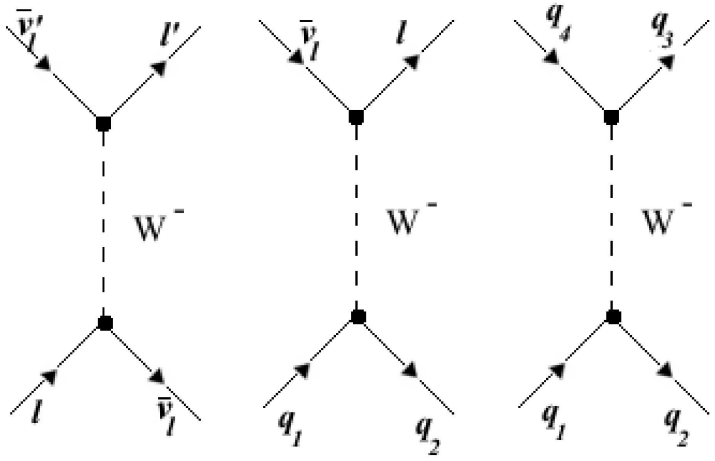

Figure 2.1: Feynman diagrams for processes with charged current. Left: Lepton process, middle: semileptonic process, right: non-leptonic process [PRSZ06].

where M_W is the mass of the $W^{\pm}$-boson. The weak charge g and the electromagnetic charge e are of the same order of magnitude. Nevertheless, the weak interaction is much weaker and has a very short range of only $\approx 2.5 \cdot 10^{-3}$ fm. The reason for this becomes clear by regarding the propagator contained in the transition matrix element M_{fi} [PRSZ06] as it appears in Fig. 2.1

$$M_{fi} \propto g \cdot \frac{1}{Q^2c^2 + M_W^2c^4} \cdot g \overset{Q^2 \to 0}{\longrightarrow} \frac{g^2}{M_W^2c^2}\,, \tag{2.4}$$

where Q^2 is the momentum transfer. In case of a small momentum transfer, the propagator of the weak interaction approaches the constant value $\frac{g^2}{M_W^2c^2}$. This explains the different behavior of the electromagnetic interaction: As the interaction boson of the electromagnetic interaction has a vanishing rest mass, the propagator is $(Qc)^{-2}$, which grows to infinity with vanishing Q.
The weak interaction does not conserve parity. The transition-matrix elements contain both a vector and an axial vector contribution that are described by the coefficients c_v and c_a. Experimentally it is found that the absolute values of the coefficients are equal, with opposing signs: $c_v = -c_a$. Accordingly, the weak interaction is considered to be a (V-A)-theory [Sch97]. A new quantum number, the chirality, is introduced by this theory, with the eigenstates "right-handed" and "left-handed". As a result of (V-A)-calculations, only left-handed fermions and right-handed anti-fermions participate in the weak interaction. Therefore, they are assigned the weak isospin T=1/2. The left-handed fermions and right-handed anti-fermions are assigned the weak isospin T=0. Up to now, no evidence for right-handed neutrinos and left-handed anti-neutrinos could be found. This indicates that the weak interaction actually only couples to left-handed fermions

and right-handed anti-fermions, confirming the weak interaction to be accurately described by the (V-A)-theory, resulting in maximum parity violation.

The electromagnetic and the weak interaction can be considered as two different aspects of the same interaction. In the electroweak unification, the interaction bosons of the weak and the electromagnetic interaction are described as two states consisting of two orthogonal linear combinations of a neutral W-boson, the W^0, and a newly postulated boson, B^0, which is a singlet state of the weak isospin T ($T = 0$, $T_3 = 0$). As a result, the weak charge g is related to the electromagnetic charge e by an angle Θ_W, which is called Weinberg angle:

$$e = g \cdot \sin \Theta_W. \tag{2.5}$$

From scattering experiments [ABD+87], the ratio of the $W^{\pm}$ and Z^0 and the decay width of the Z^0 the Weinberg angle has been determined to be $\sin^2 \Theta_W$=0.23116±0.00013 [N+10].

2.1.4 Physics of Neutrinos

Neutrinos are the only fermions in the Standard Model that do not carry electromagnetic charge. In addition, they do not interact strongly. Therefore, the only way of detecting neutrinos is the investigation of weak interactions. Neutrinos have a very small cross-section for scattering processes, which makes their detection difficult. Accordingly, it is not surprising that it took over 20 years for the electron-neutrino from its postulation in 1930 to its experimental prove by Reines and Cowan in 1956 [RC56]. In 1952, a first evidence for the electron neutrino was claimed by [RA00]. They investigated the electron capture (EC) process of ^{37}Ar [Zub04]

$$^{37}\mathrm{Ar} + \mathrm{e}^- \rightarrow {}^{37}\mathrm{Cl} + \nu_\mathrm{e} + \mathrm{Q}, \tag{2.6}$$

which has a Q-value of 816 keV and a fixed recoil energy of the nucleus being 9.67 eV because only two particles are contained in the final state. They measured the time difference between the detection of the Auger electron that starts the electron capture process and the detection of the recoiled nucleus, determining a velocity of the nucleus of 0.71cm/μs. Measuring a fixed recoil energy of the nucleus proved that two particles must be contained in the final state. The second particle was the neutrino. The final discovery of the anti-electron neutrino could be achieved by [RC56] with the help of the Savannah River nuclear reactor. They detected the reaction

$$\overline{\nu}_\mathrm{e} + \mathrm{p} \rightarrow \mathrm{e}^+ + \mathrm{n}, \tag{2.7}$$

by measuring the annihilation photons of the positron and a neutron capture within a few μs [Zub04] using a water tank with dissolved $CdCl_2$ surrounded by liquid scintillators. Interactions including electron-neutrinos are also possible

$$\nu_\mathrm{e} + \mathrm{n} \rightarrow \mathrm{e}^- + \mathrm{p}, \tag{2.8}$$

In 1962, the existence of the muon-neutrino has been proven by [DGG+62] in the Brookhaven National Laboratory, followed by the discovery of the tau-neutrino in 2000 [Hos00] at Fermilab.
The number of neutrino flavors (e, μ, τ) can be determined from the decay width of the Z^0-boson [Zub04]. It has been found that only three light neutrinos exist [Lan95, CG98]. The Z^0-boson decays into a fermion anti-fermion pair. Every neutrino anti-neutrino pair contributes 165.8 MeV to the Z^0 decay width. The decay channel is equal for all flavors. Moreover, each of the the three existing quark anti-quark pairs occurring in three different color-charge combinations and the electromagnetically charged leptons make a known contribution to the Z^0 decay width. Accordingly, the Z^0 decay width was calculated by [Lan95] assuming three different neutrino flavors

$$\Sigma_{\text{tot}}^{\text{theo}} = (2496 \pm 7)\,\text{MeV}. \tag{2.9}$$

Experimentally it has been verified by [CG98]

$$\Sigma_{\text{tot}}^{\text{exp}} = (2490 \pm 7)\,\text{MeV}. \tag{2.10}$$

The same calculations have been performed assuming two and four neutrino flavors. The results are depicted in Fig. 2.2. Also shown are the measured values from the ALEPH[2] detector at LEP[3], CERN. The measurements perfectly agree with the theoretical predictions for three neutrino flavors [ALE], yielding a number of

$$\text{N}_\nu = 2.982 \pm 0.013\,. \tag{2.11}$$

2.1.4.1 Neutrino-Flavor Oscillations

In the Standard Model, neutrinos are assumed to have a vanishing rest mass, which could not be refuted by direct experiments so far. In 1957, Pontecorvo theoretically predicted the existence of neutrino oscillations between the flavor eigenstates [Pon58]. Independently, this prediction was made in 1962 by Maki, Nakagawa and Sakata [MNS62]. Oscillations between the neutrino flavor eigenstates requires a non-vanishing rest mass of the neutrinos, because every mixture of neutrinos would be an eigenstate of the mass operator in the case of massless neutrinos. Accordingly, a basis consisting of three mass eigenstates, $|\nu_1\rangle$, $|\nu_2\rangle$ and $|\nu_3\rangle$, could be defined such that the eigenstates exactly coincide with the neutrino flavor eigenstates, $|\nu_\text{e}\rangle$, $|\nu_\mu\rangle$ and $|\nu_\tau\rangle$. In that case, no neutrino oscillations would be found.

[2] **A**pparatus for **LE**P **Ph**ysics
[3] the large electron-position collider at CERN

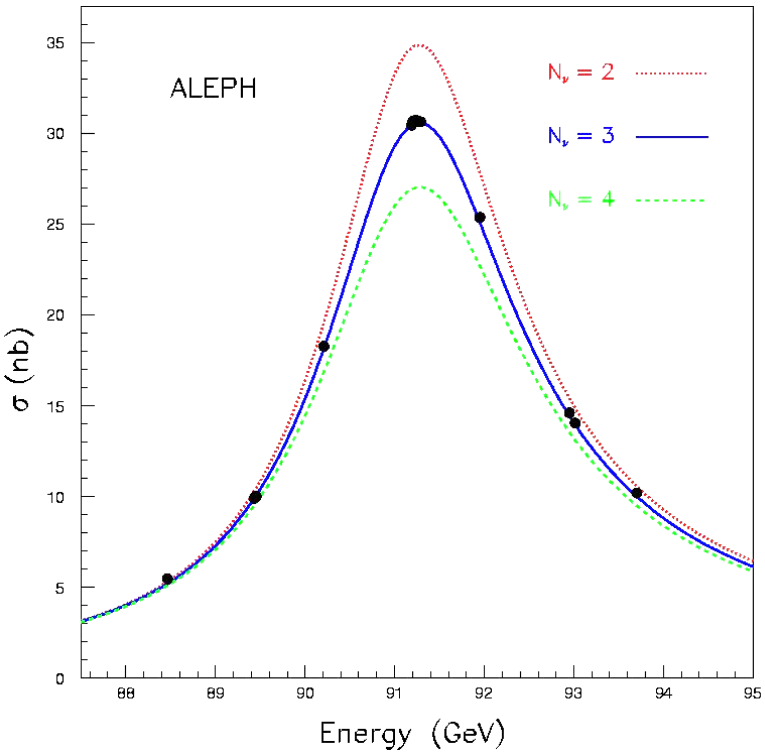

Figure 2.2: Cross section of the reaction $e^+e^- \rightarrow$ hadrons close to the Z^0 resonance. Shown are the theoretical prediction assuming two (red), three (blue) and four (green) different neutrino flavors together with the measured value from the ALEPH experiment located at LEP, CERN [ICC]. The experimental values perfectly agree with the theoretical predictions for three neutrino flavors.

The question of neutrino oscillations was answered in 2001 by the SNO[4] experiment [AAA+01] located near Sudbury, Ontario, Canada, where solar neutrinos were detected via the charged current reaction on deuterium and by elastic scattering of electrons. In solar reactions, only electron neutrinos are produced, but the SNO experiment detected an active non-electron neutrino flux. However, the total neutrino flux they measured was in agreement with the predictions of solar models, indicating that the solar models are correct. Moreover, oscillations have been detected in the atmospheric neutrino flux by the Super-Kamiokande-detector [FFI+01] in Kamioka, Japan. The Super-Kamiokande detector consists of a tank filled with 50000 t of ultra pure water, with 11200 photomultipliers to detect Čerenkov-radiation of free electrons and muons that occur in atmospheric neutrino interactions with the water. A third possibility to observe neutrino flavor oscillations is the observation of nuclear reactors. This was done by the Kam-

[4] **S**udbury **N**eutrino **O**bservatory

LAND detector located in Kamioka [SKD]. Moreover, neutrino oscillations of neutrinos that are produced in nuclear reactors are investigated, for example by the CNGS[5]-experiment that is located in the Gran Sasso underground laboratory and investigates a muon-neutrino beam that is produced in the SPS[6]-accelerator at CERN. All these experiments proved that neutrinos have a non-vanishing rest-mass and the neutrino flavor eigenstates are a superposition of the neutrino mass eigenstates [PRSZ06]. The existence of oscillations between the neutrino flavors represents a violation of the lepton family numbers L_e, L_μ and L_τ. Analogously to the quark mixing in the weak interaction, this mixing of neutrino flavors is described by a mixing matrix U, with the matrix elements U_{ij}, that shows the relation between the neutrino-flavor eigenstates with the neutrino mass eigenstates. The neutrino oscillations do not depend on on the absolute neutrino masses, but on the squared difference between them (Δm^2_{21} and Δm^2_{32}). Accordingly, at least two of the neutrinos must have a non-vanishing rest mass in order for the oscillations to occur. The most recent results on the squared mass differences are [MS10]

$$\Delta m^2_{21} = (m_2 - m_1)^2 = 7.59^{+0.23}_{-0.18} \cdot 10^{-5}\,\mathrm{eV}^2, \tag{2.12}$$

and

$$\Delta|m^2_{32}| = |(m_3 - m_2)^2| = 2.40^{+0.12}_{-0.11} \cdot 10^{-3}\,\mathrm{eV}^2. \tag{2.13}$$

Finite rest masses of the neutrinos raise some fundamental questions: In the Standard Model, neutrinos are assumed to have a vanishing rest mass. In this case, there would be no possibility to determine whether neutrinos are Dirac-particles, which means that particle and antiparticle are two different elementary particles, or Majorana-particles, meaning that anti-neutrino and neutrino are two aspects of the same particle. A finite rest mass of the neutrinos opens the possibility to investigate this question.
For massless particles, the helicity H, which describes the projection of the particle spin on the direction of its momentum, is a good quantum number instead of the spin

$$\mathrm{H} = \frac{\mathbf{s} \cdot \mathbf{p}}{|\mathbf{p}|}\,. \tag{2.14}$$

In the case of particles with a finite rest mass, the particle velocity is slower than the speed of light. Therefore, the helicity of a particle depends on the reference frame from which it is observed. Accordingly, a left-handed fermion, for example a neutrino, would have a small right-handed component. Usually, particles and antiparticles carry opposite electromagnetic charge. As neutrinos do not carry electromagnetic charge, it is still an open question whether the right-handed component of the neutrino is an anti-neutrino and vice versa. This question shall be answered by the investigation of the neutrinoless double-beta decay which will be

[5] **C**ERN **N**eutrinos to **G**ran **S**asso
[6] **S**uper **P**roton **S**ynchrotron

described in section 2.2.4.2. So far, no prove could be adduced for the neutrinos to be Majorana-particles. The anti-neutrinos that are produced during β-decay,

$$\mathrm{n} \rightarrow \mathrm{p} + \mathrm{e}^- + \overline{\nu_\mathrm{e}}\,, \tag{2.15}$$

only interact with protons

$$\overline{\nu_\mathrm{e}} + \mathrm{p} \rightarrow \mathrm{n} + \mathrm{e}^+. \tag{2.16}$$

A reaction of the anti-electron neutrinos with neutrons,

$$\overline{\nu_\mathrm{e}} + \mathrm{n} \nrightarrow \mathrm{p} + \mathrm{e}^-, \tag{2.17}$$

which should occur with the same rate as Eq. 2.16 if neutrinos and anti-neutrinos are identical particles, has not been observed. This is due to that anti-neutrinos are right-handed, whereas the electron is left-handed. If the anti-neutrinos have a non-vanishing left-handed component, it is very small, resulting in a strong suppression of the interaction 2.17.

2.2 Nuclear Physics

Atomic nuclei consist of protons and neutrons. The charge number Z of each nucleus is determined by the number of contained protons and defines the chemical element. An equal number of electrons in the atomic shell compensates the charge of the protons within the nucleus such that every atom is electromagnetically neutral. The number of neutrons inside the nucleus, N, and the charge number Z add up to the mass number A of the nucleus: A=N+Z. Isotopes are defined by the number of neutrons and protons within the nucleus. The energy that attaches the nucleons to the nucleus is called binding energy B and is given by the difference between the total mass of the nuclei, $\mathrm{ZM}(^1\mathrm{H}) + (\mathrm{A}-\mathrm{Z})\mathrm{M_n}$, and the mass of the nucleus, M(A, Z) [AW93]

$$\mathrm{B(Z,A)} = (\mathrm{ZM}(^1\mathrm{H}) + (\mathrm{A}-\mathrm{Z})\mathrm{M_n} - \mathrm{M(A,Z)}) \cdot \mathrm{c}^2, \tag{2.18}$$

$^1\mathrm{H} = \mathrm{M_p} + \mathrm{M_e}$ is the mass of a hydrogen atom, $\mathrm{M_p} = 938.272\,\mathrm{MeV/c^2}$ is the proton mass and $\mathrm{M_n} = 939.566\,\mathrm{MeV/c^2}$ is the neutron mass. M(A,Z) is the mass of the atom containing Z protons and N neutrons and can be determined using the semi empiric Weizsaecker mass-formula [Wei35, BB36]:

$$\begin{aligned} \mathrm{M(A,Z)} \;=\; & \mathrm{N\,M_n} \,+\, \mathrm{Z\,M_p} \,+\, \mathrm{Z\,m_e} \,+\, \mathrm{a_v\,A} \,+\, \mathrm{a_s\,A^{2/3}} \\ & + \mathrm{a_c}\,\frac{\mathrm{Z^2}}{\mathrm{A^{1/3}}} \,+\, \mathrm{a_a}\,\frac{(\mathrm{N}\,-\,\mathrm{Z})^2}{4\mathrm{A}} \,+\, \frac{\delta}{\mathrm{A^{1/2}}}\,. \end{aligned} \tag{2.19}$$

The parameters δ and $\mathrm{a_i}$ (i=v,s,c,a) depend on the atomic mass. The individual terms account for the number of nucleons (volume term $\mathrm{a_v}$), surface effects ($\mathrm{a_s}$), the Coulomb-repulsion between the protons ($\mathrm{a_c}$), the asymmetry of neutrons and

protons (for N-Z>0, a_a) and the fact that an even number of protons and neutrons maximizes the stability of the nucleus (pairing-term δ)

$$\delta = \begin{cases} -11,2\,\mathrm{MeV/c^2}, & \text{for even N and even Z (ee-nuclei)} \\ 0, & \text{for uneven A} \\ +11,2\,\mathrm{MeV/c^2}, & \text{for odd N and odd Z (oo-nuclei).} \end{cases} \tag{2.20}$$

In the following section, different models will be introduced in order to describe the energy states of nuclear transitions.

2.2.1 The Fermi-Gas Model

For heavy nuclei, the ground state of the nucleus can be described as degenerate Fermi gas. Due to the uncertainty principle, the particles are not localized within the nucleus but show a movement as quasi-free particles with a rather large momentum of $\simeq 250\,\mathrm{MeV/c}$. The nuclear density is determined as a compromise between the repulsion of the particles at very small distances due to Pauli's principle that is very strong compared to the Coulomb-repulsion between the protons and an attraction at larger distances due to the strong interaction. In the Fermi gas model, the protons and neutrons within the nucleus are regarded as two independent nucleon-systems that individually obey the Fermi-Dirac-Statistics. While obeying Pauli's principle, the nucleons are assumed to be free particles throughout the volume of the nucleus. Every nucleon is exposed to the superposition of the potentials arising from the other nucleons, which is assumed to be a square-well potential, being constant throughout the whole nucleus with sharp borders at the edges. Accordingly, the number of available states within the volume V and the momentum interval dp is given by [PRSZ06]

$$\mathrm{dn} = \frac{4\pi \mathrm{p}^2 \mathrm{dp}}{(2\pi\hbar)^3} \cdot \mathrm{V}. \tag{2.21}$$

In the ground state of the nucleus, all the lowest momentum states are occupied, up to a maximum momentum, the Fermi-momentum p_F, which is equal for protons and neutrons, $p_F \approx 250\,\mathrm{MeV/c}$. This corresponds to a Fermi-energy of $E_F \approx 33\,\mathrm{MeV/c^2}$. As the binding energy per nucleon B is 7-8 MeV for all heavy nuclei, the Fermi-energy also defines the depth of the square well, being $V_0 = E_F + B \approx 40\,\mathrm{MeV/c^2}$. The nucleus behaves like a free nucleon gas with a kinetic energy in the same range as the depth of the potential square well. If the Fermi levels of the protons and neutrons within a nucleus are not equal, the nucleus would decay into an energetically favorable state via β-decay (for information on β-decays see section 2.2.3). For heavy nuclei, the depth of the square well for a neutron gas is larger than that for a proton gas as a result of the Coulomb rejection between the protons. Accordingly, stable heavy nuclei contain more neutrons than protons.

From the nuclear potential, the total kinetic energy of the nucleons can be determined. Developing the total kinetic energy of the nucleus in a Taylor-series around (Z-A) yields the volume-term and the asymmetry-term in Eq. 2.19.

2.2.2 The Shell Model of the Nucleus

The shell model is based on the assumption that every nucleon occupies well-defined energy-states within the nucleus which results in discrete energy levels, analogously to the atomic-shell model. The shell model is only applicable to nuclei in the ground state or in slightly excited states, as the Fermigas-model is based on the assumption of non-interacting particles. In contrast to the atomic-shell model, the nuclei do not move within a central Coulomb potential but within a potential that is created by the other nuclei. A global nuclear potential is introduced, that can be approximated as a harmonic oscillator for very light nuclei ($A \lesssim 7$). For heavy nuclei, the shape of the potential should correspond to the nuclear density distribution due to the short range of the strong interaction. In the case of heavy nuclei, the nuclear potential is usually described by the Woods-Saxon-Potential [WS54]

$$V(r) = \frac{-V_0}{1 + e^{(r-R)/a}} \,. \tag{2.22}$$

R is the radius of the potential well and a is a parameter that describes the boundary uncertainty of the nucleus [MK84]. As the Woods-Saxon potential (Eq. 2.22) is a central potential, the wave function of the particles within the nucleus can be separated into a spherical part $Y_l^m(\theta, \phi)$ that only depends on the angle and a radial part $R_{nl}(r)$ that only depends on the radius, analogously to the atomic shell model. Energy levels are filled according to Pauli's principle. Analogously to the atomic shell model, nuclides with a certain number of protons and neutrons are particularly stable ("magic numbers"). The appearance of these magic numbers can only be explained by the nuclear shell model. The main quantum number is n, a non-negative integer. The angular momentum is described by l. The energy levels are degenerate with respect to the quantum number m, which is an integer between -l and l. In contrast to light nuclei, states with different nl are not degenerate for heavy nuclei due to spin-orbit coupling: Those states with a smaller n and larger l are located at lower energies. In contrast to the atomic shell model, the spin-orbit-coupling has a large effect on the position of the energy levels. The separation of the energy levels due to spin-orbit-coupling is of the same order of magnitude as the separation of the energy levels due to the different shells [PRSZ06]. The energy level with total angular momentum $j = l + 1/2$ is lower that that of $j = l - 1/2$. This is particularly surprising because in the atomic-shell model, the energy level with total angular momentum $j = l + 1/2$ is higher than that of $j = l - 1/2$. This is due to the sign of the spin-orbit coupling potential, which has been determined to be negative for nuclei [PRSZ06].
The nuclear shell model yields a good approximation for nuclei with completely or

almost completely filled shells. Otherwise, the nuclear potential cannot assumed to be spherical, requiring a description for deformed nuclei with a non-spherical potential.

2.2.3 Phenomenology of the β-Decay

Energetically, β-decay is always possible as long as the following condition holds

$$\mathrm{M(A,Z)} > \mathrm{M(A,Z-1)} + 2\,\mathrm{m_e}. \tag{2.23}$$

If this condition is not fulfilled, but the energy of the mother nucleus is larger than the sum of the energy of the daughter nucleus and the excitation energy ϵ of an electron in the atomic shell,

$$\mathrm{M(A,Z)} > \mathrm{M(A,Z-1)} + \epsilon, \tag{2.24}$$

the nucleus can undergo electron capture processes, where an electron from the atomic shell is captured by a proton within the nucleus, releasing a neutron and an electron neutrino according to

$$\mathrm{p} + \mathrm{e}^- \overset{\mathrm{EC}}{\rightarrow} \mathrm{n} + \nu_\mathrm{e}. \tag{2.25}$$

During β-decay, a nucleon is transferred into a nucleon with different charge number Z under the emission of an electron or a positron and a concomitant neutrino or anti-neutrino. The term β-decay therefore describes one of the following processes [MK84]

$$\mathrm{n} \rightarrow \mathrm{p} + \mathrm{e}^- + \overline{\nu}_\mathrm{e}, \tag{2.26}$$

$$\mathrm{p} \rightarrow \mathrm{n} + \mathrm{e}^+ + \nu_\mathrm{e}. \tag{2.27}$$

The decay in Eq. 2.26 also occurs in free neutrons with a half-life of 10.6 min. The decay in Eq. 2.27 can only take place within a nucleus due to the larger mass of the neutron compared to the proton. The additional energy is provided by the binding energy that bonds the proton to the nucleus. The decay probability is determined with the help of Fermi's Golden Rule

$$\mathrm{W} = \frac{2\pi}{\hbar}|M_{fi}|^2 \cdot \rho(\mathrm{E}), \tag{2.28}$$

W is the reaction rate per target particle, M_{fi} is the transition matrix element and ρ is the density of the final states at the energy E. Accordingly, the decay rate for β-decays of free neutrons, emitting an electron at energy $\mathrm{E_e}$ is

$$\mathrm{dW(E_e)} = \frac{2\pi}{\hbar}|M_{fi}|^2 \cdot \frac{d\rho_f(\mathrm{E_0,E_e})}{\mathrm{dE_e}}\mathrm{dE_e}, \tag{2.29}$$

with $\frac{d\rho_f(\mathrm{E_0,Ee})}{\mathrm{dE_e}}$ being the density of anti-electron neutrino final-states with total energy $\mathrm{E_0}$=$\mathrm{E_e}$+$\mathrm{E_r}$ ($\mathrm{E_r}$ is the recoil energy of the remaining nucleus).

Not only free but also bound nucleons within a nucleus can undergo β-decay. Depending on the mass number A of the investigated isobars[7] being either even or odd, two different cases arise: According to Eq. 2.18, the mass of the nucleus is proportional to the squared charge number Z: $m(A,Z) \sim Z^2$. Accordingly, illustrating the behavior of the mass with changing charge number yields a parabola for odd mass numbers. Regarding even-A nuclei[8] yields two parabolas, as the pairing-energy δ (defined in Eq. 2.20) is different for ee- and oo-nuclei[9]. These parabolas are illustrated in Fig. 2.3. A β-decay always occurs if there

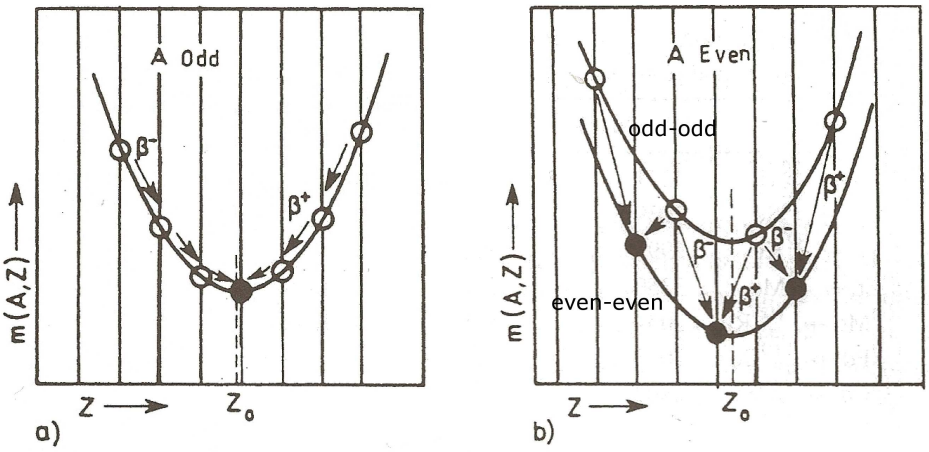

Figure 2.3: Mass of isobars with varying Z. Filled circles indicate stable isotopes while unfilled circles denote unstable isotopes. Odd-A nuclei only form one parabola, therefore only one stable state exist. Even-A nuclei split up in two parabolas, depending on whether the numbers or protons and neutrons are even or odd due to the pairing energy δ. As several even-even isotopes of the same isobar can have energetically lower states than the lowest odd-odd state, several stable states are possible [Zub04].

is a neighboring state that is energetically favorable. In practice this means for odd-odd even-A nuclei that no stable states exist because the even-even parabola is energetically favorable. When an even-A isobar decays via β-decay, an even-even nucleus is transformed into an odd-odd nucleus and vice versa. Accordingly, a β-decay of even-A isobars causes a transition from one isobar parabola to the other. Therefore, more than one β-stable state is possible because several even-even isobars can occupy a state that is energetically more favorable than the lowest odd-odd state, as illustrated in Fig. 2.3.

[7] isobars are nuclei with equal mass number A

[8] nuclei with an even mass number

[9] ee stands for even-even, oo for odd-odd, meaning the number of protons and neutrons within the nucleus.

During β^--decay of a neutron, a down-quark is transformed into an up-quark via charged current of the weak interaction. The W^--boson that is exchanged in the interaction decays into an electron and an anti electron-neutrino. During β^+-decay of a proton inside a nucleus, an up-quark is transformed into an down-quark via charged current of the weak interaction. The W^+-boson that is exchanged in the interaction decays into a positron and an electron-neutrino. Figure 2.4 shows the corresponding Feynman diagrams. A β-decay can either

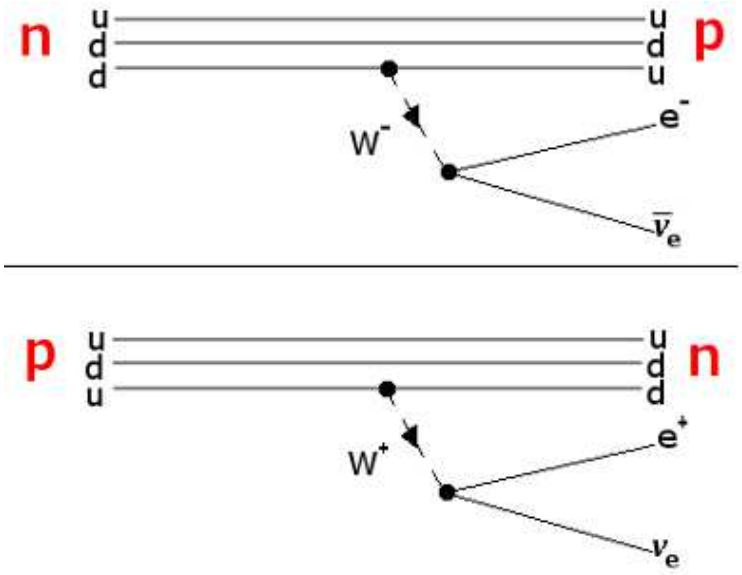

Figure 2.4: Feynman diagrams of β^- (top) and β^+-decay (bottom). The interactions take place by the exchange of a charged W-boson.

take place via vector coupling or via axial vector coupling, without interference between those two contributions. In the case of vector coupling, the transition is considered to be a Fermi-transition. Here, the spin direction of the participating fermions is conserved. The corresponding transition matrix element reads

$$|M_{fi}|_{\mathrm{F}} = \frac{\mathrm{G_F}}{\mathrm{V}}\,\mathrm{c_v}\,|\langle \mathrm{uud}|\sum_{i=1}^{3} T_{i,+}|\mathrm{udd}\rangle|\,, \tag{2.30}$$

where $\mathrm{G_F}$ is the Fermi-constant as given in Eq. 2.3, $\langle \mathrm{uud}|$ and $|\mathrm{udd}\rangle$ are the quark states before and after the transition and $\sum_{i=1}^{3} T_{i,+}$ is the operator that transforms particles with a weak isospin state T=+1/2 into the state T=-1/2, summarized over all three participating quarks. As the quark states are eigenstates of the strong interaction, the weak isospin operator $\mathrm{T_+}$ has to be transformed to the strong isospin operator $\mathrm{I_+}$. This can be done according to [PRSZ06]

$$\langle \mathrm{uud}|T_+|\mathrm{udd}\rangle = \langle \mathrm{uud}|I_+|\mathrm{udd}\rangle \cdot \cos\theta_{\mathrm{C}}, \tag{2.31}$$

where θ_C is the Cabbibo-angle, which describes a mixing of the quark eigenstates with respect to the weak isospin operator as described in section 2.1.1. With this transformation, the matrix element in Eq. 2.30 reads

$$|M_{fi}|_F = \frac{G_F}{V} \cos\theta_C c_v, \tag{2.32}$$

and is independent of the inner structure of the nucleon. In contrast, axial-vector coupling, which defines Gamow-Teller-Transitions, causes a spin-flip of the fermions. Accordingly, the transition matrix element depends on the superposition of the spin densities of the weakly interacting fermions. The transition operator for that case is $c_A T_+ \vec{\sigma}$, with the spin-operator $\vec{\sigma}$. In contrast to Fermi transitions, this transition operator depends on the inner structure of the nucleus. The transition matrix element for Gamow-Teller transitions

$$|M_{fi}|_{GT} = \frac{G_F}{V} c_A \, |\langle uud| \sum_{i=1}^{3} T_{i,+} \vec{\sigma} |udd\rangle|, \tag{2.33}$$

can be calculated by use of the valence-quark model and leads to

$$|M_{fi}|_{GT} = \frac{G_F}{V} c_A \cdot \frac{5}{3} \cdot \cos\theta_C. \tag{2.34}$$

Therefore, the total squared transition matrix element turns out to be

$$|M_{fi}|^2 = \frac{(g_V^2 + 3g_A^2)}{V^2} \tag{2.35}$$

with the two factors

$$g_V = G_F \cos\theta_C c_V , \tag{2.36}$$

$$g_A \approx G_F \cos\theta_C \frac{5}{3} c_A . \tag{2.37}$$

The factor 3 in the axial vector contribution in Eq. 2.35 results from the expectation value of the spin operator. According to Eq. 2.29, the matrix element can be used to calculate the decay rate. In momentum space, Eq. 2.29 can be written in the form

$$N(p)\,dp = \frac{2\pi}{\hbar} |M_{fi}|^2 \cdot \frac{dn}{dE_0}. \tag{2.38}$$

Again, dn/dE_0 is the density of final states per energy range. From Eq. 2.21, dn is already known. As the total number of states comprises protons and neutrons independently, the expression 2.21 has to be divided by two to account for each particle type. As this is a general expression for the number of available states within a certain volume of phase space, it can also be used to describe the number of available states for electrons and neutrinos in β-decay. The momenta of electron and neutrino are not correlated and the probability for a transition of the electron in the momentum interval dp_e and a simultaneous transition of the neutrino into

the momentum interval dp_ν is a product of both probabilities. This yields the following momentum and energy spectra of the β-particles [MK84]

$$N(\epsilon)d\epsilon = \frac{(g_V^2 M_F^2 + 3g_A^2 M_{GT}^2)}{B} F(Z,\eta)\,\eta^2\,(\sqrt{1+\eta_0} - \sqrt{1+\eta})^2\,d\eta\,, \quad (2.39)$$

$$N(\epsilon)d\epsilon = \frac{(g_V^2 M_F^2 + 3g_A^2 M_{GT}^2)}{B} F(Z,\eta)\,\epsilon\,\sqrt{\epsilon^2-1}\,(\epsilon_0 - \epsilon)^2\,d\epsilon\,. \quad (2.40)$$

All the constants have been combined to one constant factor B

$$B = \frac{2\pi^3\hbar^7}{m_0^5 c^4}, \quad (2.41)$$

ϵ_0 is the total energy of the decay (also known as Q-value), F(Z,η) is the Fermi-function which accounts for the Coulomb-correction in the spectral shape and η and ϵ are the momentum and energy of the electron, respectively. Figure 2.5 shows the shape of the momentum spectrum without Coulomb correction and with coulomb correction. These spectral forms are derived under the approximation of vanishing

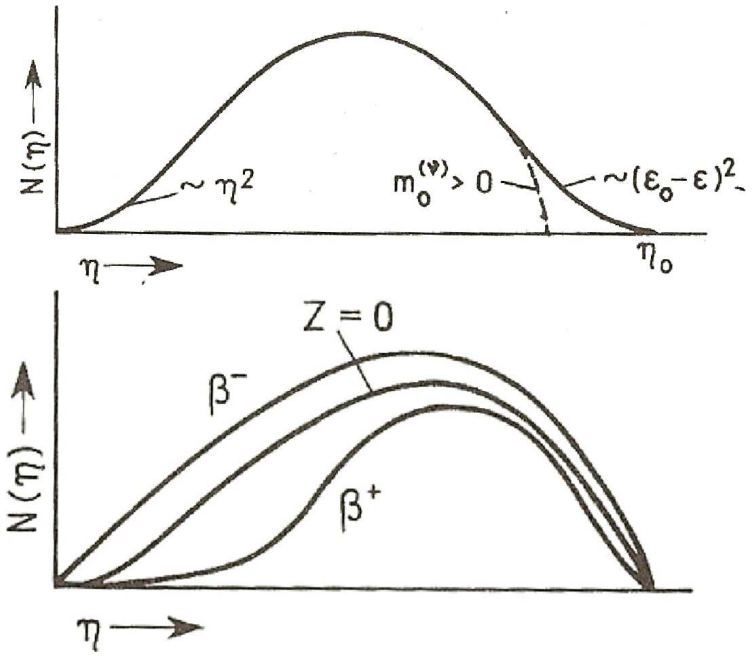

Figure 2.5: Continuous allowed β-spectrum. Top: β-spectrum neglecting the correction for the Coulomb-field of the nucleus for vanishing neutrino mass (solid line) and non-vanishing neutrino mass (dashed line). Bottom: Coulomb-corrected β-spectrum for positron emission (β^+) and electron emission (β^-) compared to the β spectrum without Coulomb correction (Z=0) [MK84].

neutrino masses, constant leptonic wave functions throughout the volume of the nucleus and non-relativistic approximation of the nucleons. These spectra are a

good description of allowed β-decays, which are first order processes. In allowed β-decays, the change in nuclear spin is either zero or one.
The probability λ for the decay to occur is determined by an integration of the energy spectrum over all possible energies

$$\frac{\log 2}{T_{1/2}} := \lambda = \int_1^{\epsilon_0} N(\epsilon)\, d\epsilon = \frac{(g_V^2 M_F^2 + 3g_A^2 M_{GT}^2)}{B} f(Z, \epsilon_0), \tag{2.42}$$

where f(Z,ϵ_0) is a Z and ϵ_0-dependent function that contains the Fermi-function F(Z,η) and can usually only be solved numerically

$$f(Z\epsilon_0) = \int_1^{\epsilon_0} F(Z, \epsilon)\epsilon\sqrt{\epsilon^2 - 1}(\epsilon_0 - \epsilon)^2 d\epsilon. \tag{2.43}$$

The f-value is often used as a quantity to describe nuclear matrix elements and the coupling constants g_A and g_V. Including the half-life $T_{1/2}$, the ft-value is defined as

$$ft := f(Z, \epsilon_0) \cdot T_{1/2} = \frac{B \cdot \log 2}{g_V^2 M_F^2 + 3g_A^2 M_{GT}^2}. \tag{2.44}$$

The ft-value is determined by measuring the half-life $T_{1/2}$ and the Q-value of a decay, which is equal to the maximum energy ϵ_0. It is used to classify the transition probability of a decay (see Table 2.5). The ft-value in logarithmic form is called log ft-value. The log ft values vary between 2.95 for ^{6}He and 24.3 for ^{50}V [BJSJ98]. The log ft value is small for allowed decays. Allowed decays are characterized by the fact that either the Gamow-Teller part or the Fermi part of the transition matrix element is finite in the approximation of constant lepton wave-functions throughout the volume of the nucleus and non-relativistic nucleons. Accordingly, allowed β-decays obey certain selection rules that can be different for Fermi- and Gamow-Teller transitions. These selection rules for allowed decays are summarized in Table 2.5.
In some decays, the selection rules cannot be fulfilled as the initial and final states can require the emission of leptons with an angular momentum $l > 0$. In a first approximation, which neglects all higher order terms in a Taylor series of the wave function of the neutrino, $l > 0$ would lead to a vanishing of the lepton wave-functions. Thus, the transition is only possible in higher orders. Higher-order transitions are also possible when the approximation of non-relativistic nucleons, where v was assumed to fulfill $v \ll c$, does not hold. In summary, transitions in higher orders of matrix elements are called x-fold forbidden β-decays, x being the forbiddenness depending on the order of the transition. Table 2.5 shows the selection rules for the forbidden decays, up to fourth-forbidden transitions. β-decays are named "unique" if no change in parity occurs for an odd-numbered change in nuclear spin or if a change in parity occurs for an even-numbered change in nuclear spin. "Non-unique" describes β-decays that change parity for odd-numbered change in nuclear spin and that conserve parity for even-numbered change in nuclear spin.

Table 2.5: Selection rules for different order processes of β-decays up to fourth-forbidden decays [MK84, BJSJ98]. ΔP of "+" means no change in parity, ΔP of "-" means a change in parity

Transition	Δs (spin)	ΔP (parity)	log ft
Allowed	0, $\pm$1	+	< 10.1
First forbidden	0, $\pm$1	-	5.1-13.3
First forbidden "unique"	2	-	7.5-12.7
Second forbidden	2	+	10.5-14.1
Second forbidden "unique"	3	+	13.86-18.0
Third forbidden	3	-	17.5
Third forbidden "unique"	4	-	20.7-21.4
Fourth forbidden	4	+	22.5-24.3

2.2.3.1 Theoretical Description of the Decay of ^{113}Cd

The four-fold forbidden, non-unique β-decay of ^{113}Cd from ground state to ground state of ^{113}In is considered to be an ultra-rare decay. Four-fold forbidden, non-unique decays typically have log ft values larger than 20 and therefore half-lifes in the range of 10^{15} years (see Table 2.5). Only three isotopes are known to exclusively decay via this decay channel: These isotopes are ^{50}V, ^{115}In and ^{113}Cd, which will be dealt with in this section.
The theoretical spectral shape, the half-life and the log ft value have been theoretically determined by [MAS06] and [MS07], which will be presented in this section and compared to measured data in section 4.3. [MAS06] used the microscopic quasiparticle-model (MQPM) to determine the initial and final states of the transition $^{113}\mathrm{Cd} \xrightarrow{\beta} {}^{113}\mathrm{In}$. The microscopic quasiparticle-model was developed to describe spherical or nearly spherical states of open-shell, odd-A nuclei. In the shell model as described in section 2.2.2, the nucleons are described to occupy well-defined energy-states that result in discrete energy levels. Open-shell nuclei denotes nuclei with an outer shell that is not completely or nearly completely filled with nucleons. The microscopic quasiparticle-model is a self-consistent, fully microscopic description.
The description of the initial and final states are not affected by the forbiddenness of a decay and the transition density as determined by the microscopic quasiparticle-model can be implemented in the general β-decay framework.
The log ft-values and the energy spectra were computed by [MAS06]. The ordering of the low-energy states of ^{113}Cd could not exactly be reproduced, which is due to the failure of the BCS[10] calculations to reproduce the low-energy spectrum of ^{113}Cd. This could also lead to a smaller calculated decay rate compared to the

[10] BCS is a many body theory that was initially developed to describe the behavior of superconducting metals.

experiment. Accordingly, the log ft value of ^{113}Cd was determined to be 23.45, yielding a half-life of $1.69{\cdot}10^{16}$ years [MAS07], which is above the experimentally determined value being $(7.7\text{ - }8.2 \pm 0.2(\text{stat})^{+0.2}_{-1.0}(\text{sys})) \cdot 10^{15}$ years. [KAE, GJK$^+$05] As the log ft values and the spectral shape of the decay did not exactly reproduce the experimental data, a proton-neutron variant of the MQPM (pnMQPM) was introduced in 2007 [MS07]. The states of the pnMQPM are created by coupling quasiparticles with phonons by the proton-neutron quasiparticle random-phase approximation (pnQRPA). This leads to a log ft-value of 23.25, indicating a half-life of $10.5{\cdot}10^{15}$ years, which is in reasonable agreement with the experimental values. Moreover, the spectral shape could be determined using the pnMQPM-model. It is shown in Figure 2.6.

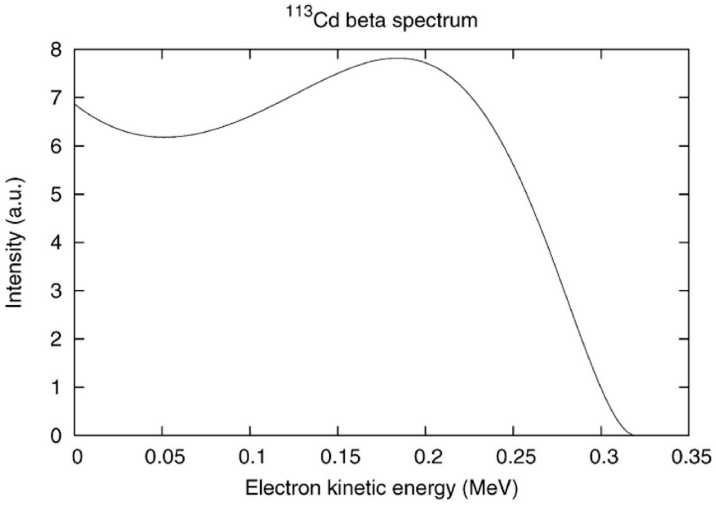

Figure 2.6: Theoretical spectrum of the four-fold forbidden decay ^{113}Cd$\rightarrow^{113}$In calculated with the pnMQPM model [MS07].

2.2.4 Double-Beta Decay

In the previous section it was shown that even-A nuclei can have several β-stable even-even isobars. The only possibility for these isobars to decay into a state with a more favorable energy is via double-beta decay, where an even-even nucleus decays into an energetically lower even-even nucleus with the same atomic mass number under the emission of two charged leptons and two neutrinos. The energy spectrum of the charged leptons is continuous (see Fig. 2.9), because the final state contains additional neutrinos. As even-even nuclei have a ground state spin of zero and positive parity, double-beta decay is a $(0^+ \rightarrow 0^+)$ transition of the second order. Ensuring that β-decay to an odd-odd isobar does not take place and that the final state has a smaller mass than the initial state, it can only occur if the following

requirements are fulfilled

$$\mathrm{m(A,Z+1) > m(A,Z) > m(A,Z+2)\,.} \tag{2.45}$$

Accordingly, two subsequent β-decays are energetically forbidden [Sch97]. However, double-β-decay occurs by quantum-mechanically tunneling through the energy barrier at (A,Z+1). The existence of $2\nu\beta\beta$-decays has been verified in 1949 [IR49] and confirmed in 1967 [KSNS68] by geochemical methods that determine the anomal isotopic abundance in minerals. The results were confirmed in 1987 [EHM87] by various counting experiments.
The possible existence of a neutrinoless double-beta decay ($0\nu\beta\beta$) as proposed in 1939 [Fur39], which will be described in section 2.2.4.2, could answer the question whether the neutrino is a Dirac- or a Majorana particle.

2.2.4.1 Neutrino-Accompanied Double-Beta Decay

The neutrino-accompanied double-beta decay was first theoretically introduced in 1935 [GM35] in the form:

$$\mathrm{(Z,A)} \rightarrow \mathrm{(Z+2,A) + 2e^- + 2\overline{\nu}_e}\,, \tag{2.46}$$

$$\mathrm{2n} \rightarrow \mathrm{2p + 2e^- + 2\overline{\nu}_e} \quad \text{in hadronic illustration}\,, \tag{2.47}$$

$$\mathrm{2d} \rightarrow \mathrm{2u + 2e^- + 2\overline{\nu}_e} \quad \mathrm{in\ the\ quark-framework}\,. \tag{2.48}$$

It can be understood as two simultaneous neutron decays via a virtual intermediate state. The corresponding Feynman diagram is shown in Fig. 2.7. According to Eq. 2.46, lepton number is conserved in this second-order process. The final state contains five particles out of which four leptons carry away the energy that is equal to the Q-value of the decay while the nucleus is at rest. The transition-matrix element is a product of the transition matrix element from the transition of the initial into the intermediate state and the transition matrix element from the transition of the intermediate state into the final state, divided by the energy of the intermediate state. As several intermediate states are possible, the transition matrix element reads [PRSZ06]

$$\mathrm{M^{2\nu} = \sum_m \frac{\langle f, 2e^+, 2\nu_e|H_W|m, e^+, \nu_e\rangle \langle m, e^+, \nu_e|H_W|i\rangle}{E_m - \frac{M_i+M_f}{2}c^2}}. \tag{2.49}$$

$\mathrm{H_W}$ is the weak Hamiltonian, $\mathrm{E_m}$ is the energy of the intermediate state, $\langle \mathrm{f}|$ is the final state and $|\mathrm{i}\rangle$ is the initial state. The phase space $\mathrm{G^{2\nu}}$ for the neutrino-accompanied double-beta decay contains four additional particles in the final state and therefore reads

$$\mathrm{G^{2\nu} = \frac{(4\pi)^4}{(2\pi)^{12}(\hbar c)^{12}} \cdot \frac{E_0^{11}}{2000}}\,. \tag{2.50}$$

The factor $\frac{\mathrm{E_0^{11}}}{2000}$ results from an approximation of the f-value (see Eq. 2.43) for large energy ($\mathrm{E_0 \gg m_e c^2}$) [PRSZ06] and the phase space for four particles. For a

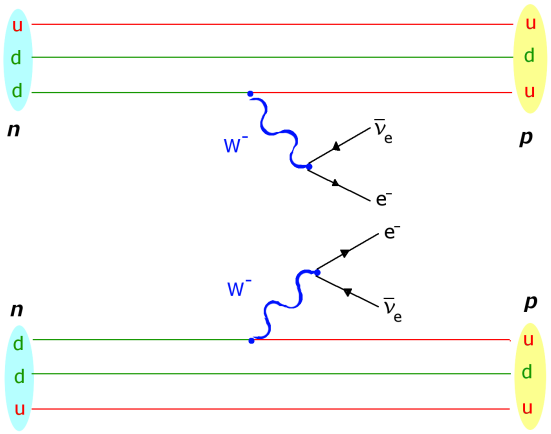

Figure 2.7: Feynman diagram of neutrino-accompanied double-beta decay. Two neutrons decay simultaneously into two protons within the nucleus. The quarks of the neutron and proton are illustrated by the straight lines. In the transition, two down-quarks are simultaneously transformed into two up-quarks.

lower limit of the half-life, it is assumed that the sum transition matrix element in Eq. 2.49 is maximized and therefore equal to one. Accordingly, the total transition matrix element reduces to G_F^2/E_0, yielding a half-life of [PRSZ06, Zub04]:

$$\begin{aligned}(T_{1/2}^{2\nu})^{-1} &= G^{2\nu}(Q,Z) \mid M_{GT}^{2\nu} + \frac{g_V^2}{3g_A^2} \cdot M_F^{2\nu} \mid^2 \\ &\approx \frac{2\pi}{\hbar} \cdot \frac{G_F^4}{E_0^2} \cdot \frac{(4\pi)^4}{(2\pi)^{12}(\hbar c)^{12}} \cdot \frac{E_0^{11}}{2000} \,. \end{aligned} \tag{2.51}$$

$M_{GT}^{2\nu}$ and $M_F^{2\nu}$ are the matrix elements for Gamow-Teller and Fermi transitions, respectively. As the intermediate states are 1^+ states (spin=1, positive parity), Fermi-transitions are strongly suppressed and thus neglected in Eq. 2.51.
The experimentally determined half-lifes of neutrino-accompanied double-beta decay are of the order of 10^{19}-10^{24} years.
While 36 isotopes are known that can undergo neutrino-accompanied double-beta decay, there are also six isotopes that can undergo double-positron decay. In that case, a proton decays within a nucleus into a neutron, a positron and an electron neutrino

$$(Z,A) \rightarrow (Z-2,A) + 2e^+(+2\nu_e) \,. \tag{2.52}$$

In case a neutrinoless double-beta decay exists, double-positron decay is also possible without the emission of neutrinos. The double-positron decay is always accom-

panied by electron capture involving processes, as they are energetically favored:

$$e_B^- + (Z, A) \rightarrow (Z-2, A) + e^+ (+2\nu_e)\,, \tag{2.53}$$

$$2e_B^- + (Z, A) \rightarrow (Z-2, A)\ (+2\nu_e)\,, \tag{2.54}$$

where one or two electrons are captured from the K-shell. $\beta^+\beta^+$-decays have an enhanced sensitivity to right-handed weak currents [Zub04]. Accordingly, they will become more important when neutrinoless double-beta decay is confirmed because they will play a key role in investigating the underlying physics. However, as this thesis deals with neutrinoless double-beta decay, $\beta^+\beta^+$-decays will not be further discussed.

2.2.4.2 Neutrinoless Double-Beta ($0\nu\beta\beta$) Decay

Neutrinoless double-beta decay, as proposed by [Fur39] in 1939, is a lepton-number violating process that requires non-vanishing neutrino masses. It is therefore forbidden in the Standard Model. It can be seen as two subsequent processes (Racah sequence) [Zub04]

$$(Z, A) \rightarrow (Z+1, A) + e^- + \overline{\nu}_e, \tag{2.55}$$

$$(Z+1, A) + \nu_e \rightarrow (Z+2, A) + e^-. \tag{2.56}$$

A neutron decays into a virtual intermediate state under the emission of an electron and a right-handed anti-electron neutrino. This anti electron-neutrino is absorbed as a left-handed electron-neutrino in a second step. This can only occur if neutrinos and anti-neutrinos are identical particles. A Feynman diagram of the neutrinoless double-beta decay is shown in Fig. 2.8. Two-component particles that are identical with their anti-particles are called Majorana particles. As left-handed anti-neutrinos can only contain a right-handed component if they have a non-vanishing rest-mass (see sect. 2.1.4.1) neutrinoless double-beta decay would be an additional proof for non-vanishing neutrino masses. Among other possibilities, (V+A) weak charged currents could also cause neutrinoless double-beta decay, but as the Schechter-Valle [SV82] theorem states that a $0\nu\beta\beta$-decay always implies a non-vanishing Majorana neutrino rest mass, the Majorana neutrino mass mechanism always contributes to neutrinoless double-beta decay. Therefore, a $0\nu\beta\beta$-decay would prove the Majorana-character of the neutrino.
As only two fermions are created in $0\nu\beta\beta$-decay, the phase space is larger than for $2\nu\beta\beta$-decay [PRSZ06]

$$G^{0\nu} = \frac{(4\pi)^2}{(2\pi)^6(\hbar c)^6} \cdot \frac{E_0^5}{32}. \tag{2.57}$$

Accordingly, $0\nu\beta\beta$-decay is favored by the phase space compared to $2\nu\beta\beta$-decay. Nevertheless, a left-handed neutrino with mass m_ν only has a right-handed component of (1-β_ν) with $\beta_\nu = v/c$, which is extremely small for small neutrino masses.

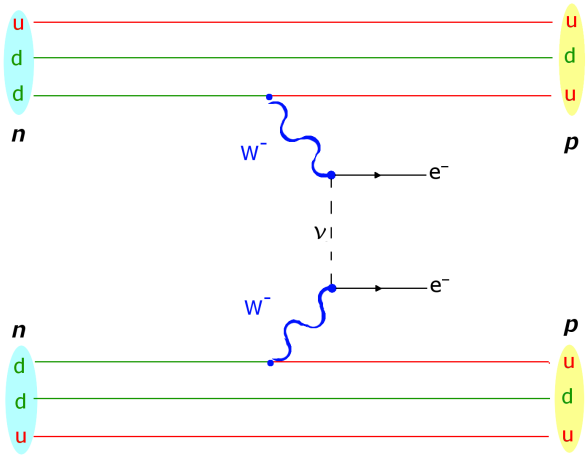

Figure 2.8: Feynman diagram of neutrinoless double-beta decay. A neutron decays into a proton under the emission of an electron and an anti-electron neutrino that is absorbed as an electron-neutrino by another neutron under the emission of another electron. The quarks are illustrated as straight lines. Two down-quarks are transformed into two up-quarks.

Accordingly, the half-life of the neutrinoless double-beta decay in the case of mass-mechanism reads [Sch97]

$$(\mathrm{T}^{0\nu}_{1/2})^{-1} = \mathrm{G}^{0\nu}|\mathrm{M}^{0\nu}_{\mathrm{GT}} - \frac{\mathrm{g}_{\mathrm{V}}^2}{3\mathrm{g}_{\mathrm{A}}^2} \cdot \mathrm{M}^{0\nu}_{\mathrm{F}}|^2 \left(\frac{\langle m_{\nu_e}\rangle}{m_e}\right)^2, \tag{2.58}$$

which yields [PRSZ06]

$$(\mathrm{T}^{0\nu}_{1/2})^{-1} \approx \frac{2\pi}{\hbar} \cdot \frac{\mathrm{G}_{\mathrm{F}}^4}{\mathrm{R}^4} \cdot \frac{(4\pi)^2}{(2\pi)^6(\hbar c)^6} \cdot \frac{\mathrm{E}_0^5}{32} \cdot (1-\beta_\nu). \tag{2.59}$$

$M^{0\nu}_{GT}$ and $M^{0\nu}_{F}$ are the Gamow-Teller and Fermi transition matrix elements for neutrinoless double-beta decay. While the phase space factor can exactly be calculated, the determination of the matrix elements involves many insecurities. The matrix elements are calculated based on different models either using the nuclear shell model or the Quasiparticle Random Phase Approximation [Sch97]. Accordingly, an error of a factor 3 in the half-life calculations must be expected from these calculations. The effective Majorana mass $\langle m_{\nu_e}\rangle$ can be determined using the elements of the lepton mixing matrix $\mathrm{U_{ei}}$ (see section 2.1.4.1) with their accordant mass-eigenvalues $\mathrm{m_i}$ and the CP-phases, also known as Majorana-phases, $\alpha_i/2$, which are $\alpha_i/2 = \mathrm{k}\pi$ if CP is conserved [Zub04]

$$\langle \mathrm{m}_{\nu_\mathrm{e}}\rangle = \left|\sum_i \mathrm{U}^2_{\mathrm{ei}}\mathrm{m_i}\right| = \left|\sum_i |\mathrm{U_{ei}}|^2 \mathrm{e}^{2\mathrm{i}\alpha_\mathrm{i}}\mathrm{m_i}\right|. \tag{2.60}$$

The half-lives of neutrinoless double-beta decay are expected to be in the range of 10^{26} years or even larger. In 2001, a subgroup of the Heidelberg-Moscow experiment, which will be described in detail in section 2.3, claimed to have found evidence for $0\nu\beta\beta$-decay [KKDHK01], which they confirmed in 2004 [KKKDC04] and 2006 [KKK06] with $6\,\sigma$ confidence level, yielding a half-life of $0\nu\beta\beta$-decay of $2.23^{+0.44}_{-0.31} \cdot 10^{25}$ years [KKK06]. As the entire energy of the neutrinoless double-beta decay is carried away by the charged electrons, the combined spectrum of both charged particles is a single peak at the Q-value (the energy difference between the initial and the final state) of the decay. This provides the possibility for experimental detection despite its very large half-life. Figure 2.9 shows the spectral shape of neutrinoless double-beta decay compared to that of neutrino-accompanied double-beta decay.

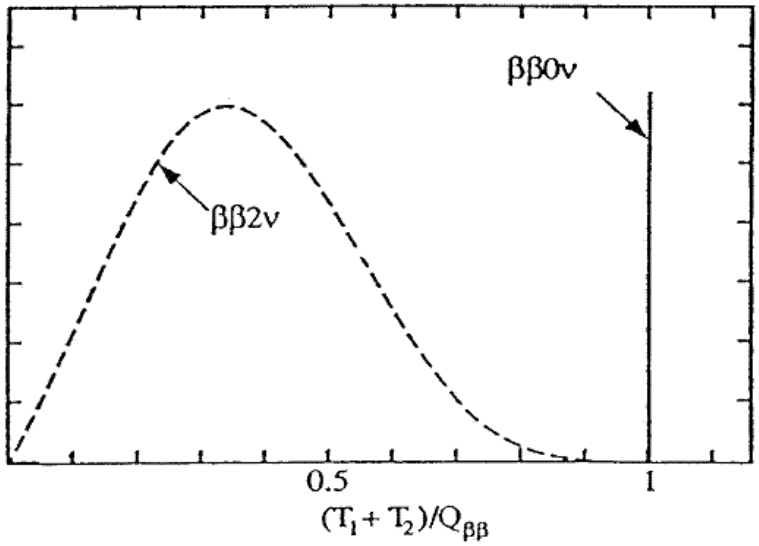

Figure 2.9: Schematic combined spectra of the total energy of the electrons in $2\nu\beta\beta$-decay (dashed line) and $0\nu\beta\beta$-decay (solid line) [NEM]. The $2\nu\beta\beta$-decay shows a continuous spectrum below the Q-value of the decay, while the $0\nu\beta\beta$-decay shows a single peak at the Q-value of the decay.

Other processes that can be involved in neutrinoless double-beta decay are the following: The Δ-mechanism, where the same particle undergoes two successive β-decays and the Δ-baryon occurs as intermediate state in π-exchange, can cause $0\nu\beta\beta$-decay. Moreover, the π-mechanism, where a pion undergoes a $\beta\beta$-decay, could contribute to $0\nu\beta\beta$-decay. An additional contribution could arise from the creation of a hypothetical majoron χ, which would exist in the case of a spontaneous violation of (B-L)-symmetry[11], super heavy neutrino exchange,

[11] B is the baryon number, L the lepton number.

supersymmetry particles [Sch97].

2.3 Experimental Evidence of $0\nu\beta\beta$-Decay

The Heidelberg-Moscow Experiment

The Heidelberg-Moscow experiment was proposed in 1987 [KK87] in order to measure neutrinoless double-beta decay with ^{76}Ge semiconductor detectors. The experiment started operation in August 1990 and finished on November 30, 2003.
The complete setup consisted of five high-purity germanium-detectors enriched to at least 86 % in ^{76}Ge. This provided a high-energy resolution of 0.2 % in the region of interest[12]. The setup was finished in Feburary 1995. The experiment was located at the Gran Sasso underground Laboratory, Italy. A shielding of 3500 mwe[13] is provided by the overburden. The total detector mass was 10.96 kg. Four of the five detectors were shielded by a commercial shielding consisting of lead, located inside an air-tight steel-box constantly flushed with nitrogen, surrounded by boron-loaded polyethylene plates [G$^+$97]. The fifth detector was shielded by copper surrounding, lead and boron-loaded polyethylene plates. Weekly calibrations were performed with ^{228}Th, ^{60}Co and ^{152}Eu calibration sources [G$^+$97].
A first evidence for $0\nu\beta\beta$-decay was claimed by the Heidelberg-Moscow experiment in 2001, where a confidence level of 2.2-3 σ (depending on the model used for the calculations) was achieved [KKDHK01]. This result could be improved in 2004 [KKKDC04], where the confidence level could be determined to be 4.2 σ. Altogether, 71.7 kg years of data were investigated, including the entire amount of data collected from 1990 until 2003. The spectrum in the energy region of interest (2000-2060 keV) is shown in Fig. 2.10. Six peaks are visible. Four of them could be identified as γ-lines from the isotope ^{214}Bi that occur at 2010.7, 2016.7, 2021.8 and 2052.9 keV. One peak occurred at 2300 keV that could not be identified. The peak that is visible at 2038.44±0.45 keV was assigned to the neutrinoless double-beta decay (occurring at Q=2039.006 [DFC$^+$01]) of ^{76}Ge, proving its existence with 4.2 σ-confidence.
In 2006, the entire dataset was again investigated, using two different types of pulse shape analysis for background reduction. One approach was the use of a neuronal net for selecting $0\nu\beta\beta$-events from the background [KKK06]. The other approach was comparing measured pulses with simulations of the electric field distribution in the detectors. A confidence level of 6 σ was achieved with these methods [KKK06]. From these results, the $0\nu\beta\beta$-decay half-life of ^{76}Ge was determined to be [HME]

$$T_{1/2} = (2.23^{+0.44}_{-0.31}) \cdot 10^{25} \text{ years}. \tag{2.61}$$

[12] The region of interest is the Q-value of the $0\nu\beta\beta$-decay of ^{76}Ge: Q=2039.01±0.32 keV [G$^+$97].
[13] **m**eters of **w**ater **e**quivalent

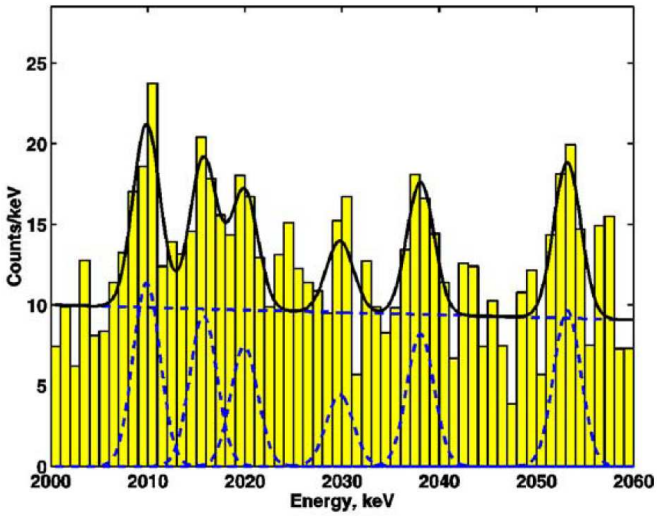

Figure 2.10: Spectrum obtained by the Heidelberg-Moscow experiment, containing 71.7 kg years of data. The constant background and the single peaks have been fitted (dashed line) and added up (solid line) and are shown together with the measured spectrum (yellow). Six peaks are visible, one of them in the energy region of interest, at 2038.44 keV [KKKDC04].

Moreover, a Majorana neutrino mass (see Eq. 2.60) could be determined under the assumption that only the mass mechanism contributes to the observed peak (see section 2.2.4.2 for a brief discussion) and that the uncertainty in the nuclear matrix element calculations was 50 % [HME]

$$m_{\nu_e} = (0.32 \pm 0.03)\,\text{eV} \quad (99.97\,\%\,\text{CL}). \tag{2.62}$$

Nevertheless, the results of this experiment have not been accepted by the science community due to open questions. Accordingly, more precise experiments are required.

Chapter 3

The COBRA Experiment

This chapter describes the current status and setup of the COBRA[1] experiment. After illustrating the problems arising from different background components from the natural decay chains in section 3.2 and explaining the aim of the COBRA experiment in sections 3.1 and 3.3, the current status of the two approaches for the COBRA experiment, coplanar grid detectors and pixelated detectors, are introduced in section 3.4. In order to make an appropriate choice between these two detector designs, both of them are still under investigation. The current setup and shielding of both approaches are described and the necessities and problems for a future large-scale experiment are explained for both cases. The chapter closes with section 3.7, presenting the latest achievements of the experiment and giving an outlook.

3.1 Motivation

During the past 10 years, neutrino physics have undergone a great progress. Various experiments have shown that neutrinos possess a non-vanishing rest mass by proving that neutrinos oscillate between different flavor-eigenstates. Unfortunately, these experiments are not able to determine the absolute value of the neutrino masses but only the difference between the squared masses. Also they cannot identify the nature of the neutrinos, being either Dirac or Majorana particles. One approach to solve both yet unanswered questions is the investigation of neutrinoless double-beta decays ($0\nu\beta\beta$-decays), providing both informations about the nature of neutrinos [Fur39] and the value of their rest mass [Ros]. Several experiments have been performed in order to answer these questions, among them the Heidelberg-Moscow experiment [HME]. In 2001, evidence for the $0\nu\beta\beta$-decay measured in ^{76}Ge was published [KKDHK01] and confirmed in 2004 [KKKDC04]. If these results hold true, this would yield a $0\nu\beta\beta$ half-life of ^{76}Ge of 0.7-4.2$\cdot 10^{25}$ years, which is equivalent to an effective Majorana neutrino mass of 0.2-0.6 eV.

[1] Location of the experiment at the **L**aboratori **N**azionali del **G**ran **S**asso (LNGS), Italy

These publications have raised a vivid discussion, so that further experiments with germanium have been set up to prove or refute the claimed results, for example MAJORANA[2] and GERDA[3] [Col05]. In order to exclude the possibility that the observed signal stems from a germanium-specific background that has not been identified yet, it is desirable to confirm the results with a different element than germanium: Promising candidates are the elements Cd and Te, as used in the COBRA experiment. COBRA searches for neutrinoless double-beta decay with CdZnTe (cadmium-zinc-telluride) semiconductors. Compared to other detectors, semiconductor detectors offer the advantage that they consist of very clean and radiopure materials and can achieve good energy resolutions. In order to obtain the maximum possible detection efficiency for the decays of interest, source and detector are identical.
The detector material contains 9 double-beta emitters, 5 being $\beta^-\beta^-$-emitters and 4 being $\beta^+\beta^+$-emitters [Zub01]. They are listed in tables 3.1 and 3.2. Of special interest are ^{116}Cd with a Q-value of 2.805 MeV, which is at a larger energy then the naturally occurring γ-lines, and ^{130}Te with a Q-value of 2.529 MeV.

Table 3.1: $\beta^-\beta^-$-emitters that are contained within the detectors used for the COBRA experiment with the corresponding Q-values and natural abundance. Of special interest are the decays of ^{116}Cd because of the particularly high Q-value and the decay of ^{130}Te because of the large natural abundance [Zub01].

Isotope	Q-value (keV)	natural abundance (%)
^{70}Zn	1001	0.62
^{114}Cd	534	28.7
^{116}Cd	2805	7.5
^{128}Te	868	31.7
^{130}Te	2529	33.8

Table 3.2: $\beta^+\beta^+$-emitters that are contained within the detectors used for the COBRA experiment with the corresponding Q-values, natural abundance and energetically possible decay modes. The decay of ^{106}Cd is especially interesting because of its high Q-value [Zub01].

Isotope	Q-Value (keV)	natural abundance (%)	Decay modes
^{64}Zn	1096.3	48.6	EC/EC, β^+/EC
^{106}Cd	2771	1.25	EC/EC, β^+/EC, β^+/β^+
^{108}Cd	231	0.9	EC/EC
^{120}Te	1722	0.10	EC/EC, β^+/EC

[2]The MAJORANA Neutrinoless Double-Beta Decay Experiment [MAJ]
[3]The **GER**manium **D**etector **A**rray [GER]

Besides neutrinoless double-beta decay, the COBRA experiment also provides access to other interesting physics. For the first time, there will be a realistic chance for observing double electron capture processes. Furthermore, rare processes such as the decay of ^{113}Cd or the electron capture of ^{123}Te are currently under investigation. The setup could also be used for dark matter detection [Zub01]. Of particular interest are β^+/EC decays because they have an enhanced sensitivity to right-handed weak currents [HMO$^+$94], which could help to investigate the underlying physics of $0\nu\beta\beta$-decays. In case of pixelated detectors, also the angular distribution of the particles can be determined. This will provide answers to the question which process contributes to what extent to $0\nu\beta\beta$-decays. Common to $0\nu\beta\beta$ decays of all isotopes is the particularly large half-life of approximately 10^{26} years, so investigation of this type of decay requires ultra-low background conditions. This thesis will introduce an effective background reduction method which gives an estimate on the intrinsic contamination of the detectors – a background source that can not be reduced by shielding. Furthermore, the four-fold forbidden, non-unique β-decay of ^{113}Cd will be investigated in order to provide a better understanding of the background spectrum.

3.2 Background

The neutrinoless double-beta decay is a rare process with an expected half-life of at least 10^{25}-10^{26} years [KKKDC04]. Therefore, it is essential to know and to eliminate as many background contributions as possible in order to detect the decay within a reasonable timespan. The sensitivity of an experiment scales with experimental parameters according to [Heu95]:

$$T_{\frac{1}{2}} \sim \alpha \cdot \epsilon \cdot \sqrt{\frac{M \cdot t}{\Delta E \cdot B}}, \tag{3.1}$$

where α is the natural abundance of the investigated isotope, ϵ is the detection efficiency, M is the source mass, t is the measurement time, ΔE is the energy resolution and B is the background index given in $\frac{\text{events}}{\text{a}\cdot\text{keV}\cdot\text{kg}}$. As shown in Fig. 3.1 a background of only 10^{-3} $\frac{\text{counts}}{\text{keV}\cdot\text{kg}\cdot\text{a}}$ is required in order to achieve sensitivities in the order of 10^{26} years using an array consisting of $40 \times 40 \times 40$ 1 cm^3 CdZnTe-detectors that have an enriched ^{116}Cd-content of 90 % within 4 years of measuring time at an energy resolution of 2%.

3.2.1 The Natural Decay Chains

One major background contribution arises from ^{40}K and from the natural decay chains, ^{238}U and ^{232}Th. The isotopes of the natural decay chains are contained in buildings, through minerals and rocks as well as the surrounding air. When

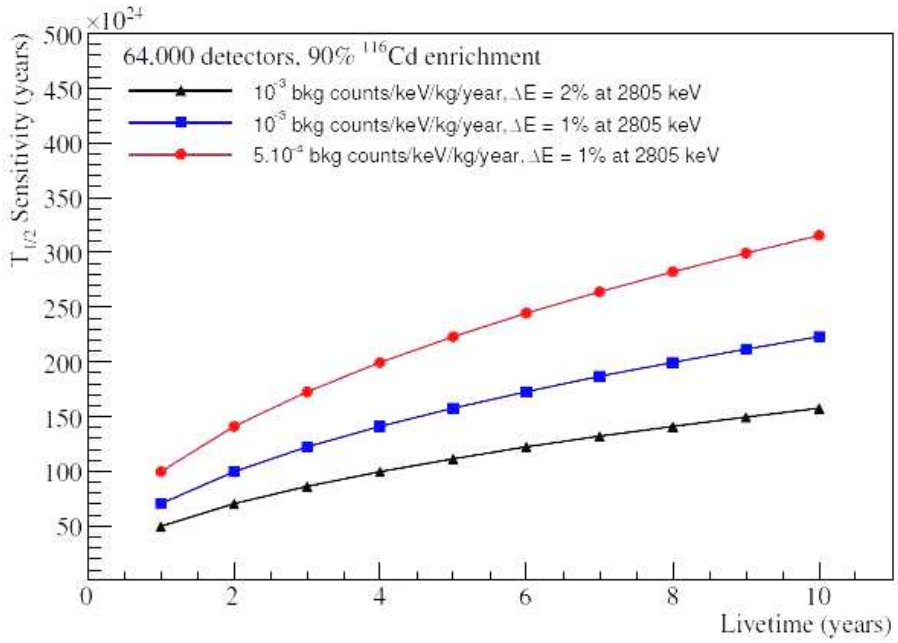

Figure 3.1: Expected half-life sensitivity for $40\times40\times40$ 1 cm^3 CdZnTe detectors at different energy resolutions and background levels. The desired neutrino mass sensitivity of 50 meV can be achieved with half-life measurements of about $2{\cdot}10^{26}$ years [B$^+$07b] and [Col06].

radium decays within a solid material, radon is generated and, being a noble gas, it is not chemically bound by the surrounding material but diffuses out into the surrounding air. The thorium chain contains ^{220}Rn, a radon isotope with a half-life of only 55.6 s. This half-life is almost too short for the radon to diffuse out of materials, but the ^{238}U chain produces the radon isotope ^{222}Rn with a half-life of 3.8 d. This is time enough to diffuse out of materials such that the surrounding air has an enhanced ^{222}Rn concentration.
The Rn background can be strongly suppressed by operating the detectors in a nitrogen environment. In order to reduce surface currents and to keep the crystals from degrading, they have previously been covered by a passivation paint, which produced a considerable radiation background. The idea of operating detectors without passivation paint in a nitrogen environment is currently under investigation. Further background reduction can be achieved by identifying timing coincidences within the decay chains. Within the ^{238}U chain, the most promising timing coincidence is the β-α coincidence of ^{214}Bi followed by ^{214}Po:

$$^{214}\mathrm{Bi} \xrightarrow{\beta} {}^{214}\mathrm{Po} \xrightarrow{\alpha} {}^{210}\mathrm{Pb}. \tag{3.2}$$

First, Bismuth emits a β-particle with a maximum energy of 3.272 MeV. This decay is the only β-decay within the natural decay chains that produces betas with an energy in the $0\nu\beta\beta$-region of ^{116}Cd and ^{130}Te. Because β-decay is a three-body decay, the β-spectrum is continuous. Afterwards, with a half-life of only 164.3 μs [NUC], ^{214}Po decays via α-decay into ^{210}Pb, emitting an α-particle with 7.687 MeV. Because of this extremely low half-life and the characteristic α energy, it is particularly easy to identify this decay sequence. 70% of the background contribution to the 2-3 MeV region of the ^{238}U chain arises from the decay of ^{214}Po. Coincidence analysis can identify 41.4% of the ^{214}Po decays and therefore contributes significantly to background reduction in the region of interest [Ree09].
The ^{232}Th chain also provides some decay sequences that are suitable for timing-coincidence analysis: ^{220}Rn decays via α-decay with an α energy of 6.288 MeV into ^{216}Po which has a half-life of only 0.145 s and subsequently decays via α-decay into ^{212}Pb with an α-energy of 6.778 MeV:

$$^{220}\mathrm{Rn} \xrightarrow{\alpha} {}^{216}\mathrm{Po} \xrightarrow{\alpha} {}^{212}\mathrm{Pb}. \tag{3.3}$$

Furthermore, the decay of ^{212}Bi is suited for timing-coincidence analysis:

$$^{212}\mathrm{Bi} \xrightarrow{\beta} {}^{212}\mathrm{Po} \xrightarrow{\alpha} {}^{208}\mathrm{Pb}, \tag{3.4}$$

$$^{212}\mathrm{Bi} \xrightarrow{\alpha} {}^{208}\mathrm{Tl} \xrightarrow{\beta} {}^{208}\mathrm{Pb}. \tag{3.5}$$

With a branching ratio of 64.06%, ^{212}Bi decays via β-decay into ^{212}Po. ^{212}Po has a half-life of $2.99{\cdot}10^{-7}$ s and emits an alpha particle with 8.785 MeV. Since the used ADCs[4] have a charge collection time of 120 μs, this coincidence is inapplicable for timing coincidence analysis. The remaining 35.94% of ^{212}Bi decay via α-decay into ^{208}Tl with α-energies of 6.051 MeV and 6.090 MeV. This isotope emits β-particles with 1.796 MeV at the most and has a half-life of 183.18 s, which makes timing-coincidence analysis difficult because this timespan is too large to be very selective. However, this analysis is still worthwhile because ^{208}Tl also emits gammas up to 2.614 MeV that contribute a major background to the $0\nu\beta\beta$-region of ^{130}Te. Knowing the amount of ^{208}Tl might provide an estimate of the γ-background.
Timing-coincidence analysis can especially be used to estimate internal detector contamination limits. Since α- and β-radiation occurring from particles that are incorporated in the detectors is expected to deposit their full energy within the detector volume, this analysis method becomes even more selective.

3.2.2 Investigated Isotopes

A first step to successful background reduction is the choice of an appropriate isotope because the Q-value of the decay defines the position of the peak within

[4] Analog-to-Digital Converter

the spectrum. Since the background rate depends on the energy, the choice of an appropriate Q-value can locate the $0\nu\beta\beta$-peak within an energy range where the background rate is low. The two main isotopes of interest are ^{130}Te, with a Q-value of 2.529 MeV and ^{116}Cd, with a Q-value of 2.809 MeV. There are two major aspects that make a high Q-value desirable: The decay rate scales with Q^5, so a high Q-value will provide a relatively high decay rate [SFM09]. ^{116}Cd is especially interesting, because the highest naturally occurring gamma radiation appears within the ^{232}Th chain and has an energy of 2.615 MeV [NUC]. Therefore the naturally occurring gamma radiation will not produce any background events in the $0\nu\beta\beta$-region of ^{116}Cd .

3.2.3 $2\nu\beta\beta$-Decay of ^{116}Cd

The $2\nu\beta\beta$-decay of ^{116}Cd produces a continuous background signal between 0 keV and the $0\nu\beta\beta$-energy of ^{116}Cd, where the $0\nu\beta\beta$-decay of ^{116}Cd, if existent, generates a sharp peak. It is problematic that the rate of the $2\nu\beta\beta$-decay is at least four orders of magnitude larger than that of the $0\nu\beta\beta$-decay. In order to distinguish between both processes, an outstanding energy resolution of the detectors is required.

3.2.4 Cosmogenic Produced Radio-Isotopes

Another possible background source arises from cosmogenic produced radio-isotopes inside the detector volume and the surrounding materials. Accordingly, it is essential to store the materials in a well-shielded environment. Furthermore, a good knowledge of the occurring radio-isotopes is essential. The only dangerous radiation arises from ^{56}Co, which is produced within the shielding materials lead and copper and emits γ–particles with energies up to 2.599 MeV. Other isotopes of potential danger are ^{126}Sb, ^{124}Sb, ^{110}Ag, ^{88}Y and ^{60}Co [Col05], but those do not have any intense γ-lines in the $0\nu\beta\beta$-regions of ^{116}Cd and ^{130}Te.

3.2.5 Neutrons

Neutrons are a problematic background source for the experiment because CdZnTe contains ^{113}Cd, which has a particularly high caption cross section for thermal neutrons. These reactions can release γ-rays up to 9 MeV. Neutrons evolve mainly from fission and (α,n)-reactions in concrete and rock. Furthermore, neutrons with higher energies result from cosmic muons. Fast neutrons interact via scatter reactions. They can transfer parts of their energy to other nuclei by elastic scattering. Also, inelastic scattering is possible which activates the interaction partner, so that photons are emitted. Both reactions lead to unpredictable energy depositions in

the detector material. Therefore, it is indispensable to shield the experiment from neutrons and muons as good as possible.

3.3 The Detectors

The detectors used for the COBRA experiment consist of cadmium-zinc-telluride (CdZnTe). Zn and Cd are contained in a ratio of Zn:Cd = (0.07 - 0.11):(0.89 - 0.93). In addition to the typical advantages of semiconductors as mentioned in section 3.1, CdZnTe semiconductors have the advantage of a large bandgap, so that they can be operated at room temperature. Two different designs for the large-scale experiment are still under investigation. One of them is an array consisting of $40\times40\times40$ 1 cm^3 CdZnTe coplanar grid detectors, enriched to 90% in ^{116}Cd. Each CdZnTe-crystal has a mass of 6.5 g. This would yield a total amount of 420 kg of detector material, which could achieve sensitivities below 50 meV within 10 years of measuring time assuming a background of 5×10^{-4} $\frac{\text{counts}}{\text{keV}\cdot\text{kg}\cdot\text{a}}$ at an energy resolution of 1% [Col06]. Unfortunately, this type of detector is only capable of measuring the total energy deposition with no tracking information. The other proposed design uses pixelated detectors. This type of detector would yield very precise tracking capabilities (depending on the pixel size) and can therefore identify a large amount of background signal because different types of particles can be identified by their topology. Moreover, measurement of the angular distributions and the single-electron spectra can provide a better understanding of the underlying physical processes. On the other hand, the requested readout electronics are obviously much more complex and thus demanding for pixelated detectors than for coplanar grid detectors as described in the following section.

3.3.1 The CdZnTe Coplanar Grid (CPG) Detectors

Cadmium-Zinc-Telluride detectors can be produced with a very good energy resolution. Depending on their size, temperature, the applied high-voltage and the price, CdZnTe detectors are available with an energy resolution of 1.5-3% at 2.6 MeV, but energy resolutions down to 0.9% at 2.8 MeV have been achieved [Col05]. Especially in the low-energy region, the energy resolution can be further improved by a slight cooling of the detectors down to 0°C since cooling reduces the leakage current [Col05]. CdZnTe has a bandgap of 1.57 eV and a pair creation energy of 4.64 eV [EVP].
The detectors are available in the Coplanar Grid design depicted in Fig. 3.2. When a particle enters a semiconductor, electrons are excited from the valence band into the conduction band, leaving holes in the valence band that act as positively charged particles. The electrons and holes act as quasi-free particles within the semiconductor. Applying a voltage to the semiconductor enables collection of the charge carriers. In CdZnTe, holes have a much lower mobility than electrons

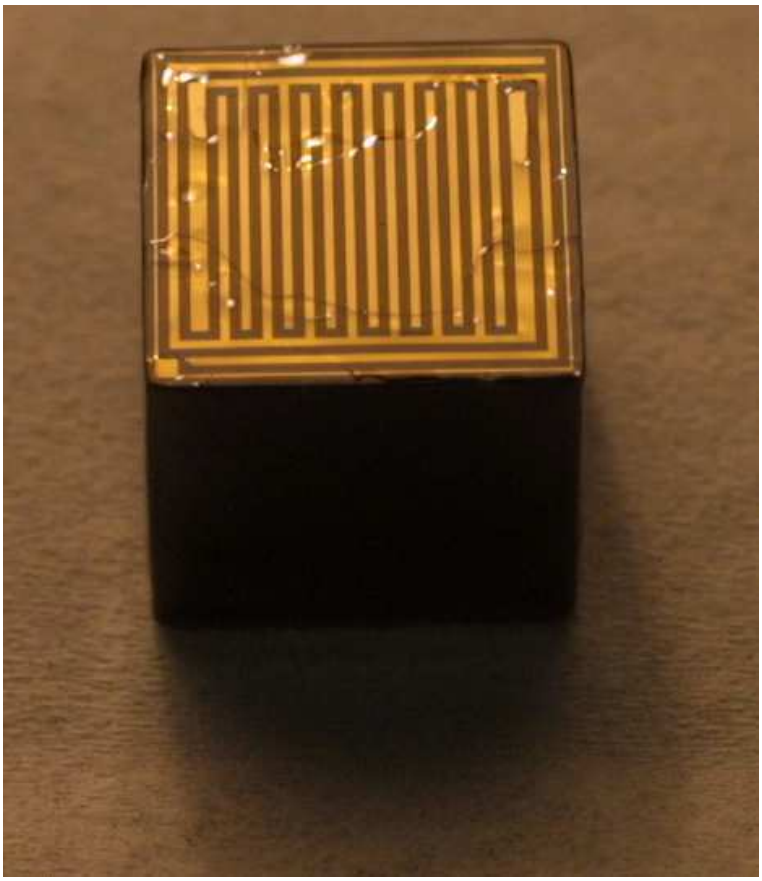

Figure 3.2: Picture of the coplanar grid design of a colorless passivated 1 cm^3 CdZnTe detector [COB].

and therefore much larger collection times, which results in incomplete charge collection depending on the interaction depth. In the CPG design, the anode forms two interleaved electrodes (see Fig. 3.2) with a small bias voltage in between. One of those electrodes is connected to ground and is called collecting anode (CA). The other electrode is called non-collecting anode (NCA) and is slightly negatively charged, resulting in a small bias voltage between the two anode electrodes, the grid-bias [Koe08, Luk95]. The grid-bias creates an electrostatic potential around the anode electrodes as shown in Fig. 3.3 that is small compared to the voltage between the anodes and the plane cathode. Therefore, the CA and NCA signals are almost identical for interactions within the detector volume except for those interactions that occur very close to the anode side. In that case, almost the whole signal is obtained by the collecting anode due to the potential resulting from the grid-bias. As a result, the difference between the two anode signals is nearly independent of the interaction depth within the detector but only depends on the energy of the interacting particle. Both the CA and the NCA are read out sep-

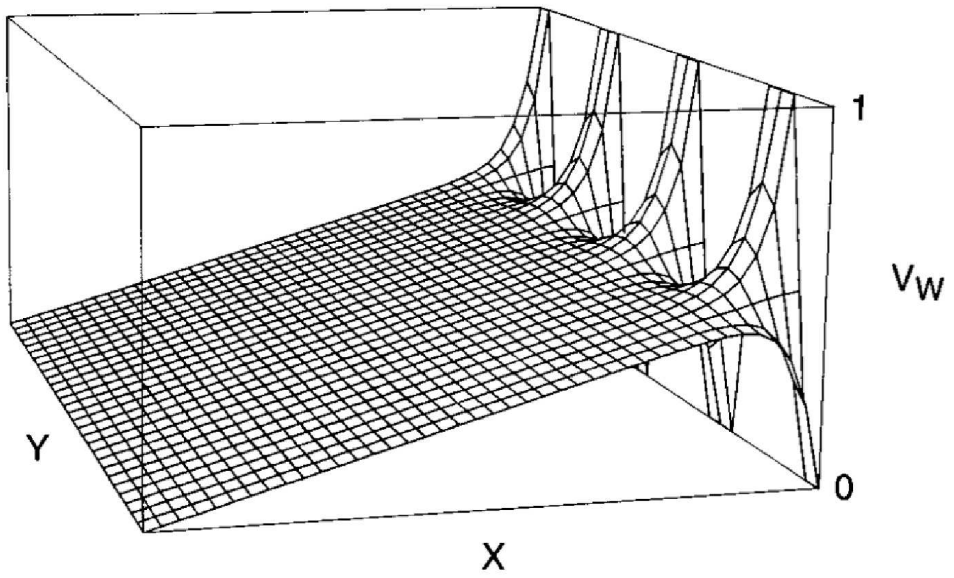

Figure 3.3: Potential distribution around one of the grid electrodes within a CPG designed detector. The grid-bias only affects the potential at very small distances from the electrodes [Luk95].

arately and the difference is calculated afterwards. Cooling the detectors to 0 °C while applying a larger grid-bias could improve the energy resolution by a factor 2 [Col05].
In order to protect the detectors from damage and to keep them from degrading, a passivation layer is implemented. The first measurements at LNGS have been performed with four detectors produced by eV-PRODUCTS that were coated with a red passivation. The composition of the passivation is kept secret by the manufacturer. Within test studies and measurements, the passivation layer has been identified as a major background contribution, so for further measurements, it had to be replaced [Col06]. Two proposals have been made for the new passivation paint: One passivation is a colorless paint fabricated by eV-PRODUCTS. The other option is provided by the Freiburg Material Research Center: They developed an alternative etching method with ammonium fluoride and BCB-Cyclotene. Both passivations have reduced the background significantly compared to the red passivation. Their contamination level has been determined at the low background counting facility at LNGS and is shown in table 3.3. A comparison of both passivations has not yet been completed but is in progress in order to choose the most appropriate one. This thesis deals with the background spectrum of the colorless passivated detectors.

Table 3.3: Activity of the Cyclotene and the colorless passivation determined in the low background counting facility at LNGS. Left: Activity A of the cyclotene paint. Right: Activity A of the colorless passivation.

Isotope	A (Bq/kg)	Activity (g/g)	A (Bq/kg)	Activity (g/g)
^{226}Ra	(2.1 ± 0.1)	$(1.7 \pm 0.1) \cdot 10^{-7}$	<0.81	$< 4.5 \cdot 10^{-8}$
^{234}Th	(1.1 ± 0.3)	$(8.5 \pm 2.5) \cdot 10^{-8}$	<1.5	$< 1.2 \cdot 10^{-7}$
^{234m}Pa	(1.6 ± 1.0)	$(1.3 \pm 0.8) \cdot 10^{-7}$	<4.3	$< 3.5 \cdot 10^{-7}$
^{235}U	(0.17 ± 0.03)	$(3.0 \pm 0.5) \cdot 10^{-7}$	$< 15 \cdot 10^{-3}$	$< 2.6 \cdot 10^{-8}$
^{228}Ra	(1.1 ± 0.1)	$(2.7 \pm 0.2) \cdot 10^{-7}$	<0.18	$< 4.5 \cdot 10^{-8}$
^{228}Th	(0.73 ± 0.07)	$(1.8 \pm 0.2) \cdot 10^{-7}$	<0.19	$< 4.7 \cdot 10^{-8}$
^{40}K	(6.9 ± 0.8)	$(2.2 \pm 0.3) \cdot 10^{-8}$	<1.0	$< 3.4 \cdot 10^{-5}$
^{137}Cs	$< 15 \cdot 10^{-3}$	—	$< 56 \cdot 10^{-3}$	—
^{60}Co	$< 15 \cdot 10^{-3}$	—	$< 72 \cdot 10^{-3}$	—

3.3.2 Pixelated Detectors

Pixelated detectors seem to be the convenient alternative compared to CPG detectors (see Fig. 3.4). Their additional capability of particle tracking enables particle identification by track length and energy deposition along the track as shown in Fig. 3.5. Alpha particles deposit all of their energy within a few neighboring pixels while beta particles deposit their energy along a connected track. Because gammas do not carry electromagnetic charge, their energy deposition is distributed along a track of disconnected pixels. Muons, which are negatively charged, create a straight connected track. This particle identification would allow reduction of a large amount of background not only by identifying the particles themselves, but also by relating coincident events from the natural decay chains to certain characteristic signatures.

For the purpose of particle tracking, simulations have shown that the pixels of the detectors have to be as small as 200 μm at the most. One major drawback of pixelated detectors is the necessity for a large amount of sophisticated and compact electronics in order to be able to read out the pixels separately. Furthermore, it is not yet completely certain if the segmenting of the detector leads to additional background contributions [Zub01].
Pixelated detectors are still in the development phase and will therefore not be considered within this thesis. Simulations and further measurements have to be performed to get a better understanding of the detector response.

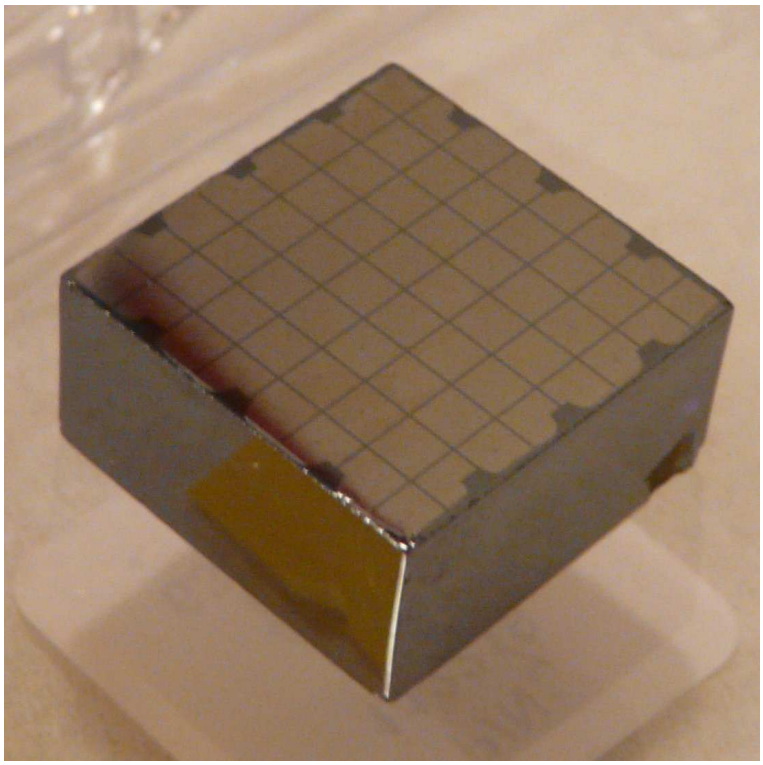

Figure 3.4: Pixel detector from St. Louis group. The Volume of the CdZnTe crystal is $2\times2\times1\,\mathrm{cm}^3$. It consists of 8×8 pixels [COB].

3.4 The Experimental Setup

3.4.1 Status and Shielding of the CPG Detectors

In 2001, the COBRA experiment was proposed by Kai Zuber [Zub01]. Due to the large amount of environmental background on the surface, the experiment can only be operated inside an underground laboratory. The COBRA experiment is currently located at LNGS underground laboratory, which contributes a great part to background reduction by providing 3500 mwe[5] of shielding [Col08]. It reduces the hadronic component of cosmic rays completely and the muon-flux by six orders of magnitude.
For the readout of the CdZnTe detectors, the coplanar grid design as described in section 3.3.1 has been chosen. The current setup consists of eight $1\,\mathrm{cm}^3$ CdZnTe detectors: Four of them are passivated with a clear passivation paint developed by eV-PRODUCTS and the other four detectors are passivated with the passivation method developed by Freiburg Material Research Center (see section 3.3.1). The detectors are embedded inside a holder structure made of Polyoxymethylene, which is a plastic called POM that is very radiopure. This holder structure contains 4×4

[5]mwe = meters of water equivalent

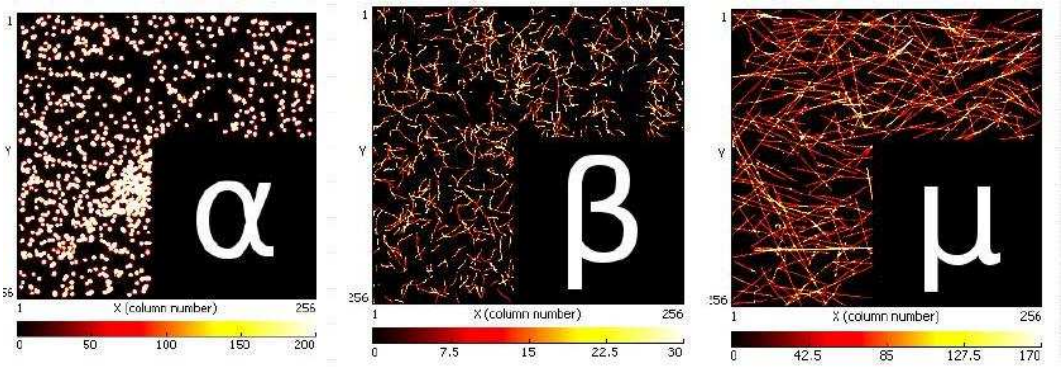

Figure 3.5: Signals of different particles within a 55 μm pitch pixelated Si-detector. One can clearly distinguish between alpha particles that deposit their full energy within one or two pixels (left), beta particles with energy deposition along a connected trace (middle), and muons with an energy deposition along a straight line (right) [Zub10b].

spaces for the individual detectors (see Fig. 3.6).
The detector contacts are made by gluing very thin, ultra-clean gold wires to the gridded anode with silver lamellas in acetone. To protect these contacts, they are covered with Uhu-Hart glue. Rg-178 cables are used to connect the detectors to the preamplifiers as well as for voltage supply. The POM holder is located within a $40 \times 40 \times 50\,\mathrm{cm}^3$ brick made of electropolished copper called the NEST which provides space for four layers of POM holder structures. It is therefore capable of holding a total number of 4×16 detectors (see Fig. 3.7). The NEST is shielded by another 10 cm of copper and 20 cm of radiopure lead to further reduce external neutrons and gammas. Teflon tubes feed into the NEST for easy energy calibration of the detectors by simply inserting calibration sources and for nitrogen flushing [Col06]. This setup is located inside a Faraday cage made of very clean copper in order to shield the experiment from electronic disturbances. On the outside of the Faraday cage, the neutron shield is located. The neutron shield consists of boron-loaded polyethylene plates of 7 cm thickness and further 20 cm of paraffin wax at the bottom. Better neutron shieldings consisting of different numbers of layers and different materials are still under investigation. For a more detailed description, see [Hei10]. The whole setup is shown in Fig. 3.8 All electronics are kept outside the neutron shielding except for the preamplifiers. They are located between the lead and the Faraday cage in order to keep the connection cables as short as possible [Col06]. The detectors are constantly flushed with pure nitrogen in order to eliminate or at least strongly suppress radon background. Also, operating the detectors in liquid scintillator is under investigation because this could act as an active veto counter for background events [Col05]: When a charged particle enters the setup from outside, it first has to pass through the scintillator before reaching the detector. The scintillator generates a light pulse that can be collected

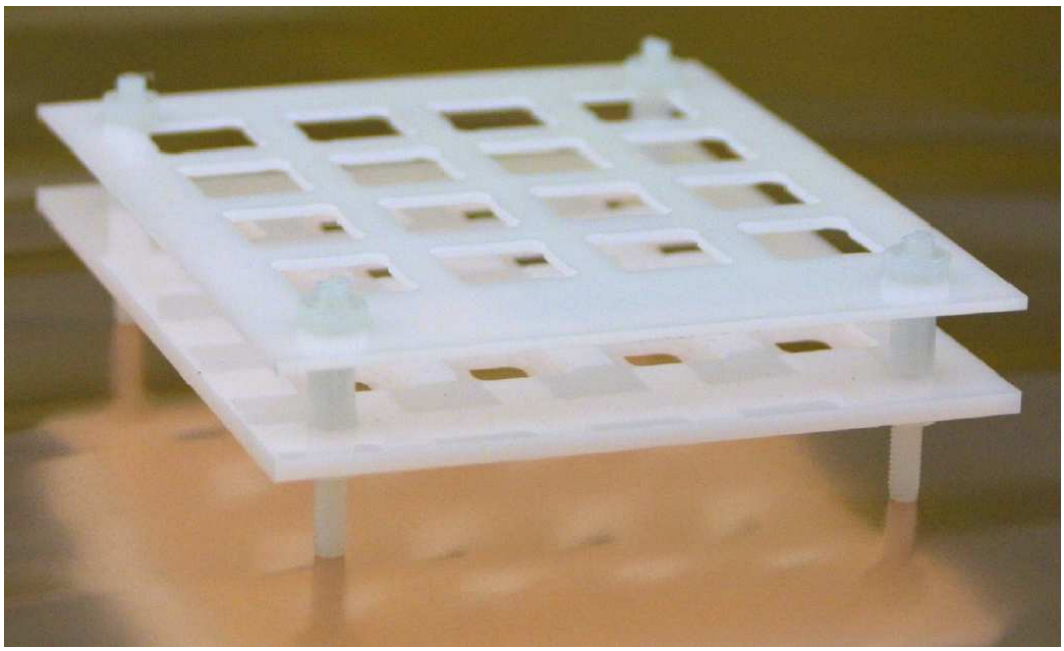

Figure 3.6: POM holder structure capable of holding sixteen detectors [COB].

with photomultipliers. That way, events entering the setup from outside can be recognized.
The detector bias is created with a custom-made cost-effective 64-channel high-voltage power supply developed by the University of Warwick. The detectors are operated at a high-voltage of -1500 V with a grid-bias of 20-40 V. Custom-built ADCs are used for signal read-out, each serving four crystals. A VME DAQ[6] system as described in section 3.4.2 is used for data acquisition. A VME is a computer bus standard. An upgrade to 64 detectors is planned and will take place after the choice for the passivation paint is made.

3.4.2 Data Acquisition

The detectors are read out with non-commercial, charge-sensitive preamplifiers placed in preamplifier boxes with implemented subtraction circuit in order to subtract the two anode signals as described in section 3.3.1 [Mue07] and [Koe08]. Eight-channel main amplifiers further amplify and shape the signal before it reaches the VME data acquisition system [Koe08]. The requirements for the readout system of this setup are such that no commercially available system could fulfill the needs of the experiment: A multi-channel peak-sensing device with more than eight channels and a resolution that exceeds 13 bit is needed. It must be self-triggering with time resolution $\leq 10\,\mu$s and a boolean logic input for a veto system [Col05].

[6]Data Acquisition

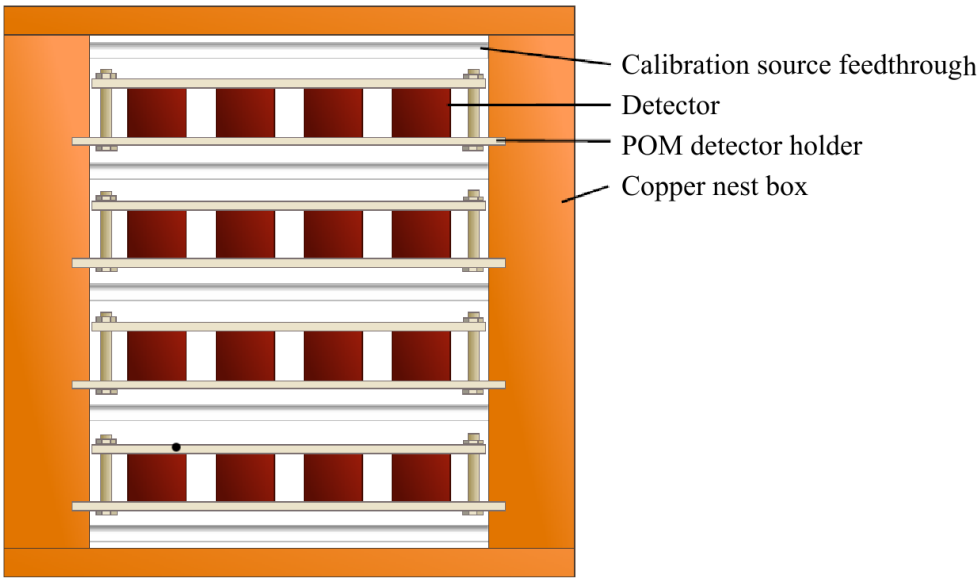

Figure 3.7: Schematical cross-section of the NEST structure filled with four POM holders, each containing 16 detectors. Teflon tubes feed into the nest in between the holders for easy calibration and nitrogen flushing. [Ree09]. The Pertinax has been replaced by a more radiopure plastic called POM

Furthermore, the trigger signal has to be connectible to other modules to enable upgrading the setup to a larger number of detectors. A prototype VME board has been developed for a 2×2 array [Col05]. It contains 4 peak sensing 14 bit ADC channels. The threshold and gain can be set by the VME system. When one signal exceeds the threshold, all channels are read out. A so-called "piggy back" – the analogue part of the module – contains a signal shaper and a peak holder[7] followed by a low-pass filter [Kie05]. The signal is converted within the piggy back.
The timer of the system is a 32-bit counter that has a precision of 8 μs and overflows to zero after 9.6 h. The timer is driven by the 16 MHz clock on the VME blackplane. 16 TTL[8] logic I/O[9] modules give information about the status of different components, such as a 20 μs long veto signal. The output of the piggy back is fed into an ADC chip[10]. A FIFO[11] buffer stores the values of the ADC chip together with the timer value and the 16 TTL levels. 64 bytes are available in total. The data can be read out in a block when an interrupt is generated [Col05]. For the setup at LNGS, a PPC[12] based TVME8240 is used for the VME controller.

[7] a commercial PKD01 chip is used as peak holder [Kie05]
[8] Transistor-Transistor Logic, performs the logic gating and the amplifying
[9] input/output communication system
[10] ADC chip: Type AD7865
[11] First In, First Out, a queue processing technique that processes data in the order they occurred.
[12] **P**ower **PC**

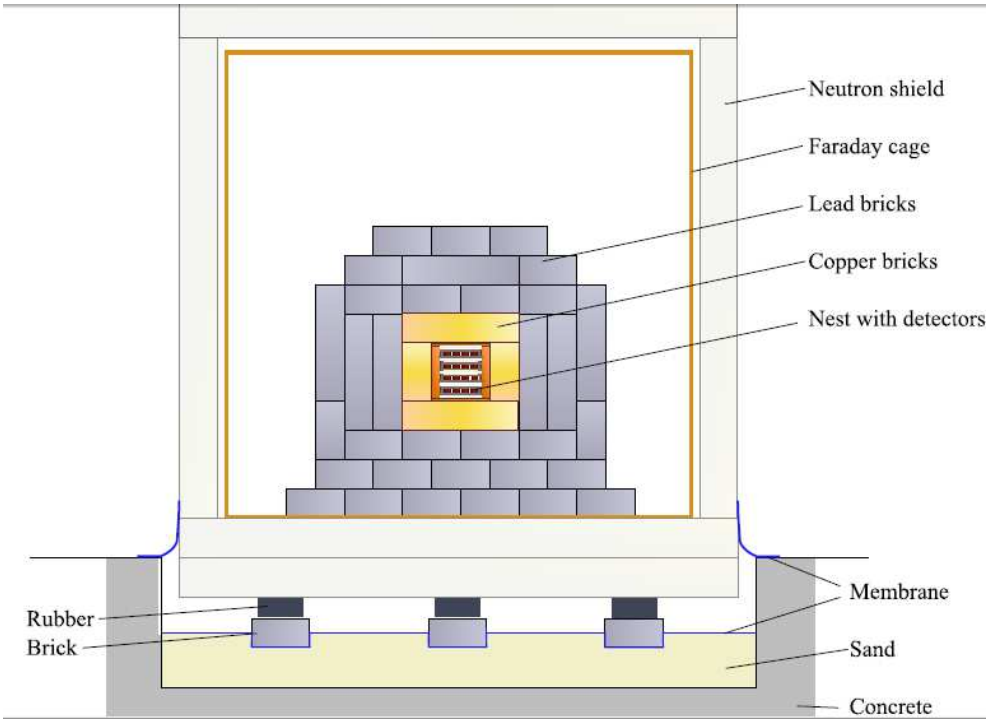

Figure 3.8: Experimental setup at LNGS. POM holders, each providing space for 16 detectors, are embedded within the copper NEST which is surrounded by copper and lead bricks. A Faraday cage shields the experiment from electronic disturbances. The whole setup is surrounded by a neutron shield [Ree09].

For testing purposes, a MC68040 based MVME-167 is used in Dortmund. An external electronic pulser may additionally trigger the readout of the ADC [Col06].

3.4.3 Development and Status of the Pixelated Detectors

Pixelated detectors seem to be the convenient alternative to CPG detectors because of their ability to simultaneously measure the energy deposition and the particle track through the detector. The electrodes of the detectors are segmented into pixels. The energy resolution of the detectors is not reduced by pixelization. Simulations showed that in order to obtain a reasonable spatial resolution, pixel sizes as small as 100-200 μm are required. These simulations also indicate that this would lead to a background suppression of almost 3 orders of magnitude [BF07]. With this pixelization, α-particles would mostly be single-pixel events while betas would deposit their energy along a connected track of about 1 mm length. High-energy gammas would hit several disconnected pixels along a track due to Compton scattering. This allows a discrimination between the different types of radiation. Background events including α-particles could be identified with an efficiency of almost 100% [Col07]. Of course a large amount of sophisticated and compact elec-

tronics is necessary for the readout of all the pixels. It is not clear if it is possible to achieve an acceptable depth resolution without a coplanar grid, but indications exist that a depth resolution of the order of 1 mm can be achievedwith pixelated detectors.
After measurements with two detectors purchased from eV-PRODUCTS for testing purposes has been completed and simulation tools have been improved, various pixelated detectors have been built: One detector with a pixel size of 625 μm and a total size of $2\times2\times0.5\,\mathrm{cm}^3$ and one with a pixel size of only 200 μm consisting of 100×100 pixels. The readout ASIC for these detectors is under development and plans exist to install them underground. First measurements of the detector response have been made, revealing a quite poor energy resolution of the small pixels (>10%) due to charge sharing between the pixels. Improving the energy resolution of the pixels is still a work-in-progress [Col10].
Furthermore, a CdTe TimePix detector has been purchased. The size is $1.4\times1.4\times0.1\,\mathrm{cm}^3$, it consists of 256×256 pixels with 55 μm pitch, each provided with an analog circuitry and a digital counter. This detector is read out with an ASIC developed by the Medipix collaboration at CERN [Col08]. The TimePix detector can be operated in 3 different modes: It can count the number of events above threshold in each pixel, measure the energy deposition in time-over-threshold mode in each pixel or measure the time of arrival. One TimePix detector with 300 μm silicon sensor and a pixel pitch of 55 μm has been calibrated pixelwise and installed at the Felsenkeller low background laboratory[13], taking data in time-over-threshold mode with random readout trigger [Col09]. The results seem promising: One can distinguish between low-energy X-rays, high-energy electrons, alpha particles and muons as can be seen in Fig. 3.5 [Col09]. Another of these detectors has been installed at Mondane Underground Laboratory[14] in order to exclude most external background sources and to measure the contamination due to the setup.

3.5 Calibration

In order to correctly assign the signal from the ADC chip to the corresponding energy, an accurate energy calibration is indispensable. Furthermore, the energy resolution of the detectors can be determined by regarding the FWHM[15] of the calibration peaks. For this purpose, the spectra of different radioactive sources with well–known peak energies are taken with the detectors and the peaks are fitted. In order to easily insert the calibration sources into the setup, Teflon tubes lead into the NEST. Usually, calibration is performed with ^{57}Co, ^{22}Na and ^{228}Th sources, out of which ^{228}Th is the most important one because of the γ-peak at an energy of 2.615 MeV and numerous other γ-peaks occurring at lower energies.

[13] located in Dresden
[14] located between Modane and Bardonecchia at the border between France and Italy
[15] **F**ull **W**idth **H**alf **M**aximum

Both the energy resolution and the channel number of the ADC increase linearly with increasing energy.

3.6 Achievements

Even though the COBRA experiment is still in the research and development phase, several existing half-life limits could already be reached within an order of magnitude. A new world best limit could be observed for the $0\nu\beta^+$/EC-decay of ^{120}Te to the ground state (see Tab. 3.4) [D$^+$09].

Besides the investigation of various double beta decays, also the spectrum of

Table 3.4: List of half–life limits achieved by the COBRA experiment compared to the existing world–best limits [Zub10a]. The world-best half-life of ^{120}Te has been achieved by the COBRA experiment.

Isotope and Decay	$T_{1/2}$, COBRA	$T_{1/2}$, World Best
^{116}Cd to gs.	$9.4{\cdot}10^{19}$	$1.7{\cdot}10^{23}$
^{130}Te to gs.	$5.0{\cdot}10^{20}$	$3.0{\cdot}10^{24}$
^{130}Te to 536 keV	$3.5{\cdot}10^{20}$	$9.7{\cdot}10^{22}$
^{114}Cd to gs.	$2.0{\cdot}10^{20}$	$1.1{\cdot}10^{21}$
^{128}Te to gs.	$1.7{\cdot}10^{20}$	$1.1{\cdot}10^{23}$
^{64}Zn $0\nu\beta^+$/EC to gs.	$1.1{\cdot}10^{18}$	$4.3{\cdot}10^{20}$
^{64}Zn 0νEC/EC to gs.	$3.3{\cdot}10^{17}$	$1.1{\cdot}10^{20}$
^{120}Te $0\nu\beta^+$/EC to gs.	$\mathbf{4.1}{\cdot}10^{17}$	$1.9{\cdot}10^{17}$
^{120}Te 0νEC/EC to gs.	$2.4{\cdot}10^{16}$	$6{\cdot}10^{17}$
^{106}Cd $0\nu\beta^+\beta^+$ to gs.	$2.7{\cdot}10^{18}$	$2.4{\cdot}10^{20}$
^{106}Cd $0\nu\beta^+$/EC to gs.	$4.7{\cdot}10^{18}$	$3.7{\cdot}10^{20}$
^{106}Cd 0νEC/EC to gs.	$1.6{\cdot}10^{17}$	$3.5{\cdot}10^{18}$
^{106}Cd $0\nu\beta^+$/EC to 512 keV	$4.6{\cdot}10^{18}$	$2.6{\cdot}10^{20}$

the four-fold forbidden, non-unique β-decay of ^{113}Cd has been measured [Mue06]. Only three isotopes that can undergo such decays are known: ^{50}V, ^{113}Cd and ^{115}In. The spectrum of ^{113}Cd has an endpoint energy of about 320 keV and a natural abundance of 12.22 % [NUC]. With the COBRA experiment, a half-life of $(8.2 \pm 0.2(\text{stat})^{+0.2}_{-1.0}(\text{sys})) \cdot 10^{15}$ a was obtained [Mue06], which is in good agreement with [KMZ03]. With the current shielding, a background rate of $8\,\frac{\text{counts}}{\text{keV}\cdot\text{kg}\cdot\text{a}}$ [Hei10] could be achieved. This background rate needs to be reduced by at least 4 orders of magnitude in order to successfully achieve reasonable half-life limits on the $0\nu\beta\beta$-decays of ^{130}Te and ^{116}Cd.

3.7 Outlook: The 64k Array

For the future, a large-scale experiment is planned at LNGS in order to achieve the desired half-life sensitivity of 10^{25}-10^{26} years. The experiment is supposed to consist of 40×40×40 1 cm^3 CdZnTe semiconductors which will yield a total detector mass of about 420 kg. For the investigation of the $0\nu\beta\beta$-decay of ^{116}Cd, the detectors will be enriched to 90 % in ^{116}Cd. In order to obtain the desired sensitivity, sophisticated background reduction methods are required which are still under development and which are part of this work. Analytical background reduction methods such as timing-coincidence analysis are an important tool because they are the only possibility to reduce background occuring from radioactive activation of the detectors and can improve the total background rate whenever no further improvement of the shielding is possible. A special focus lies on an appropriate neutron shielding due to the large cross section for thermal neutron capture of ^{113}Cd. In addition, an active component to veto cosmic muons seems desirable. Development and improvement of an active shielding component is already in progress [Col06]. In order to obtain a sensitivity of 10^{26} years within a measuring time of 4 years, the whole shielding device including all the other background reduction methods need to achieve a background reduction down to at least 0.001 counts / (keV · kg · a) with an energy resolution of 2% in the region of interest (see Fig. 3.1). This requires a maximum ^{238}U and ^{232}Th crystal contamination of 10^{-3} mBq/kg, a contamination level of the POM holder of less than 10^{-2} mBq/kg and a ^{210}Pb surface contamination of the crystals of no more than 10^{-7} mBq/kg [Col06].

Chapter 4

Data Analysis

In this chapter, the data taken by the colorless passivated detectors between January 2008 and December 2009 are analyzed with respect to reduction of the background arising from naturally occurring isotopes and investigation of the low-energy spectrum, which is dominated by the decay of ^{113}Cd.
In section 4.1, the spectrum of the data taken at LNGS with four detectors that were not flushed with nitrogen is discussed. Section 4.2 explains the method of timing-coincidence analysis and describes the relevant timing-coincidences suitable for this analysis. In section 4.2.1, simulations of the investigated decay sequences are discussed. The simulations are used to verify the validity of the method of timing-coincidence analysis and enable determining its efficiency. The background of the $0\nu\beta\beta$-region of ^{116}Cd and ^{130}Te arising from the isotopes of the natural decay chains is investigated: On the one hand, the detector surrounding materials such as air, cabling and even shielding components can contain radioactive materials that induce a signal and therefore contribute to the background. This is called external contamination and can especially be seen in the datasets of section 4.1 not flushed with nitrogen. The external contamination will be investigated in section 4.2.2. It can be reduced by either a better shielding, the use of more radiopure materials or nitrogen flushing of the detectors. On the other hand, the detectors themselves contain isotopes from the natural decay chains that produce a background signal. This is called intrinsic contamination. As the intrinsic contamination arises from isotopes that are encapsulated within the detectors, conservative background reduction methods such as shielding and nitrogen flushing are not able to reduce this background contribution. The intrinsic contamination of the detectors poses a threat to the success of the experiment because the signal that they produce is, depending on the extent of the detector contamination, larger than the $0\nu\beta\beta$-signal which can accordingly not be observed. It is demonstrated that this problem can be solved by timing-coincidence analysis, which does not reduce the total background by a certain percentage, but by the absolute value of the intrinsic contamination of the detectors - a feature that becomes more valuable with improving the absolute

background rate. Accordingly, an investigation of the intrinsic contamination of the detectors is only possible for runs taken with N_2 flushed detectors and is the subject of section 4.2.3. The discussion involved with timing-coincidence analysis is closed with a short summary in section 4.2.4
Section 4.3 deals with the spectral shape of the decay ^{113}Cd$\rightarrow$ ^{113}In, which is a rare process classified as four-fold forbidden, non-unique β-decay. In section 4.3.1, the spectrum taken with four colorless passivated detectors during the measuring period of 2009 will be compared to a theoretical model developed by [MAS06] in two different ways: The first part of this section will compare the model with the data by making a χ^2-test and therefore determining the best χ^2-value. In the second part of this section, the best position of the model will be determined by the expected rate of ^{113}Cd-decays during the measuring period. In section 4.3.3, a short summary of the investigation of the spectral shape of ^{113}Cd is given.

4.1 The Total Spectrum of the Runs without N_2 Flushing

Figure 4.1 shows the total background spectrum taken by the four colorless passivated detectors between March 21^{st} and July 7^{th} in 2008 that were not flushed with nitrogen. The data add up to a total amount of 64.95 kg · h. The spectrum contains the different background components of the detector signal.
The high-energy region of the spectrum reveals two dominant peaks: One at

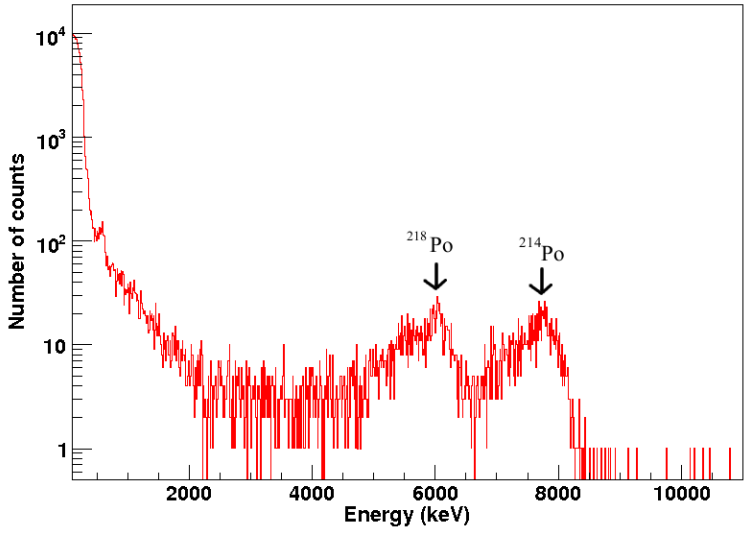

Figure 4.1: Total energy spectrum measured by four colorless passivated CdZnTe detectors. The measuring time is 64.95 kg · h.

5.835 MeV and one at 7.555 MeV. The peaks are strongly broadened because they

mainly arise from particles entering the detectors from outside. Furthermore, the crystals can contain "'bad regions"', which are regions within the detector volume that do cot produce a signal when energy is deposited. Passing through the surrounding air or the passivation layer, they deposit part of their energy. This also leads to an energy reduction of the peak maxima. The peak that occurs at 5.835 MeV can be assigned to the α–decay of ^{218}Po, which is emitted at an energy of 6.002 MeV [NUC]:

$$^{218}\text{Po} \rightarrow {}^{214}\text{Pb} + \alpha. \tag{4.1}$$

The second peak that is visible in the high-energy spectrum occurs at an energy of 7.555 MeV and can be identified as α-particles occurring from the decay of ^{214}Po at 7.687 MeV [NUC]:

$$^{214}\text{Po} \rightarrow {}^{210}\text{Pb} + \alpha. \tag{4.2}$$

Zooming into the low-energy region of the spectrum, which lies between 0 and 1600 keV, reveals two more, comparably small peaks (see Fig. 4.2). One of those peaks is slightly visible at an energy of 335 keV and can be identified as γ-decay of an excited ^{214}Pb that is emitted at 351.5 keV according to [Ree09]. The other peak that occurs at 581 keV turns out to be the 609.3 keV de-excitation γ of excited ^{214}Bi [Ree09]. Also visible is the shoulder of the four-fold forbidden non-unique β-decay of ^{113}Cd at energies below 316 keV that is investigated in section 4.3. The appearance of ^{214}Pb, ^{214}Po and ^{214}Bi in the spectrum clearly reveals the fact that the major background arises from the ^{238}U decay chain. The reason for the increased occurrence of isotopes from the ^{238}U chain is the existence of ^{222}Rn, a daughter nuclide of ^{238}U, within the surrounding air as described in section 3.2. The presence of radon in the air motivates the use of timing-coincidence analysis for background reduction, because many of the events in the $0\nu\beta\beta$-signal region arise from the daughter nuclides of ^{222}Rn, mostly ^{214}Bi, which is the most suitable isotope for timing-coincidence analysis. Moreover, the effect of the ^{222}Rn-contamination demonstrates the necessity of constant nitrogen flushing of the detectors which eliminates most of the radon-induced events.

4.2 A Background Reduction Technique: Timing-Coincidence Analysis

As mentioned in section 3.2, some isotopes occurring within the natural decay chains have a very characteristic decay-signature that is easy to identify by timing-coincidence analysis. The principle of timing-coincidence analysis is the following: Search the dataset for particle events within a reasonable range around the emitted particle energy, and afterwards search for the expected particle energy from the decay of the generated daughter nuclide within a reasonable timespan, which is, depending on the investigated coincidence, about five half-lives of the coincidence

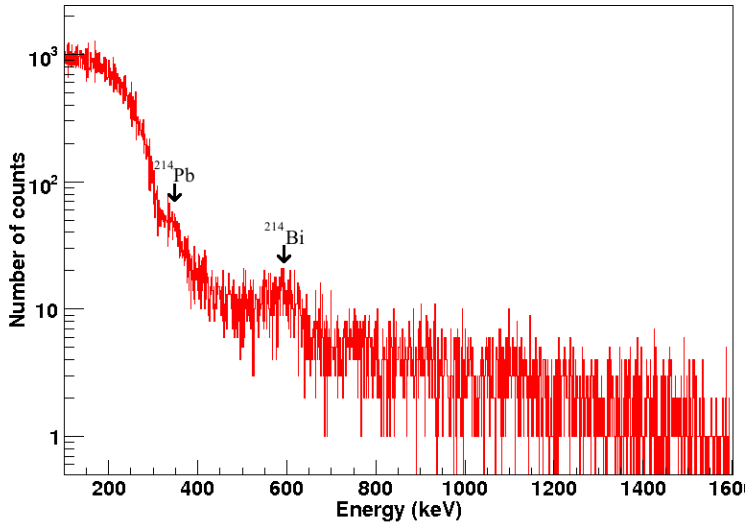

Figure 4.2: Low-energy region of the spectrum measured by four colorless passivated CdZnTe detectors. The measuring time is 64.95 kg · d. Two Peaks are visible: One at 335 keV and one at 581 keV that can both be identified as de-excitation gamma-particles of ^{214}Bi [Ree09]. Also visible is the shoulder of ^{113}Cd at energies below 316 keV.

of interest. Within this timing-cut, 99.33 % of the events of the investigated coincidence are included

For the COBRA experiment, the most suitable timing-coincidence is the $^{214}\text{Bi} \rightarrow {}^{214}\text{Po}$ coincidence due to its particularly short half-life of only 164.3 μs [NUC]. It is still worthwhile to search the data for other timing-coincidences in order to get an estimate on the contamination of the detectors with isotopes from other natural decay chains. A summary of all the investigated timing-coincidences as employed in this thesis, their characteristic energies and half-lives is given in Table 4.1.

4.2.1 Monte-Carlo Simulations of the Decays under Investigation

Before looking at real data, it is indispensable to analyze simulations of the investigated coincidences to gain a complete understanding of their energy signature inside the detector as used in the COBRA experiment. The behavior of the decays of interest within the detector setup were simulated using GEANT4[1] and VENOM[2]. Simulations of the decays of $^{214}\text{Bi} \rightarrow {}^{214}\text{Po}$, $^{214}\text{Po} \rightarrow {}^{210}\text{Pb}$, $^{212}\text{Bi} \rightarrow {}^{208}\text{Tl}$, and $^{208}\text{Tl} \rightarrow {}^{208}\text{Pb}$ have been performed by the University of Dortmund and are shown

[1] GEANT4 is a toolkit for the simulation of the passage of particles through matter [GEA].

[2] VENOM is a GEANT4 application designed by the COBRA collaboration for the simulation of semiconductor detector based double-beta decay experiments [VEN].

Table 4.1: Timing-coincidences that occur within the natural decay chains and that are suitable for coincidence analysis. Also shown are the types of the emitted particles, their energies and the half-lives of the second decay of the coincidences [NUC].

Coincidence	Decay Chain	1st Event	E_1 (MeV)	2nd event	E_2 (MeV)	$T_{1/2}$
$^{223}\mathrm{Ra} \xrightarrow{\alpha} {}^{219}\mathrm{Rn} \xrightarrow{\alpha} {}^{215}\mathrm{Po}$	^{235}U	α	5.747 5.716 5.607 5.540	α	6.819 6.553 6.425	3.96 s
$^{220}\mathrm{Rn} \xrightarrow{\alpha} {}^{216}\mathrm{Po} \xrightarrow{\alpha} {}^{212}\mathrm{Pb}$	$^{232}\mathrm{Th}$	α	6.288	α	6.778	0.145 s
$^{212}\mathrm{Bi} \xrightarrow{\alpha} {}^{208}\mathrm{Tl} \xrightarrow{\beta} {}^{208}\mathrm{Pb}$	$^{232}\mathrm{Th}$	α	6.050 6.090	β	<1.706	184.98 s
$^{222}\mathrm{Rn} \xrightarrow{\alpha} {}^{218}\mathrm{Po} \xrightarrow{\alpha} {}^{214}\mathrm{Pb}$	$^{238}\mathrm{U}$	α	5.490	α	6.002	183 s
$^{214}\mathrm{Bi} \xrightarrow{\beta} {}^{214}\mathrm{Po} \xrightarrow{\alpha} {}^{210}\mathrm{Pb}$	$^{238}\mathrm{U}$	β	<3.247	α	7.686	164.3 μs

in Fig. 4.3-4.6. The simulations were performed assuming ideal crystals with perfect energy resolution and homogeneously spread decays throughout the crystal volume. In Fig. 4.3, the simulation of the β-decay $^{214}\mathrm{Bi} \xrightarrow{\beta} {}^{214}\mathrm{Po}$ is shown. The β-spectrum shows many β-particles at low energies, slightly increasing to a maximum at 237 keV and exponentially decreasing with higher energies. Most of the β-particles from ^{214}Bi are emitted at energies above 0.5 MeV [NUC]. The maximum at 237 keV occurs because electrons have a non-vanishing probability to leave the detector without depositing their full energy. This probability increases with increasing electron energy. A naive approximation of the maximum traveling distance d_{max} of electrons in matter [ARC] is given in nm by

$$d_{max} = \frac{5.2 \cdot 10^{-4}}{\rho} \cdot T^{\delta}, \tag{4.3}$$

where ρ=5.78 g/cm^3 is the density of CdZnTe [EVP] in g/cm, T is the kinetic energy of the electrons in eV and $\delta = 1.667$ for particles with T>1 keV. This approximation assumes electron energies above 1 keV and is derived from the Bethe-formula for electrons. In CdZnTe, this leads to a maximum traveling distance for electrons with an energy of 3.274 MeV of 6.5 mm. The COBRA-detectors have a size of $1 \times 1 \times 1\,\mathrm{cm}^3$, the probability that only a fraction of the electron energy is deposited is thus quite large. Figure 4.4 shows a simulation of the α-decay $^{214}\mathrm{Po} \xrightarrow{\alpha} {}^{210}\mathrm{Pb}$. 99.99% of the emitted α-particles have an energy of 7.686 MeV, the remaining 0.01% of the α-particles is emitted at 6.902 MeV. In the simulations, those peaks are shifted by 150 keV towards larger energies. By emitting an α, the nucleus gains a non-negligible momentum that is seen by the detector in addition

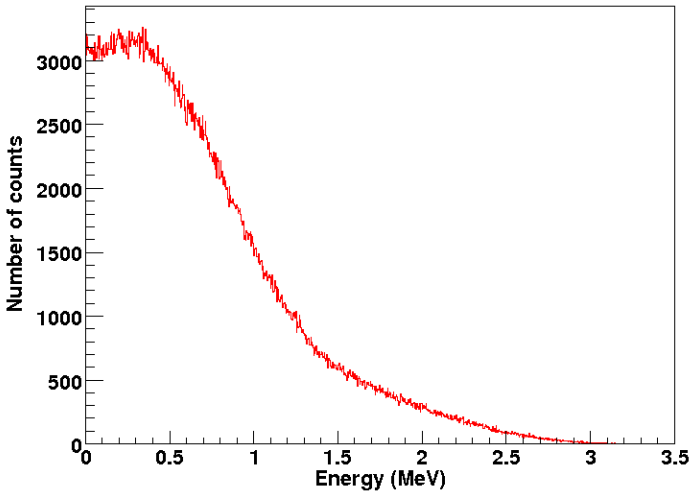

Figure 4.3: Simulation of the β-spectrum of decay $^{214}\mathrm{Bi} \rightarrow {}^{214}\mathrm{Po}$ within a $1\,\mathrm{cm}^3$ CdZnTe crystal. ^{214}Bi emits β-particles at energies up to 3.274 MeV, but most of them at energies smaller than 0.5 MeV. Above 0.5 MeV, the β-spectrum shows an exponential decrease.

to the α-energy. Accordingly, the 7.687 MeV α-peak is visible at 7.837 MeV and the 6.902 MeV α-peak occurs at 7.037 MeV. The constant part of the background arises from α-decays that occur very close to the detector surface: In that case, the α-particle can leave the detector without depositing the full amount of its energy. This background is constant because the probability for an α-decay to occur is the same for every distance to the detector surface. This contrast to the β-spectrum is shown in Fig. 4.3 and arises from the larger mass of the α-particles and the monoenergetic emission of the α-particles. α-particles desposit their energy within the detector by a few, energy-rich interactions with the detector atoms while β-particles interact with matter by a large number of low-energetic interactions, such as scatter-processes and the emission of bremsstrahlung [EIM].
In Fig. 4.5, a simulation of the two decay channels of ^{212}Bi is shown. With a branching ratio of 64.06 %, ^{212}Bi decays via β-decay: $^{212}\mathrm{Bi} \xrightarrow{\beta} {}^{212}\mathrm{Po}$. β-particles up to 2.248 MeV are emitted. This part of the decay dominates the low-energy region of the spectrum. As typical for β-decays, the spectrum is continuous with most events occurring at low energies. The high-energy part of the spectrum features the α-decay of ^{212}Bi: $^{212}\mathrm{Bi} \xrightarrow{\alpha} {}^{208}\mathrm{Tl}$. As a decay into excited states of ^{208}Tl is possible, various α-lines are visible: Table 4.2 shows the most intense α-lines arising from the decay with their relative intensity of the total α-decays of ^{212}Bi. In the simulation (Fig. 4.5), the peaks are shifted to higher energies due to the recoil of the nucleus and de-excitation particles from ^{208}Tl. The peak occurring at

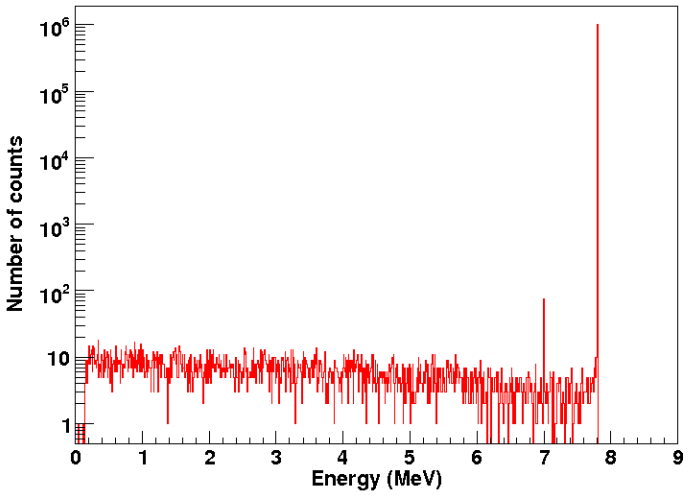

Figure 4.4: Simulation of the α-spectrum of the decay ^{214}Po $\rightarrow$ ^{210}Pb. Visible are two sharp α-peaks: One at 7.686 MeV and a smaller one at 6.902 MeV.

Table 4.2: Energies of the α-particles emitted by the decay ^{212}Bi$\rightarrow$ ^{208}Tl with their corresponding intensities [NUC].

Energy (MeV)	Intensity (%)
6.090	27
6.051	70
5.768	2
5.606	1

6.2 MeV contains both the 6.09 MeV and the 6.051 MeV α-particles. At 6.15 MeV, the 5.768 MeV peak is visible. This peak arises from the sum of the α-particle, the energy of the recoiling nucleus and two de-excitation Auger-electrons that are emitted by the excited ^{208}Tl. The 5.768 MeV α-particle is also responsible for the peak visible at 5.9 MeV. In this case, the de-excitation of the ^{208}Tl is accomplished by γ-particles that can escape the detector without significant energy deposition. The 5.606 MeV α-particle produces a peak at 5.8 MeV, due to the same reasons as above.
Figure 4.6 shows a simulation of the β-decay ^{208}Tl$\xrightarrow{\beta}$ ^{208}Pb. The β-particles have energies up to 1.796 MeV. A second shoulder arises at energies above 1.6 MeV because in addition to the β-particles, gamma-particles are produced with energies up to 2.614 MeV that deposit parts of their energy within the detectors so that the

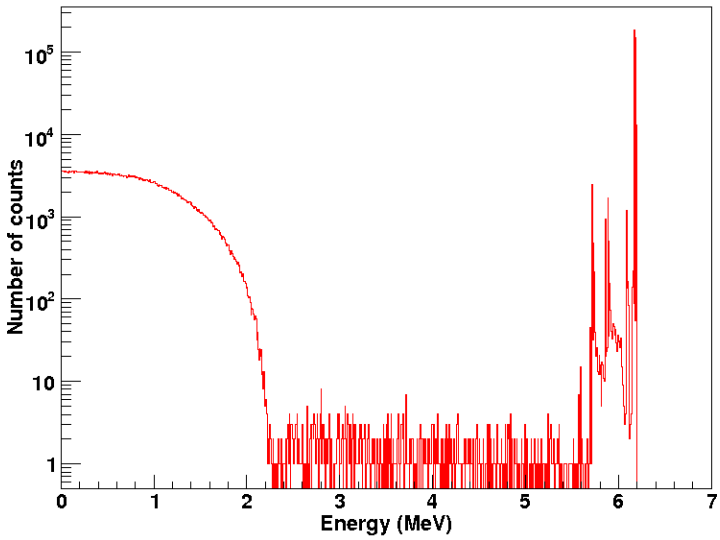

Figure 4.5: Simulation of the α- and β-decay ^{212}Bi. At low energies the spectrum of the β-decay of ^{212}Bi occurring with a probability of 64.06% is visible. The high-energy region reveals four α-peaks.

energy of both decays add up to a maximum of 4.410 MeV.
All simulations were employed to test the cuts that are used for timing-coincidence analysis in sections 4.2.2 and 4.2.3. This is especially important for the determination of the intrinsic contamination of the detectors (section 4.2.3), because the efficiencies of the cuts are determined by these simulations.

4.2.2 The Datataking Periods without Nitrogen Flushing

In order to get an impression on the external contamination of the detector surrounding materials and air with ^{214}Bi, ^{212}Bi, ^{222}Rn, ^{220}Rn, and ^{223}Rn, the timing-coincidence technique was applied to a dataset taken in 2008 with colorless passivated CdZnTe detectors that were not flushed with N_2 containing 36.51 kg · h of data.

4.2.2.1 External ^{214}Bi-Contamination

In order to find the characteristic coincidence $^{214}\text{Bi} \xrightarrow{\beta} {}^{214}\text{Po}$ from the ^{238}U chain, the dataset was searched for two signals with energies above 100 keV that occurred within 120-800 μs. In the case of this coincidence, the only necessary condition on the particle energies is that they must be above the detector threshold of 100 μs: The half-life is so short that it is not necessary to further constrain the particle energies because statistical events are very unlikely to occur within a timespan of 800 μs, which makes the timing-cut the most selective one.

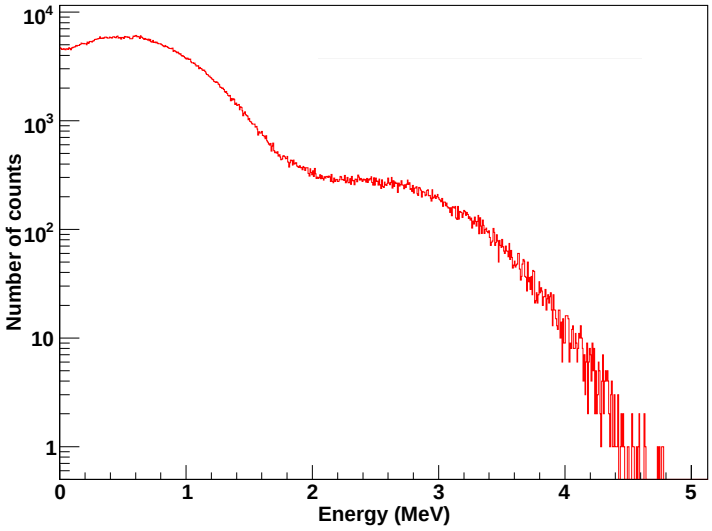

Figure 4.6: Simulation of the β-spectrum of the decay ^{208}Tl $\rightarrow$ ^{208}Pb. β-particles are emitted at energies up to 1.796 MeV. Additional γ-particles up to 2.614 MeV produce the shoulder above 1.7 MeV.

Within the dataset of the not N_2 flushed run, 379 supposedly ^{214}Bi-events were found. Figure 4.7 shows a correlation plot of the energy of the first event, E_β, which is assumedly a β-particle arising from the decay of ^{214}Bi vs. the energy of the second event, E_α, presumably an α-particle emitted from a ^{214}Po-nucleus. The secondly occurring events E_α are accumulated between 6 and 8 MeV, with only few events in the low-energy region. In contrast, the first events E_β occur at energies between 0 and 3 MeV, but most of them at low energies, which is in perfect agreement with the simulations of the decays of ^{214}Bi and ^{214}Po as depicted in Figs. 4.3 and 4.4. In order to confirm the assumption that the observed events arise from the decays of ^{214}Bi and ^{214}Po instead of being random events, it is useful to look at the time difference distribution between the first and second event. If the observed events belong to the timing-coincidence of ^{214}Bi, they follow the decay law [PRSZ06]:

$$N(t) = N_0 e^{-\lambda t}, \tag{4.4}$$

where N_0 is the number of investigated isotopes and λ is the decay constant, which is connected with the half-life $T_{1/2}$ as follows:

$$\lambda = \frac{\log 2}{T_{1/2}}. \tag{4.5}$$

Accordingly, the half-life of the decay can be determined by exponentially fitting the time-difference distribution. Figure 4.8 shows the histogram of the time

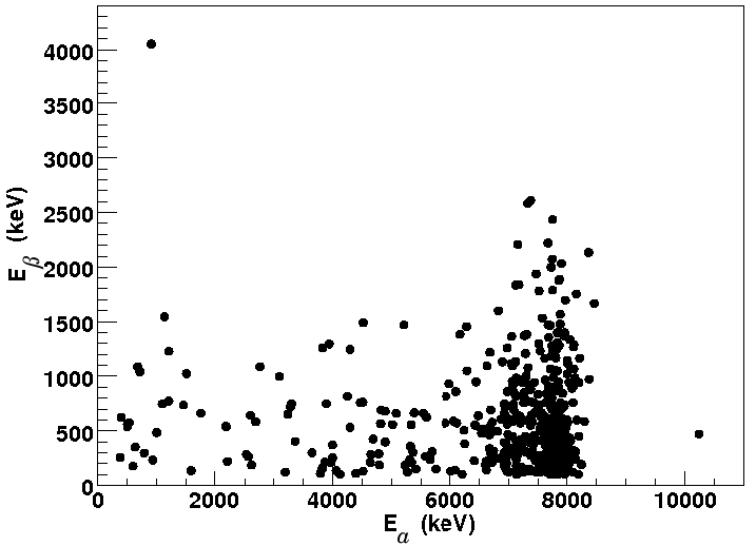

Figure 4.7: Correlation plot of second event energy vs. first event energy within the dataset taken with not N_2 flushed detectors during 2008 for the decay sequence ^{214}Bi $\rightarrow$ ^{214}Po.

differences Δt of all events separated by 120-800 μs within datasets of the runs without N_2 flushing. The number of events shows an exponential decrease with increasing time difference. The exponential fit yields a half-life of 164.5$\pm$7.5 μs, which is in perfect agreement with the ^{214}Po half-life of 164.3 μs as stated in Tab. 4.1. This impressively confirms the validity of the presented method: The events that were selected by the timing cut arise from the $^{214}\text{Bi} \xrightarrow{\beta} {}^{214}\text{Po} \xrightarrow{\alpha} {}^{210}\text{Pb}$ coincidence and are not random events.

In addition, the method of timing-coincidence analysis allows to look at the α- and β-spectra separately. Figure 4.9 shows the energy spectrum of the β-particles emitted by ^{214}Bi. The spectrum shows an exponential decrease with increasing energy in agreement with the simulations depicted in Fig. 4.3. As most of the ^{214}Bi-coincidence events arise from a contamination of the surrounding air, many β-particles have to pass some air and the passivation paint of the detectors. This leads to a reduction of the detected energy, which explains the shift of the whole spectrum towards lower energies compared with the simulated β-spectrum.

In Fig. 4.10, the energy spectrum of the α-particles from ^{214}Po is shown. For the same reasons as above, the α-particles loose some of their energy before reaching the detector. α-particles have a much lower penetration depth than β-particles, therefore this effect is even stronger visible in the α-spectrum: It leads to a broadening of the peak expected at 7.686 MeV and causes some events to occur at lower energies compared to the simulated ^{214}Po-spectrum as shown in Fig. 4.4. Nevertheless, most of the α-particles occur around 7.686 MeV, additionally

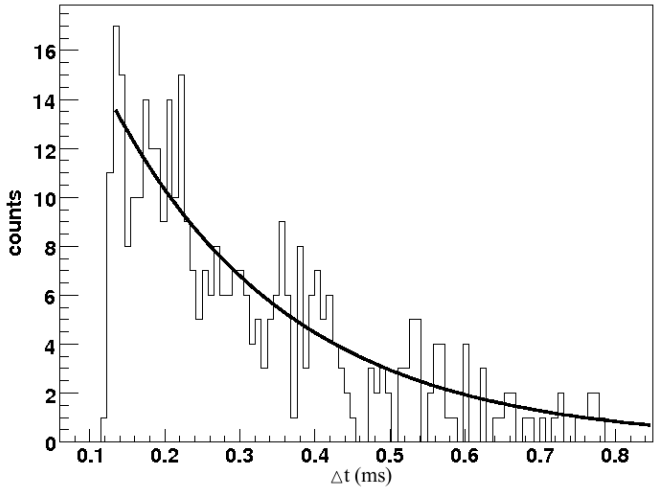

Figure 4.8: Histogram of time difference Δt between two events occurring within 120-800 μs in datasets of the runs not flushed with N_2. The energy is not constrained. With increasing time difference, the number of events decreases exponentially, indicating that the observed events are real $^{214}\text{Bi} \xrightarrow{\beta} {}^{214}\text{Po}$ events.

confirming that it was the $^{214}\text{Bi} \rightarrow {}^{214}\text{Po}$ coincidence that has been selected by the timing-coincidence method.

4.2.2.2 External ^{222}Rn- and ^{212}Bi-Contamination

After demonstrating the success of the timing-coincidence method on the very distinct ^{214}Bi-decay, now the limits of this method are shown. The decay $^{222}\text{Rn} \xrightarrow{\alpha} {}^{218}\text{Po} \xrightarrow{\alpha} {}^{214}\text{Pb}$ occurs within the same decay chain as the decay of ^{214}Bi. The first emitted particle is an α-particle with an energy of 5490 keV, followed by another α-particle with 6002 MeV. The half-life of this coincidence is 186 s. In contrast to the $^{214}\text{Bi} \rightarrow {}^{214}\text{Po}$ coincidence, random events are not unlikely to occur within this timespan. Therefore confining the time difference Δt between the two emitted α-particles is not sufficient in order to observe the coincidence while excluding random events and the time cut is not a selective criteria. Consequently, the observed energies additionally have to be restricted to adequate ranges. A reasonable time cut includes 3-5 half-lives of the coincidence in order to include 95 - 99.3 % of all events. The energy cuts are chosen to be about 5-10% around the emitted particle energy, in order to account for the energy resolution of the detectors. The cuts used to identify the decay sequence $^{222}\text{Rn} \xrightarrow{\alpha} {}^{218}\text{Po} \xrightarrow{\alpha} {}^{214}\text{Pb}$ within data of the runs without N_2 flushing are listed in

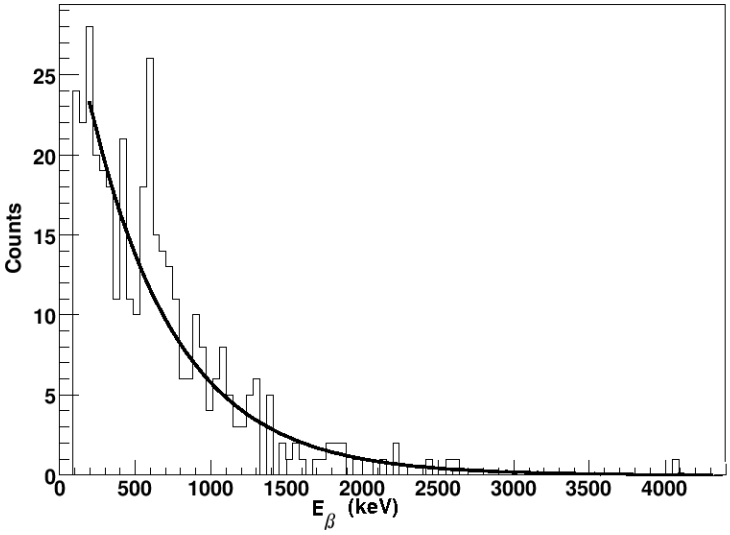

Figure 4.9: Energy spectrum of β-events from the datasets of the runs without N_2 flushing of 2008. The spectrum shows an exponential decrease with increasing energies, up to a maximum of 3.2 MeV. Compared to the simulated β-spectrum, this spectrum is shifted towards lower energies due to energy losses of the β-particles in the surrounding air, the passivation paint and the dead layer of the detectors.

Table 4.3. The whole dataset revealed 99 of 9540160 events within the cut ranges

Table 4.3: Cuts to identify the decay sequence $^{222}\mathrm{Rn} \xrightarrow{\alpha} {}^{218}\mathrm{Po} \xrightarrow{\alpha} {}^{214}\mathrm{Pb}$ within the runs without N_2 flushing performed in 2008.

Time Difference	First α-Energy	Second α-Energy
$1\,\mathrm{s} < \Delta t < 554\,\mathrm{s}$	$5000\,\mathrm{keV} < E_{\alpha 1} < 6000\,\mathrm{keV}$	$5500\,\mathrm{keV} < E_{\alpha 2} < 6500\,\mathrm{keV}$

defined in Table. 4.3, which corresponds to 0.001 % of all events. Figure 4.11 shows a correlation plot for the α-energies. The emitted α-particles have discrete energies, therefore the detector signal should be accumulated around the energies of 5.490 MeV and 6.002 MeV. In contrast to this assumption, both particles' energies are homogeneously distributed throughout the specified energy range. This indicates that the events selected by the cuts are random events instead of events arising from the decay $^{222}\mathrm{Rn} \rightarrow {}^{218}\mathrm{Po} \rightarrow {}^{214}\mathrm{Pb}$. A histogram of the observed time difference between the two events is an excellent test to answer the question whether the observed events are random or arise from the $^{222}\mathrm{Rn} \rightarrow {}^{218}\mathrm{Po} \rightarrow {}^{214}\mathrm{Pb}$ decay instead. If they arise from this decay sequence, an exponential fit will yield the half-life of ^{218}Po, which is 183 s. Figure 4.12 shows the histogram of the time difference between two events fulfilling the

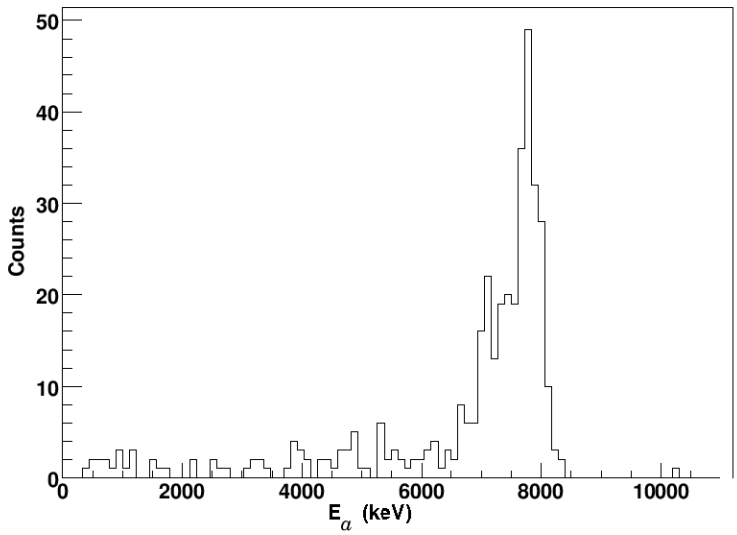

Figure 4.10: Spectrum of α-events from the dataset of the runs without N_2 flushing of 2008. The spectrum shows a peak at about 7.75 keV. This is in good agreement with the Q-value of the decay being 7.83 MeV [NUC]. Compared to the simulated α-spectrum in Fig. 4.4, the α-peak is broadened and some events occur at lower energies due to energy loss in the surrounding air, the detector passivation and the dead layer on the detector surface.

requirements of the cuts as described in Table 4.3. The histogram does not show an exponential behavior, which proves the assumption that most of the events are random events instead of events arising from the $^{222}\mathrm{Rn} \rightarrow {}^{218}\mathrm{Po} \rightarrow {}^{214}\mathrm{Pb}$ coincidence. This clearly demonstrates the need for background reduction. An analysis of the ^{222}Rn background is not possible without eliminating a large part of the background signal by nitrogen flushing of the detectors. The limiting factor of coincidence analysis for ^{222}Rn is the large half-life of 183 s. Within the timespan of the timing cut, which has to be at least three half-lives of the coincidence in order to be efficient, the probability for random events is too high, even if the energy ranges are restricted to the high-energy part of the spectrum. For the same reasons it is not possible to investigate the decay $^{212}\mathrm{Bi} \xrightarrow{\alpha} {}^{208}\mathrm{Tl} \xrightarrow{\beta} {}^{208}\mathrm{Pb}$ within datasets containing the runs without N_2 flushing, which is not shown in this thesis. The search for this decay is even more problematic due to the continuous β-spectrum of ^{208}Tl in the low-energy range where the background rate is much higher than the background rate in the high-energy range.

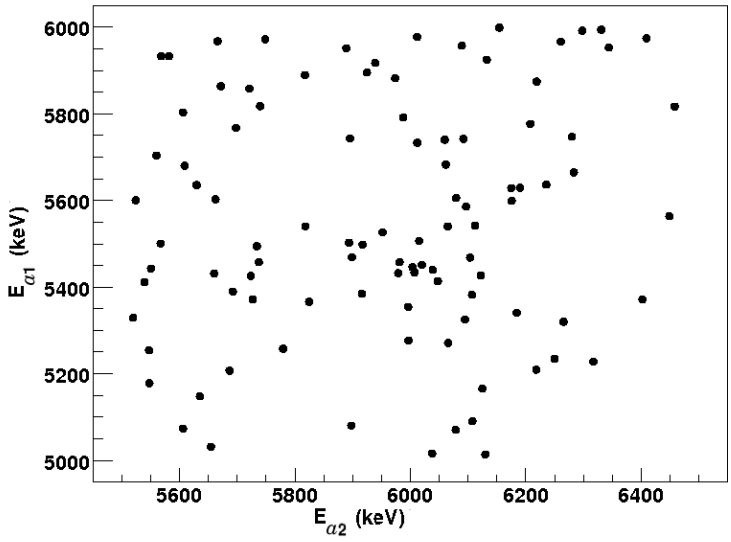

Figure 4.11: Energy correlation plot for the ^{222}Rn coincidence within the dataset containing the runs without N_2 flushing of 2008.

4.2.2.3 External ^{223}Ra-Contamination

The isotopic abundance of ^{235}U is only 1/138 of that of ^{238}U. Therefore, the number of background events arising from the ^{235}U decay chain is expected to be two orders of magnitude smaller than the number of background events arising from the ^{238}U chain. However, the ^{235}U chain provides one decay sequence that is suitable for timing-coincidence analysis: $^{223}\text{Ra} \xrightarrow{\alpha} {}^{219}\text{Rn} \xrightarrow{\alpha} {}^{215}\text{Po}$. This decay sequence has a half-life of 3.96 s and various α-energies as listed in Table 4.1. Searching the runs without N_2 flushing for events with an energy of 5.2-6.2 MeV followed by events with an energy of 6-7 MeV within 0.1-20 s revealed five events. Assuming that the number of ^{214}Bi events, which is 379 within this dataset, is representative for the appearance of ^{238}U, the expected number of events arising from decay sequences within the ^{235}U chain is three. Therefore, a result of five events seems realistic. By reason of smallness of the statistics in this case, it is not useful to investigate the histogram of the time differences between those events or to look at the energy correlation plot in order to confirm that these events really arise from the decay sequence $^{223}\text{Ra} \xrightarrow{\alpha} {}^{219}\text{Rn} \xrightarrow{\alpha} {}^{215}\text{Po}$. Due to the small abundance of this decay chain, a problematic background signal is not expected, but the fact that five possible events were found enhances the necessity for a nitrogen flushing system.

4.2.2.4 External ^{220}Rn-Contamination

Moreover, the dataset was searched for events arising from the decay sequence $^{220}\text{Rn} \xrightarrow{\alpha} {}^{216}\text{Po} \xrightarrow{\alpha} {}^{212}\text{Pb}$ from the ^{232}Th-chain. ^{216}Po has a half-life of 0.145 s.

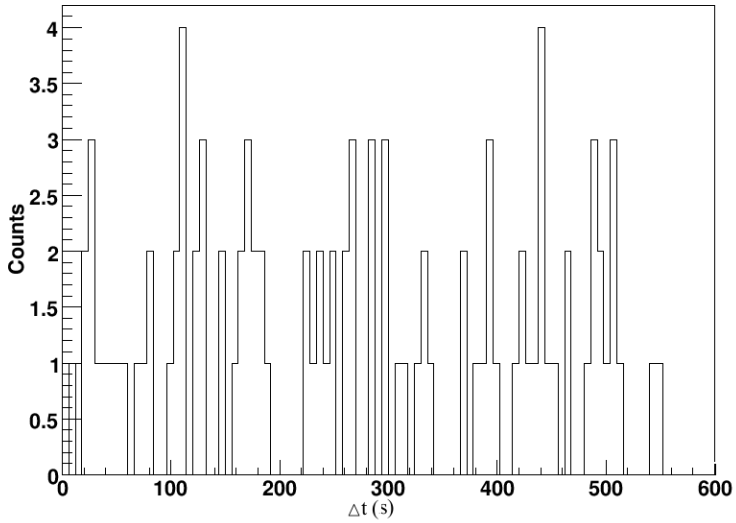

Figure 4.12: Histogram of time difference between two events fulfilling the cuts used to identify the decay $^{222}\mathrm{Rn} \rightarrow {}^{218}\mathrm{Po} \rightarrow {}^{214}\mathrm{Pb}$ as described in Table 4.3. No exponential behavior is visible, indicating that the selected events are random events instead of $^{222}\mathrm{Rn} \rightarrow {}^{218}\mathrm{Po} \rightarrow {}^{214}\mathrm{Pb}$ events.

Searching the dataset for events within the range 5-6 MeV followed by events with 6.5-7.5 MeV within 0.001-0.750 s revealed no events, indicating that the detector surrounding materials and air are not contaminated with ^{220}Rn. This is not very surprising. As mentioned in section 3.2, isotopes from the natural decay chains are encapsulated within materials such as concrete and rocks. Radon is a noble gas which is no longer chemically bound within those materials, so when it comes into existence, it starts to diffuse. ^{222}Rn, which occurs in the ^{238}U decay chain, has a half-life of 183 s. This is enough time for it to diffuse out of the material into the surrounding air. In contrast, ^{220}Rn has a half-life of 55.6 s, which is hardly enough time to diffuse to the material surface or into the surrounding air, so the ^{220}Rn remains inside those materials, where it decays. Therefore, the α-particles that are emitted are deposited inside the materials and do not reach the detectors.

Altogether, the results demonstrate the necessity for a nitrogen flushing system which dramatically reduces the large amount of background signal that disturbs timing-coincidence analysis. The large amount of events arising from an external ^{214}Bi-, ^{212}Bi- and ^{222}Rn-contamination can be strongly suppressed by installing a constant nitrogen flushing system to the COBRA setup. This was done in 2008 [Col08], so further analysis and discussions will be engaged with datasets taken with the N_2 flushed COBRA setup.

4.2.3 The Datataking Periods with Nitrogen Flushing

Since 2008, the detectors of the COBRA experiment are flushed with nitrogen. For this purpose, liquid nitrogen is evaporated and inserted into the setup through teflon tubes as illustrated in Fig. 3.7. Figure 4.13 shows the effect of nitrogen flushing on the total background rate. The timespans during which the detec-

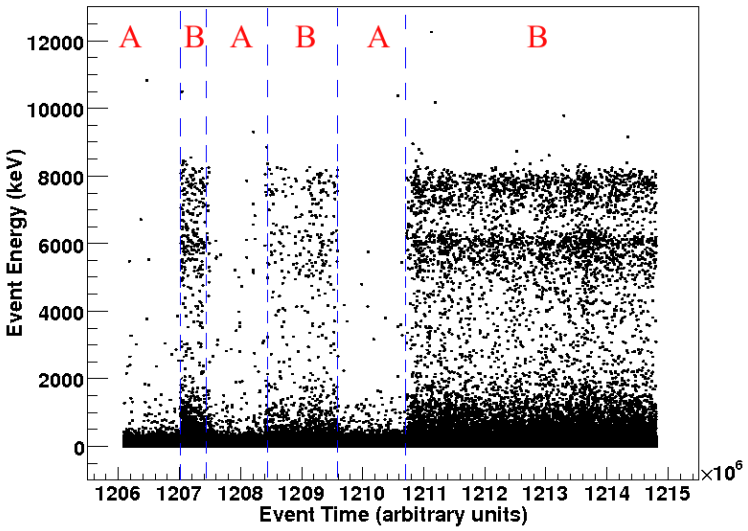

Figure 4.13: Energy of all detected events during measuring period of 2008. The reduction in background is clearly visible during the nitrogen flushed periods, labeled as A. The data taking periods without nitrogen flushing (labeled as B) show a significantly higher background rate.

tor setup was flushed with nitrogen show a significantly reduced background signal above the detector threshold of about 100 keV compared to the data taking periods without nitrogen flushing. Furthermore, the ^{214}Bi background as well as the number of ^{212}Bi- and ^{222}Rn- background signals are reduced dramatically by nitrogen flushing. This becomes especially evident in the ^{214}Bi produced background determined by timing-coincidence analysis of the complete dataset of 2008 containing runs with and without nitrogen flushing. The time occurrence of the α-particles emitted by ^{214}Po is shown in Fig. 4.14. By flushing the detectors with nitrogen while taking data, the ^{214}Bi background can be reduced by almost two orders of magnitude. Figure 4.15 shows a comparison of the number of ^{214}Bi events within the runs without nitrogen flushing vs. the number of ^{214}Bi events within the runs with nitrogen flushing. The dataset taken during the not nitrogen flushed datataking period contains 379 events within 35.92 kg $\cdot$ h of measuring time, indicating a ^{214}Bi background of 0.268 counts/h. The dataset of the runs during which the detectors were flushed with nitrogen consisted of 166.37 kg $\cdot$ h of measuring time and

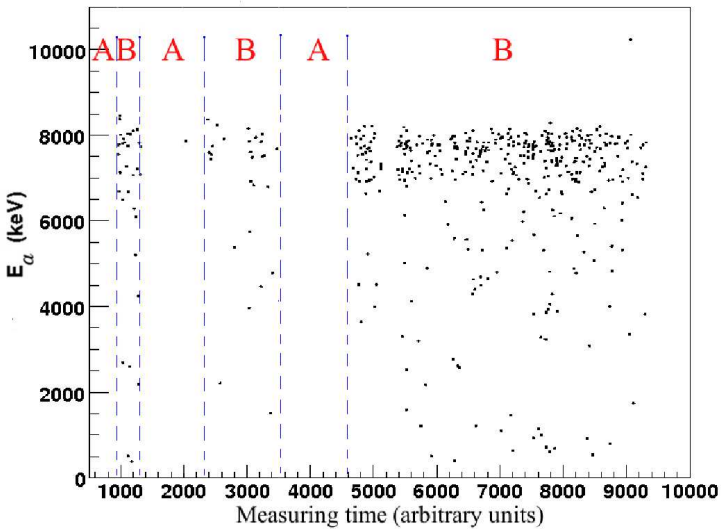

Figure 4.14: Energy of all detected α-events arising from the $^{214}\text{Bi} \xrightarrow{\beta} {}^{214}\text{Po}$ coincidence during measuring period of 2008. As before for the total background, the reduction in $^{214}\text{Bi} \xrightarrow{\beta} {}^{214}\text{Po}$-events is clearly visible during the nitrogen flushed periods, labeled as A. The data taking periods without nitrogen flushing (labeled as B) show a significantly higher $^{214}\text{Bi} \xrightarrow{\beta} {}^{214}\text{Po}$-background rate.

contains 7 events. This yields a ^{214}Bi background of 0.001 counts/h. Accordingly, the improvement in ^{214}Bi background that can be achieved by nitrogen flushing is a factor of about 270 .

4.2.3.1 Intrinsic Contamination of the Detectors

CdZnTe detectors can be fabricated very radiopure. Nevertheless, as the air and buildings are contaminated with isotopes contained in the natural decay chains, especially radon, some radioactive isotopes are encapsulated within the detectors during the fabrication process. Moreover, a contamination of the detector surfaces during transportation or passivation can not be excluded. This results in an intrinsic contamination of the detectors. The radioactive isotopes are contained within the detector material, therefore shielding or nitrogen flushing are not capable of avoiding this type of background. It will be demonstrated in this section that the intrinsic contamination can be reduced by timing-coincidence analysis. As the previous sections have shown, the analysis of the intrinsic contamination is only applicable in a system where the external background is as low as possible. Therefore, the runs with nitrogen flushing are investigated.
To determine the intrinsic contamination of the detectors, the cuts of the analysis have to be limited to a narrow range around the properties of the investigated

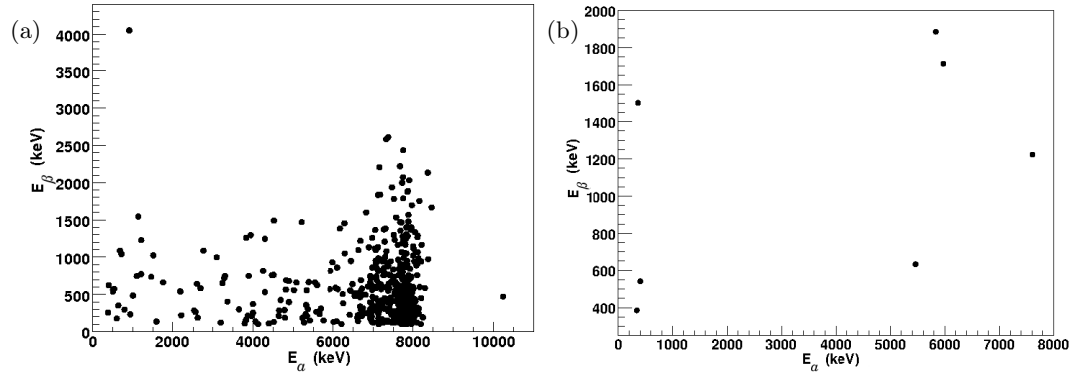

Figure 4.15: Effect that nitrogen flushing has on the ^{214}Bi background. a) The ^{214}Bi background of 35.92 kg·h of not nitrogen flushed data taking periods. 379 ^{214}Bi events can be identified, resulting in a total ^{214}Bi activity of 0.268 counts/h. b) The ^{214}Bi background of 166.37 kg·h of nitrogen flushed datataking periods. 7 events could be identified yielding a total ^{214}Bi activity of 0.001 counts/h.

decay in order to exclude external or random events. The limited energy resolution of the detectors constrains the cut range for the particle energies. The detector resolution increases linearly with increasing energy. For this analysis, a conservative detector resolution of 5% was assumed. The COBRA detectors have a resolution of 1.5-3 % [Col05] at 2.6 MeV. However, the energy resolution slightly degrades with increasing energy. Therefore, a worse energy resolution is assumed in order not to underestimate the effects the energy resolution causes. The timing cuts are those as in section 4.2.2: Accordingly, a timespan consisting of 3-5 half-lives of the investigated coincidence is chosen for the timing cut. Furthermore, the timecut must be above the dead time of the ADCs being 120 μs and it has to be large enough to exclude faster decays. The problem of faster decays does not affect the decay of ^{214}Bi because of its particularly low half-life, but it has an effect on timing-coincidences with larger half-lifes and must therefore be excluded.
In order to give a realistic estimate on the contamination of the detectors, it is necessary to consider that the cuts have a limited efficiency. This means that they only identify a certain fraction of all occurring events. This is due to detector efficiency, detector resolution and incomplete deposition of the particle energy inside the detector volume. The total cut efficiency represents the percentage of all occurring events of interest that meet the requirements of the cuts. The total efficiency is a product of the single cut efficiencies:

$$\epsilon_{\mathrm{total}} = \epsilon_{\Delta \mathrm{t}} \prod_{i,j} \epsilon_{\mathrm{i,j}} \epsilon_{\mathrm{mi}} \qquad i = \alpha,\ \beta \quad j = 1,\ 2 \tag{4.6}$$

where $\epsilon_{\mathrm{total}}$ is the total cut efficiency, ϵ_{mi} are the branching ratios of the decay i, such that $\epsilon_i \epsilon_{\mathrm{mi}}$ are the energy cut efficiencies and $\epsilon_{\Delta \mathrm{t}}$ is the efficiency of the

timing cut. The branching ratios ϵ_{mi} of the investigated decays are characteristic properties of the decaying isotopes and were taken from [NUC].
The energy cut efficiencies ϵ_i are determined by the help of the simulations introduced in section 4.2.1: The simulations are used to determine how many events of interest are identified by the energy cuts. The energy cut efficiency $\mathrm{N_{eff}}$ is defined as follows:

$$\mathrm{N_{eff}} = \frac{\mathrm{N_{ROI}}}{\mathrm{N_{total}}}, \tag{4.7}$$

with $\mathrm{N_{ROI}}$ being the number of events in the energy region of interest and $\mathrm{N_{total}}$ being the total number of events. In order to determine the timing-cut efficiency $\epsilon_{\Delta t}$ no simulations are required. The timing-cut efficiency is equal to the probability of observing an event during the selected timespan. Due to the fact that all the investigated isotopes have well-known half-lives that can be transformed into decay-constants, the timing-cut efficiencies can be calculated using Eq. 4.4. This yields an observation probability P_λ of the desired events depending on the observed timespan $\Delta\mathrm{t} = (t_2 - t_1)$:

$$\epsilon_{\Delta\mathrm{t}} := P_\lambda = \frac{\mathrm{N(t_1) - N(t_2)}}{\mathrm{N_0}} = \lambda \int_{t_1}^{t_2} e^{-\lambda t}\,\mathrm{d}t = e^{-\lambda t_2} - e^{-\lambda t_1}. \tag{4.8}$$

4.2.3.2 Intrinsic ^{214}Bi Contamination

The complete datasets of the $\mathrm{N_2}$-flushed datataking periods of 2008 and 2009 were searched for the decay sequence $^{214}\mathrm{Bi} \xrightarrow{\beta} {}^{214}\mathrm{Po} \xrightarrow{\alpha} {}^{210}\mathrm{Pb}$ in order to determine the intrinsic ^{214}Bi contamination of the detectors. The investigated datasets contained $166.37\,\mathrm{kg \cdot h}$. The cuts that were used for this analysis, along with the cut efficiencies, are listed in Table 4.4. The total cut efficiency ϵ_{total} turns out to be 0.4142.

Table 4.4: Cuts to determine the intrinsic contamination of the detectors with ^{214}Bi within the datasets of the $\mathrm{N_2}$ flushed datataking periods taken in 2008 and 2009, containing 166.37 kg·h of data.

Cut	Cut-Range	Cut Efficiency
$\epsilon_{\beta 1}$	$300\,\mathrm{keV} < \mathrm{E}_\beta$	73.29 %
$\epsilon_{\alpha 2}$	$7200\,\mathrm{keV} < \mathrm{E}_\alpha < 8200\,\mathrm{keV}$	99.50 %
$\epsilon_{\Delta\mathrm{t}}$	$120\,\mu\mathrm{s} < \Delta\mathrm{t} < 800\,\mu\mathrm{s}$	56.8 %
Total Cut Efficiency $\epsilon_{\mathrm{total}}$		41.42 %

Due to the dead time of the ADCs of $120\,\mu$s and the lower limit of 300 keV for the β cut, the remaining 58.58 % of the $^{214}\mathrm{Bi} \rightarrow {}^{214}\mathrm{Po}$ events are not included in the cuts and are therefore not seen.
Analyzing the entire dataset containing $166.37\,\mathrm{kg \cdot h}$ of data reveals two events that could be traced back to the decay sequence $^{214}\mathrm{Bi} \xrightarrow{\beta} {}^{214}\mathrm{Po} \xrightarrow{\alpha} {}^{210}\mathrm{Pb}$. The activity

A in Becquerel per kilogram is defined according to [Ree09]:

$$A = \frac{\mathrm{n}}{\epsilon_{\mathrm{total}} \cdot \mathrm{M_T}}, \tag{4.9}$$

where n is the number of observed events and $\mathrm{M_T}$ is the amount of analyzed data in kg·s. For ^{214}Bi, the intrinsic contamination turns out to be $(8.1^{+9.1}_{-5.1})\,\frac{\mu\mathrm{Bq}}{\mathrm{kg}}$ at 68 % CL. The intrinsic contamination of the CdZnTe detectors with ^{214}Bi has been investigated before by [Ree09]. He investigated the detectors while they were passivated with the red passivation paint that was found to be radioactively contaminated itself. The outcome of his investigation was an intrinsic contamination of the detectors with ^{214}Bi of $(7 \pm 14)\,\frac{\mu\mathrm{Bq}}{\mathrm{kg}}$, which is in reasonable agreement with this analysis yielding results in the same order of magnitude. In this thesis the error margins were calculated using Poisson statistics (see [FC98]) that yield asymmetric error margins. Poisson statistics apply to an analysis with a small number of events.

For a successful outcome of the COBRA experiment, it is especially important to determine the background contribution of the intrinsic contamination to the energy region of interest, which is 2700-3000 keV for ^{116}Cd. As explained in section 3.7, a maximum background of 0.001 counts / (keV · kg · year) in the energy region of interest is the goal to achieve for observation of $0\nu\beta\beta$ decays. In order to determine the background contribution of the ^{214}Bi contamination of the detectors in the energy region of interest, again simulations are required:

$$\mathrm{N_{exp,ROI}} = \frac{\mathrm{N_{sim,ROI}}}{\mathrm{N_{sim,total}}}. \tag{4.10}$$

$\mathrm{N_{exp,ROI}}$ is the fraction of expected events in the energy region of interest, $\mathrm{N_{sim,ROI}}$ is the number of simulated ^{214}Bi-events occurring in the region of interest and $\mathrm{N_{sim,total}}$ is the sum of all simulated ^{214}Bi events. The percentage of ^{214}Bi atoms that emit a β-particle within the energy region of interest turns out to be 0.2219 %. This implies a background signal of $(1.9^{+2.1}_{-1.1}) \cdot 10^{-4}\,\frac{\mathrm{counts}}{\mathrm{keV \cdot kg \cdot year}}$ in the region of interest. Obviously, this background is almost 1/5 of the maximum total background that can be tolerated in order to have a realistic chance to observe a possible $0\nu\beta\beta$-decay within a timespan of four years, as described in Sect. 3.7. Only 41.42 % of this background contribution can be eliminated by timing-coincidence analysis, leaving an unidentified background conribution of $(7.9^{+8.7}_{-4.6}) \cdot 10^{-5}\,\frac{\mathrm{counts}}{\mathrm{keV \cdot kg \cdot year}}$ arising from ^{214}Bi. Therefore, a further improvement in background reduction is not absolutely necessary in the case of ^{214}Bi if the sum of all other background contributions can be suppressed to a maximum of $9.68 \cdot 10^{-4}\,\frac{\mathrm{counts}}{\mathrm{keV \cdot kg \cdot year}}$.

4.2.3.3 Intrinsic ^{212}Bi Contamination

Analogously to ^{214}Bi, the datasets of 2008 and 2009 have been scanned for the decay sequence $^{212}\mathrm{Bi} \xrightarrow{\alpha} {}^{208}\mathrm{Tl} \xrightarrow{\beta} {}^{208}\mathrm{Pb}$ in order to determine the intrinsic ^{212}Bi

contamination of the detectors. Table 4.5 shows the corresponding cuts that were used to identify the decay sequence within the datasets and the cut efficiencies. Because ^{208}Tl has a half-life of 3.83 min, the upper limit of the timing cut only

Table 4.5: Cuts to determine the intrinsic contamination of the detectors with ^{212}Bi within the datasets taken during N_2 flushed datataking periods of 2008 and 2009, containing 166.37 kg·h of data.

Cut	Cut-Range	Cut Efficiency
ϵ_α^1	$5700\,\text{keV} < \text{E}_\alpha < 6400\,\text{keV}$	35.85 %
ϵ_β^2	$320\,\text{keV} < \text{E}_\beta < 2300\,\text{keV}$	73.32 %
$\epsilon_{\Delta\text{t}}$	$1\,\text{s} < \Delta\text{t} < 554\,\text{s}$	87 %
Total Cut Efficiency ϵ_{total}		22.87 %

includes three half-lives of the coincidence instead of five in order to reduce the occurrence of random events that mimic the ^{212}Bi decay sequence. The total efficiency of the cuts turns out to be 22.87 %. This is due to that the α-decay of ^{212}Bi has a branching ratio of 35.94% which reduces the α-cut efficiency drastically. The datasets of 2008 and 2009 revealed four events in total that fulfill the requirements of the cuts. Using Eq. 4.9, this yields a ^{212}Bi detector contamination of $(30.0^{+20.0}_{-12.1})\frac{\mu Bq}{kg}$ at 68 % CL.
Furthermore, the simulations of the decay ^{208}Tl$\rightarrow$ ^{208}Pb revealed that 0.97% of all decaying ^{208}Tl atoms produce a signal in the region of interest. Taking the branching ratio of the decay ^{212}Bi$\rightarrow$ ^{208}Tl of 35.85 % into account, this produces a background signal of $(11.1^{+7.4}_{-4.5} \cdot 10^{-3})\,\frac{\text{counts}}{\text{kg·keV·year}}$ in the region of interest. This number does not represent the actual ^{212}Bi contamination of the detectors, but should be understood as an upper limit instead. The large half-life of the coincidence ^{212}Bi$\rightarrow$ ^{208}Tl and the fact that a continuous β-spectrum is included make the investigation difficult, because these facts allow for random events to mimic the coincidence. However, this number is too large in order for the experiment to successfully measure the signal of the $0\nu\beta\beta$-decay of ^{116}Cd or ^{130}Te. The analysis of the ^{212}Bi coincidence could be verified by a histogram of the time difference between the two occurring events as it was done in section 4.2.2. However, the amount of events is much too small in order to correctly perform this fit. Accordingly, more statistics are needed to be able to draw reasonable conclusions. Furthermore, the properties of the other decay channel of ^{212}Bi, containing the decay sequence $^{212}\text{Bi}\xrightarrow{\beta}{}^{212}\text{Po}\xrightarrow{\alpha}{}^{208}\text{Pb}$, are much more suitable for timing-coincidence analysis and could give a much better estimate on the actual ^{212}Bi contamination of the detectors. This would provide an independent analysis to check the validity of timing-coincidence analysis in the case of ^{212}Bi. In order to detect this decay channel, ADCs with a collecting time as low as 0.1 μs are needed. The ADCs currently in use for the experimental setup are not capable of resolving that decay sequence because they have a collection time of 120 μs while ^{212}Po has a half-life of

only 0.3 μs. Because of the small statistics, it is not clear if the ^{212}Bi contamination actually poses a threat to the successful outcome of the experiment. In that case, investigating the β-decay channel of ^{212}Bi by providing readout electronics that can resolve a fast decay of the order of 0.3 μs might be a solution.
A further improvement in background reduction is desirable and could be achieved if detectors were used that are enriched in ^{116}Cd: A reduction of the ^{113}Cd content of the detectors would weaken the background signal of ^{113}Cd occurring in the energy region of 0-316 keV and therewith, a statistical occurrence of ^{113}Cd events within a timespan of 800 μs would become more unlikely. Therefore, the β-energy cut could be lowered to 100 keV if the ^{113}Cd content of the detectors was reduced. Moreover, the detectors could be produced more radiopure. Another approach to further reduce the background signal of the natural decay chains is the use of the pixelated detectors described in section 3.3.2 instead of the CPG detectors described in section 3.3.1. Pixelated detectors are capable of identifying the coincident events from the natural decay chains by their decay signature with an efficiency of almost 100 % [Col07].

4.2.3.4 Other Intrinsic Contamination Limits

Some other timing coincidences can be found within the natural decay chains that are suitable for timing-coincidence analysis as well: The decay-sequence $^{222}\mathrm{Rn}\xrightarrow{\alpha}$ $^{218}\mathrm{Po}\xrightarrow{\alpha}$ ^{214}Pb occurring in the ^{238}U decay chain is an $\alpha-\alpha$ coincidence with a branching ratio of almost 100 % and a half-life of 3.05 min. The ^{232}Th decay chain contains the decay sequence $^{220}\mathrm{Rn}\xrightarrow{\alpha}$ $^{216}\mathrm{Po}\xrightarrow{\alpha}$ ^{212}Pb with a branching ratio of 100 % and a half-life of only 0.145 s. Within the ^{235}U decay chain, the decay sequence $^{223}\mathrm{Ra}\xrightarrow{\alpha}$ $^{219}\mathrm{Rn}\xrightarrow{\alpha}$ ^{215}Po has a branching ratio of 100 % and a half-life of 3.96 s. All these decay sequences are $\alpha-\alpha$-coincidences that hardly contribute to the energy-region of interest. Nevertheless, knowing the detector contamination limits with these isotopes improves the understanding of the full background spectrum which will now briefly be discussed. Unfortunately, no simulations for these decays exist so far, resulting in an incomplete knowledge of the energy cut efficiencies. However, since all decays are α-decays, the energy cut efficiency can be assumed to be 100 % without namable errors. The energy cuts were chosen to be 1000 keV around the α-energies. For the timing cuts, a maximum of five half-lives of the investigated coincidence was chosen, yielding a timing cut efficiency of almost 100 %. One event indicating a ^{222}Rn contamination could be identified. This yields a ^{222}Rn detector contamination of $(1.7^{+2.9}_{-1.1})\ \frac{\mu\mathrm{Bq}}{\mathrm{kg}}$ at 68 % CL. The same number serves as an upper limit on the intrinsic ^{220}Rn- and ^{223}Ra-contamination, where no events were found within the whole dataset.

4.2.4 Background Reduction Summary

In the previous two sections it was shown that timing-coincidence analysis is a powerful method for background reduction and the total background rate of certain decay sequences from the natural decay chains have been determined. Furthermore, timing-coincidence analysis demonstrates the necessity for nitrogen flushing by showing the improvement in the naturally occurring background rate, reducing the background by two orders of magnitude. Investigations on datasets of detectors not flushed with nitrogen confirmed the correctness of timing-coincidence analysis by confirming the half-lives of the observed decays. Furthermore, timing-coincidence analysis is the only background reduction method capable of providing an estimate on the intrinsic contamination of the detectors with isotopes from the natural decay chains. Table 4.6 shows the achieved estimates of the detector contamination with different isotopes. The contamination limits have been determined with the help of simulations of the investigated decays. Using these

Table 4.6: Intrinsic contamination limits determined with timing-coincidence analysis. A dataset containing 166.37 kg h of data taken with nitrogen flushed detectors was investigated.

Coincidence	Intrinsic Contamination
$^{223}\mathrm{Ra} \xrightarrow{\alpha} {}^{219}\mathrm{Rn} \xrightarrow{\alpha} {}^{215}\mathrm{Po}$	$<(1.7^{+2.9}_{-1.1})\ \frac{\mu\mathrm{Bq}}{\mathrm{kg}}$
$^{220}\mathrm{Rn} \xrightarrow{\alpha} {}^{216}\mathrm{Po} \xrightarrow{\alpha} {}^{212}\mathrm{Pb}$	$<(1.7^{+2.9}_{-1.1})\ \frac{\mu\mathrm{Bq}}{\mathrm{kg}}$
$^{212}\mathrm{Bi} \xrightarrow{\alpha} {}^{208}\mathrm{Tl} \xrightarrow{\beta} {}^{208}\mathrm{Pb}$	$<(30.0^{+20.0}_{-12.1})\ \frac{\mu\mathrm{Bq}}{\mathrm{kg}}$
$^{222}\mathrm{Rn} \xrightarrow{\alpha} {}^{218}\mathrm{Po} \xrightarrow{\alpha} {}^{214}\mathrm{Pb}$	$(1.7^{+2.9}_{-1.1})\ \frac{\mu\mathrm{Bq}}{\mathrm{kg}}$
$^{214}\mathrm{Bi} \xrightarrow{\beta} {}^{214}\mathrm{Po} \xrightarrow{\alpha} {}^{210}\mathrm{Pb}$	$(8.1^{+9.1}_{-5.1})\ \frac{\mu\mathrm{Bq}}{\mathrm{kg}}$

simulations, the background signal of the ^{214}Bi- and the ^{212}Bi-contamination in the energy region of interest was estimated to be $(1.9^{+2.1}_{-1.1})\cdot 10^{-4}\ \frac{\mathrm{counts}}{\mathrm{keV\cdot kg\cdot year}}$ for ^{214}Bi and $(11.1^{+7.4}_{-4.5})\cdot 10^{-3}\ \frac{\mathrm{counts}}{\mathrm{keV\cdot kg\cdot year}}$ for ^{212}Bi. To conclude, the outcome of the analysis of the dataset is that at this moment, the intrinsic contamination limit for ^{212}Bi is too high in order for the $0\nu\beta\beta$-experiment to succeed. Therefore, further background reduction and an improvement of timing coincidence are necessary.
The major drawback of timing-coincidence analysis is its efficiency: The most suitable timing coincidence, which is the decay sequence ^{214}Bi$\rightarrow{}^{214}$Po$\rightarrow{}^{210}$Pb, is identified with a rather low efficiency of 41.42 %. A reduction of the intrinsic background could be achieved in two different ways: Either the detectors are fabricated with an intrinsic ^{212}Bi contamination that is improved by at least an order of magnitude, or the efficiency of timing-coincidence analysis is enhanced to that extent that 90-95 % of the naturally occurring events can be identified. A significant improvement can be achieved by the use of ADCs with much shorter collecting time: The ADCs currently in use have a collecting time of 120 μs, which limits the efficiency of the timing cut, especially for the decay sequence ^{214}Bi$\rightarrow{}^{214}$Po$\rightarrow{}^{210}$Pb.

However, some decay sequences, such as ^{212}Bi$\rightarrow^{208}$Tl$\rightarrow^{208}$Pb are difficult to investigate due to their large half-life. The contamination limit of these decays might therefore be overestimated. The use of faster ADCs would significantly improve this limit by enabling the investigation of the other decay channel of ^{212}Bi which is ^{212}Bi$\rightarrow^{212}$Po$\rightarrow^{208}$Pb with a half-life of 0.3 μs. Therewith, the probability for random events during the timespan of the timing-cut would be reduced to almost zero, allowing an exact determination of the ^{212}Bi contamination. In addition, reducing the ^{113}Cd content of the detectors would improve the contamination limits of decay sequences where β-decays are involved by reducing the number of random events in the low-energy region due to the ^{113}Cd shoulder.
Another possibility of improving the background arising from the natural decay chains is the use of pixelated detectors as described in section 3.3.2 instead of CPG detectors, which are explained in section 3.3.1. Pixelated detectors can identify timing-coincidences by their decay signature with an efficiency of almost 100 % (see section 3.4.3).

4.3 Specific Background Signatures: The Decay of ^{113}Cd

As illustrated in the analysis in the first part of this chapter, the high-energy part of the spectrum is strongly dominated by external events. In contrast, the low-energy part of the spectrum mostly contains events arising from the decay ^{113}Cd$\xrightarrow{\beta}$ ^{113}In. ^{113}Cd is encapsulated within the cadmium of the detectors with a natural abundance of 12.22 % [NUC]. The decay ^{113}Cd$\xrightarrow{\beta}$ ^{113}In is classified as four-fold forbidden, non-unique β decay [MAS06]. Hence, it is a very rare process that has an experimentally determined half-life of $7.7{\cdot}10^{15}$ years [KAE] $- 8.2{\cdot}10^{15} \pm 0.2(\text{stat})^{+0.2}_{-1.0}(\text{sys})$ years as determined by the COBRA experiment [GJK$^+$05].
Various authors have tried to theoretically characterize the spectral shape of this rare process, such as [ABC$^+$94] and [DGK$^+$96]. Several theoretical models were experimentally found not to describe the behavior of the ^{113}Cd$\rightarrow$ ^{113}In decay [B$^+$07a]. In 2005, [GJK$^+$05] experimentally proved that the spectral shape proposed on the Table of Isotopes Web Page [TOI] does not reproduce the actual data. They investigated 0.86 kg·d of data taken by four red passivated 1 cm^3 coplanar grid detectors. They also compared the theoretical curves proposed by [DGK$^+$96] and [ABC$^+$94] to the measured spectrum, but none of them showed reasonably good agreement.

4.3.1 A Theoretical Description of the ^{113}Cd-Spectrum

In 2006, [MAS06] for the first time introduced a theoretical model derived from the microscopic quasiparticle-phonon model that was supposed to describe the spectral shape of the ^{113}Cd$\xrightarrow{\beta}$ ^{113}In decay more accurately (as discussed in section 2.2.3.1 The spectral shape of this model is shown in Fig. 4.16. The intensity has been

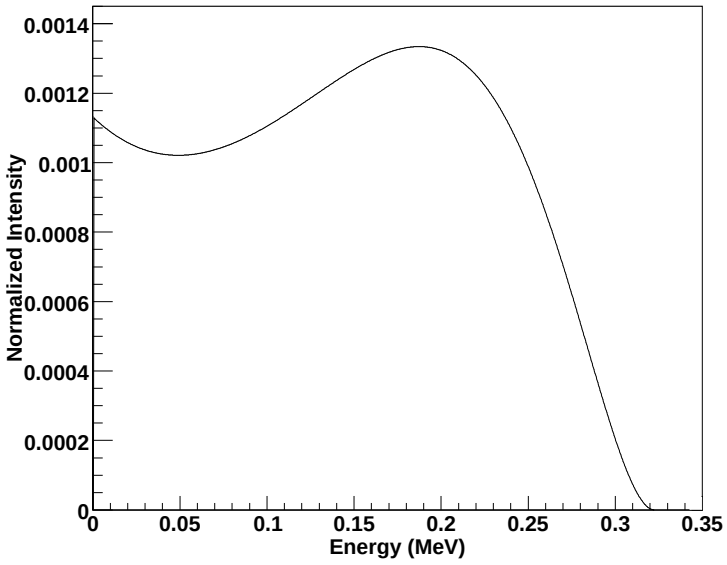

Figure 4.16: Theoretical spectral shape of the decay $^{113}\mathrm{Cd}\xrightarrow{\beta}{}^{113}\mathrm{In}$ according to [MAS06]. The intensity has been normalized to the area underneath the curve.

normalized by the total area underneath the curve.
In order to compare the theoretical model to the data, the model has to be adjusted to the detector properties: The detector efficiency and the detector resolution influence the spectrum. The finite energy resolution of the detector deforms the spectrum. Particles do not produce a signal at the energy that they actually deposit within the detector volume, but cause a signal within a range around this particle energy. The energy resolution of a detector is a non-local function of the energy that influences the signal. This effect can be taken into account in the theoretical spectrum by performing a convolution of the energy resolution of the detector with the theoretical model. The energy resolution of a detector worsens as the energy approaches zero. Accordingly, convolving the detector resolution with the theoretical spectral shape shifts the original spectrum towards decreasing intensities at low energy.
As the detector efficiency is limited, some particles pass through the detectors without causing a signal. In order to account for the impact of the detector efficiency on the theoretical model, the model has to be multiplied with the detector efficiency [Koe] that is determined with the help of simulations. The spectra have been taken with four colorless passivated detectors with different detector efficiencies. Figure 4.17 shows the theoretical model adjusted to the properties of the four detectors individually. As expected, the theoretical spectrum is slightly shifted towards lower energies and vanishes when the energy approaches zero. The effect of the detector resolution is much stronger than that of the detector efficiency,

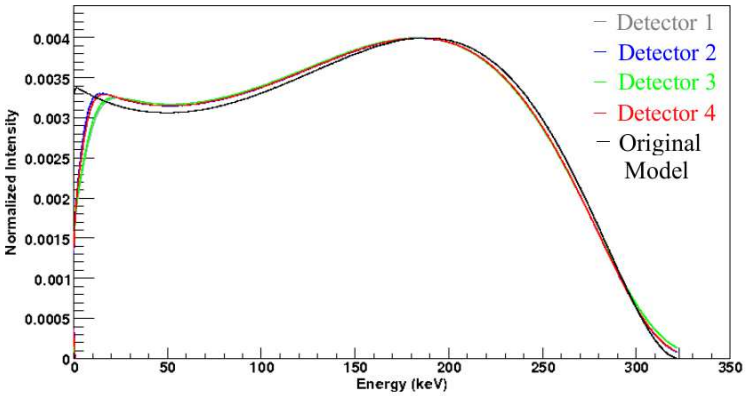

Figure 4.17: Theoretical spectral shape of the decay $^{113}\mathrm{Cd}\xrightarrow{\beta}{}^{113}\mathrm{In}$ according to [MAS06], convolved with the detector resolutions of the four detectors, multiplied with their efficiencies. The intensity has been normalized to the area underneath the curve. The effect that the difference in energy resolution and efficiency of the different detectors has on the change in the spectral shape becomes only important in the energy region below 40 keV.

which is hardly visible at all. The adjusted spectra only show significant differences in the energy region below 40 keV. The detector threshold is 100 keV in most of the measurements, but it is above 40 keV in every dataset. Accordingly, for a comparison of the model with the dataset, an average detector resolution and efficiency can be used without any significant loss of information.

4.3.2 Comparison of the Model with the Data

A comparison of the theoretical spectrum with the dataset of the nitrogen flushed run of 2009 containing 89.04·kg h of data is performed using the χ^2-test (see Appendix C) After being adjusted to the detector properties, the only variable of the spectrum is its normalization. The shape and the horizontal position are fixed. The χ^2-test allows drawing a conclusion on how well the dataset is described by the model. Moreover, it yields the optimum vertical position of the theoretically determined curve relative to the experimentally measured spectrum (for more informations on the determination of the best χ^2-value, see Appendix D).
Before the measured spectrum can be compared to the data, the obvious background to the spectrum has to be subtracted. This background shows exponential behavior. To determine the shape of this background to the ^{113}Cd spectrum, an exponential fit of the form $N(E)=\exp(p_0+p_1\cdot E)$ is performed for the region above 320 keV in order to exclude events arising from ^{113}Cd. This fit is shown in Fig. 4.18 together with the total spectrum below 1600 keV measured with nitrogen flushed detectors during 2009. The following parameters were determined by the

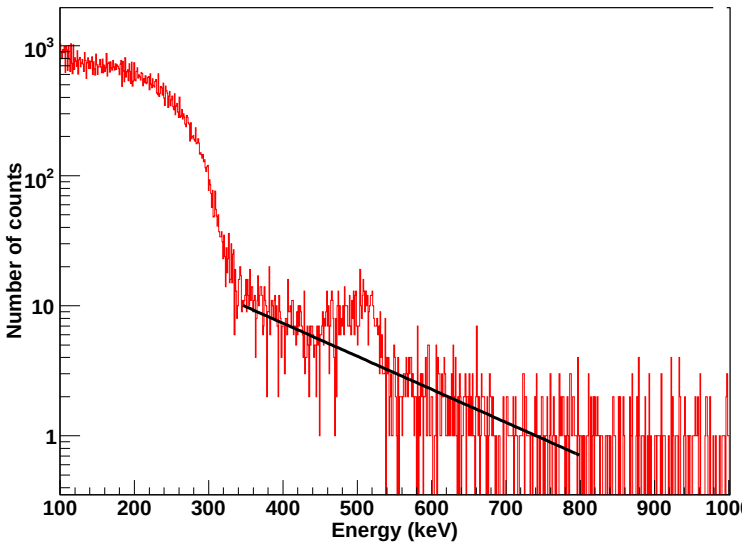

Figure 4.18: Total energy spectrum of the runs with nitrogen flushing performed during 2009, containing 166.37 kg h of data. An exponential fit has been performed in the energy region above 320 keV in order to determine the shape of the background signal.

fit: p_0=-5.85097·10^{-3}, p_1=4.33392. For the following discussions, this background was extrapolated to the ^{113}Cd signal region and subtracted from the spectrum. Figure 4.19 shows the theoretical model normalized with the best χ^2-value together with the dataset. The binning of the histogram had to be adjusted to the number of datapoints available from the theoretical model being $\frac{333}{316}$ bins/keV. As the investigated energy range did not include the region below 100 keV, the binning of the histogram was chosen to be $\frac{227}{216}$ bins/keV in order to be comparable to the available binning of the theoretical model. Obviously, the theoretical model does not reproduce the spectral shape that was measured by the detectors. A quantitative value that represents the quality of the model is χ^2_{norm}, defined as follows:

$$\chi^2_{\mathrm{norm}} = \frac{\chi^2}{\mathrm{n_f} - \nu - 1}, \tag{4.11}$$

where $\mathrm{n_f}$ is the number of degrees of freedom, which is in this case the number of bins in the histogram, and ν is the the number of adjustable parameters. In this case, ν is 1, because the only adjustable parameter of the theoretical model is its vertical position. This analysis yielded a χ^2_{norm} of 31 with a $\mathrm{n_f}$ of 227 and a χ^2 of 7000. According to [PSY], a χ^2 of 255.26 at 200 degrees of freedom yields a probability of 99.95% for the model not to describe the data. Therefore, a χ^2 of 7000 for 227 degrees of freedom practically excludes an agreement between the theoretical model and the measured spectrum. Two opposing assumptions can be made based on this finding: Either the model does not describe the behavior of

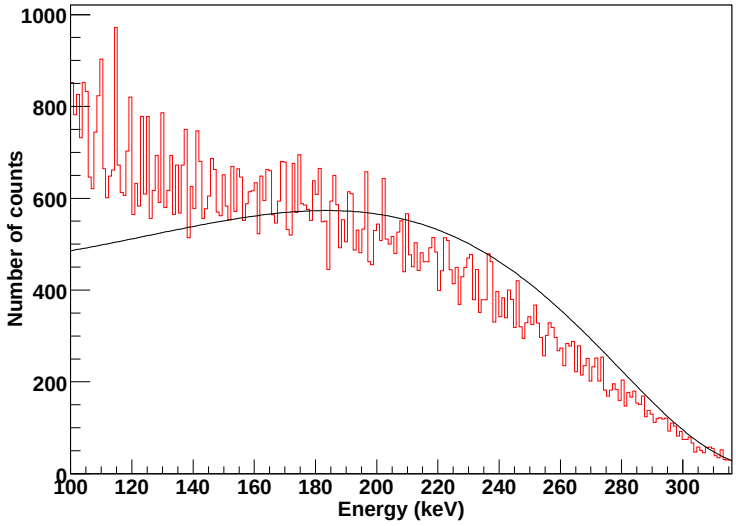

Figure 4.19: Comparison of theoretical spectral shape of the decay $^{113}\text{Cd} \xrightarrow{\beta} {}^{113}\text{In}$ according to [MAS06], convolved with the average detector resolutions of the four detectors, multiplied with the average efficiency and normalized with the best χ^2. It is obvious that the theoretical model does not reproduce the spectral shape that was measured by the detectors. The measured spectrum contains 166.37 kg h of data.

the decay correctly, or the spectrum of ^{113}Cd is superimposed by an unidentified background. Both assumptions allow different conclusions and will be discussed in the following sections.

4.3.2.1 Comparison by χ^2-test

In order to exclude the possibility that the difference between the theoretical model of the ^{113}Cd spectrum and the measured spectrum is caused by a malfunction of one of the detectors, the analysis is repeated for the four detectors separately. Figure 4.20 shows the spectra and the best χ^2-fits for the four detectors individually. The χ^2-values for the four spectra compared with the theoretical model normalized with the best χ^2-value are: χ^2(detector 1)=4281; χ^2(detector 2)=787; χ^2(detector 3)=1074; χ^2(detector 4)=1418. Obviously, detector 1 shows a significantly stronger difference between the measured spectrum and the model. In particular, the event rate in the energy region below 140 keV is significantly higher in the spectrum of detector 1 compared to the other detectors: This indicates that detector 1 might be located close to an additional background source that produces a low-energetic signal. Another reason for the different spectral shape measured by detector 1 could be a different ^{113}Cd content compared to the other detectors.

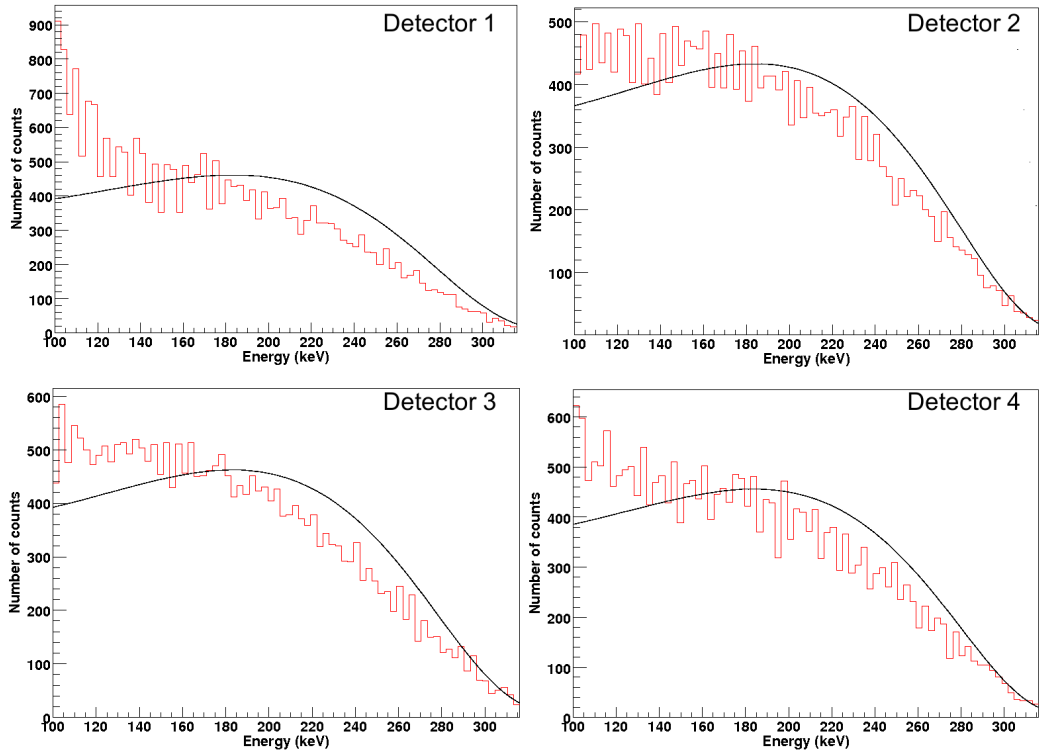

Figure 4.20: ^{113}Cd spectra taken by four colorless passivated detectors during measuring period of 2009 along with the theoretical model developed by [MAS06] at best χ^2. The best χ^2-values are: χ^2(detector 1)=4281; χ^2(detector 2)=787; χ^2(detector 3)=1074; χ^2(detector 4)=1418.

Nevertheless, all the χ^2-values are very large and therefore prove that the model does not describe the measured spectrum accurately. In addition, the four spectra differ from the theoretical description in the same manner: The theoretical model overestimates the measured spectrum at energies above 140-160 keV but below 140 keV every spectrum shows a larger intensity than the model. Assuming the correctness of the model, this allows to draw the following conclusion: In the energy region above 160 keV, the total measured spectrum is actually dominated by events from the decay $^{113}\mathrm{Cd}\xrightarrow{\beta}{}^{113}\mathrm{In}$, where it is well described by the theoretical model from [MAS06], but in the energy region below 160 keV, the measured spectrum appears to be a superposition of events from the decay of ^{113}Cd and an additional unknown background contribution, so that the normalization of the theoretical curve is overestimated by the χ^2-test. Answering the question whether the theoretical spectral shape agrees with the measured spectrum at energies below 160 keV will be possible as soon as this additional background component is fully identified and can therefore be subtracted from the total measured spectrum to reveal the absolute ^{113}Cd spectrum. This requires to employ additional physical

informations and will be further investigated in the next section.
The analysis of the ^{113}Cd spectrum has been performed before by [Ree09] in

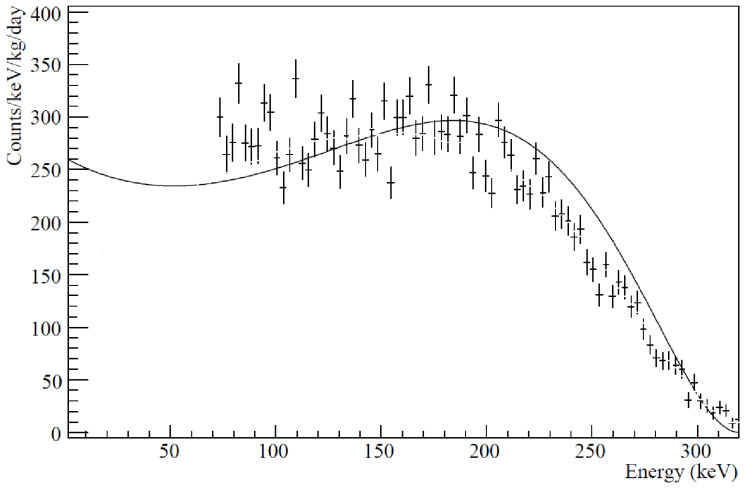

Figure 4.21: ^{113}Cd spectrum taken by one red passivated detector, with theoretical model (solid line) of four-fold forbidden, non-unique β-decay from [Ree09].

2009, with 12 red passivated detectors. He compared those spectra to the model from [MS07]. The outcome of his analysis is shown in Figure 4.21. In contrast to this analysis, the theoretical model (solid line) was not convolved with the detector resolution or multiplied by the detector efficiency, nor did he systematically adjust the model to the spectrum. Nevertheless, the tendency is visible. He concluded that the theoretical model does not agree with the measured spectrum. This effect becomes especially evident in the energy region below 140 keV, where the theoretical model predicts smaller intensities than those obtained by the measurement. Furthermore, the event rate from ^{113}Cd is overestimated in the region above 180 keV. This is a result of the χ^2-method, which does not adjust the model to regions where it agrees with the curve progression but minimizes the total error instead. As a conclusion, [Zub] assumed that the difference between the data and the model is due to the red passivation paint, which was proved to be radioactively contaminated [Col06]. The outcome of the analysis of the dataset taken with colorless passivated detectors is in perfect agreement with the results of [Ree09]. Therefore, the analysis of the colorless passivated detectors refutes the assumption of an additional background contribution arising from the red passivation paint being responsible for the difference between the data and the model. The values obtained in the energy region below 140 keV are significantly larger in the measured spectrum than in the predictions of the model.

4.3.2.2 Comparison by Expected Event Rate

Instead of determining the best position for the theoretically predicted curve by a χ^2-test, it is also possible to approximate the absolute height of the theoretical spectrum by a different method: The knowledge of the half-life of the ^{113}Cd decay, being (7.7-8.2)·10^{15} years, and the ^{113}Cd content in the detectors, which is 12.22 % of the cadmium within the detectors and therefore 4.77-5.25 % of the total detector material (more precisely, 4.77-5.25 % of the total number of particles defining the total detector mass) allows an approximation of the expected number of ^{113}Cd-decays within the measuring time of 3432 hours performed with 25.837 g of detector material. In this section, the theoretical curve is renormalized with the expected number of ^{113}Cd-decays. This determines the expected position of the theoretical curve within the spectrum. The renormalized theoretical ^{113}Cd-spectrum is shown in Fig. 4.22, together with the measured sum-spectrum of all four detectors yielding a total of 89.04 kg·h of data. For this renormalization of the theoretical curve, an average half-life of the latest two results of $8 \cdot 10^{15}$ years is used.
Above 160 keV, the measured spectrum agrees with the renormalized theoretical

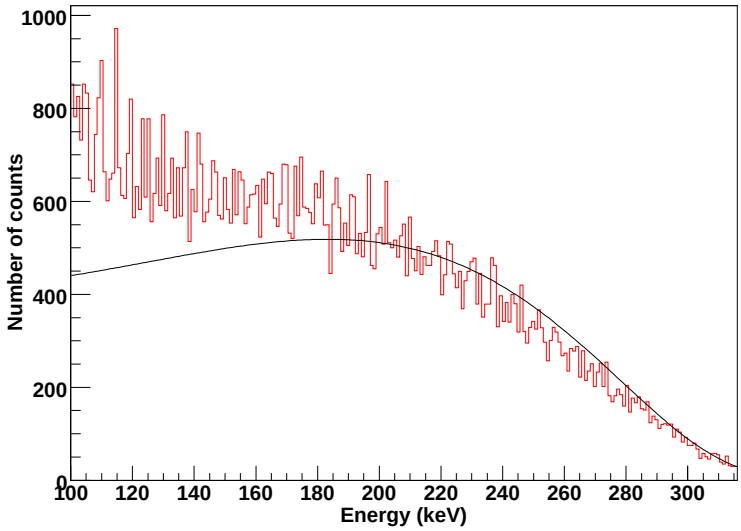

Figure 4.22: ^{113}Cd spectrum taken by four colorless passivated detectors during measuring period of 2009, with theoretical model (solid line) of four-fold forbidden, non-unique β-decay normalized with the expected number of decays from ^{113}Cd within that measuring time.

description. As the choice for the normalization of the theoretical curve has been made completely independent of the measured spectrum, and only the specifics of the measurement, such as the ^{113}Cd-content of the detectors, the total detector

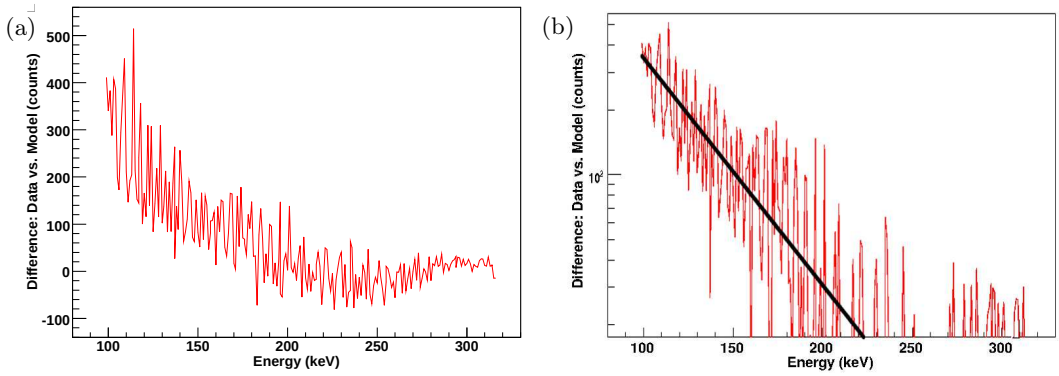

Figure 4.23: Background signal to the spectrum of ^{113}Cd. An exponential decrease in intensity can be seen between 100 keV and 220 keV. Furthermore, a small peak is slightly visible at 172 keV. (a) shows a linear plot of the background signal. In (b) the background signal is illustrated half-logarithmically, with an exponential fit indicating that the background to the ^{113}Cd spectrum actually shows an exponential behavior and becomes relevant at energies below 220 keV. The peak at 172 keV is more evident in this illustration.

mass and the measuring time, were considered in the normalization of the model, the agreement is quite remarkable. Below the energy of 180 keV, the measured spectrum constantly shows a larger number of events than expected from the model.

The χ^2-method in combination with the expected event rate method yield a quantitative deviation that allows the assumption that the theoretical model describes the spectral shape of ^{113}Cd accurately and the derivation of the measured spectrum from the theoretical description arises from a yet unidentified background in the low-energy region. The benefit of the expected event rate method is that the residual background-spectrum can easily be determined by subtracting the correctly normalized theoretical curve from the measured spectrum. The result is shown in Fig. 4.23. An exponential decrease of the signal can be observed between 100 keV and 220 keV. No peaks can be observed within the energy region below 160 keV. The most probable source of this background component is electronic noise. Electronic noise can arise from the entire readout system, but the most probable source are the unshielded capton cables used for signal readout and the detector contacts [Zub]. This needs to be confirmed by further investigations. A possible source of the electronic noise must be found and eliminated to measure the absolute ^{113}Cd spectrum. Figure 4.23b shows the differential ^{113}Cd background signal with half-logarithmic scale. An exponential fit has been performed for the low-energetic part. The exponential fit is in perfect agreement with the differential spectrum, verifying the exponential decrease with increasing energy of the yet unidentified background to the ^{113}Cd spectrum. In

addition to the exponentially decreasing part of the background signal, a small peak is suggestively visible at 172 keV, indicating an additional background source superimposed to electronic noise. This peak is more evident in the logarithmic illustration. None of the isotopes occurring within the natural decay chains produce γ-lines in this energy region. Furthermore, the detector materials do not contain any isotopes that could be responsible for this peak. There is one Cd-isotope, ^{124}Cd, which produces a γ-peak at 180 keV [KAE], but this isotope is not naturally contained within cadmium but has to be synthetically fabricated. Therefore, it is not clear whether the bump at 172 keV really arises from an unknown background source or if it is a statistical fluctuation that vanishes when a larger dataset providing more statistics is investigated. Above 220 keV, the differential signal between the measured spectrum and the model reduces to statistical fluctuations around zero. Above 220 keV, the measured spectrum is therefore in accordance with the model prediction.

4.3.3 ^{113}Cd Summary

It is found that the theoretical model for the spectrum of ^{113}Cd proposed by [MAS06] does not reproduce the total measured spectrum below 320 keV for one of the following two reasons: Either the theoretical model does not accurately describe the decay of ^{113}Cd, or the measured spectrum is a superposition of the ^{113}Cd spectrum and a yet unidentified background in the energy region below 220 keV. The available amount of data does not allow to draw a definite decision between those two assumptions, but the results of this analysis favor the assumption that the decay of ^{113}Cd is accurately described by the theoretical model, but that the measured spectrum contains an additional background that is yet to be identified. A measurement containing more statistics could help to identify this additional background by reducing statistical fluctuations. This could be provided by a longer measurement with more detector material. Further improvement would be achieved by a slight cooling of the detectors because this would improve the energy resolution of the detectors, reduce the electronic noise contribution and allow measurements with a threshold as low as 10 keV [Zub]
In order to exclude different potential background sources, an additional independent investigation of the spectrum must be performed with detectors enriched in ^{113}Cd. Accordingly, a measurement with detectors enriched in ^{113}Cd could answer the question whether the difference between the theoretical curve and the measured spectrum at energies below 220 keV arises from an additional background or from an incorrect theoretical description of the decay by determining the change in the relative difference between model and measurement with increasing ^{113}Cd content of the detectors. Moreover, the background arising from electronic noise should be investigated by a measurement with the colorless passivated detectors

without high-voltage.

Chapter 5

Conclusion and Outlook

In this thesis, the background of the COBRA experiment has been investigated, with special focus on background-reduction techniques. The method of timing-coincidence analysis has been introduced and proved to be an effective method for background reduction due to the identification of events arising from special isotopes of the natural decay chains. By timing-coincidence analysis, the necessity for a constant nitrogen flushing system in the COBRA experiment has been demonstrated by determining an improvement in ^{214}Bi-background by a factor of about 270 compared to the runs without nitrogen flushing. The correctness of the timing-coincidence method could be confirmed by successfully verifying the half-lifes of the investigated decay-sequences. In combination with a constant nitrogen flushing system, timing-coincidence analysis is capable of providing estimates of the intrinsic contamination of the detectors with certain isotopes from the natural decay chains. The decay sequence $^{214}\mathrm{Bi} \xrightarrow{\beta} {}^{214}\mathrm{Po} \xrightarrow{\alpha} {}^{210}\mathrm{Pb}$, causing most of the intrinsic contamination with over 70 % of the total number of events arising from the ^{238}U chain in the region of interest, turned out to be $(8.1^{+9.1}_{-5.1})\,\mu$Bq/kg. By consulting simulations, this value could be translated and corresponds to a signal of $(1.9^{+2.1}_{-1.1}) \cdot 10^{-4}$ counts/kg·keV·year in the region of interest. Furthermore, an upper limit for the ^{212}Bi-contamination of the detectors has been estimated to be $(30^{+20}_{-12.1})\,\mu$Bq/kg, yielding an upper limit of $(11.1^{+7.4}_{-4.5}) \cdot 10^{-3}$ counts/kg·keV·year in the energy region of interest. Moreover, upper limits for a detector contamination with ^{222}Rn, ^{220}Rn and ^{223}Ra were determined and turned out to be $(1.7^{+2.9}_{-1.1})\,\mu$Bq/kg for all three isotopes. The intrinsic contamination limit of ^{212}Bi turns out to be more than one order of magnitude too high for the $0\nu\beta\beta$-decays of ^{116}Cd and ^{130}Te to be observed. The major drawback of timing-coincidence analysis is its present limited efficiency: The timing cuts are restricted to be above 120 μs, which is the time resolution of the ADCs that are used. Accordingly, the efficiency of the ^{214}Bi-identification is reduced down to 41.42 %. Moreover, the decay sequence $^{212}\mathrm{Bi} \xrightarrow{\alpha} {}^{208}\mathrm{Tl} \xrightarrow{\beta} {}^{208}\mathrm{Pb}$ has a half-life as large as 183 s, causing random events to occur during the observation period. Therefore, the ^{212}Bi-contamination

limit might be completely overestimated due to random events. An investigation of the decay channel $^{212}\mathrm{Bi} \xrightarrow{\beta} {}^{212}\mathrm{Po} \xrightarrow{\alpha} {}^{208}\mathrm{Pb}$ by timing-coincidence analysis is not possible with the currently used ADCs due to the small half-life of ^{212}Po, being $0.3\,\mu$s. An investigation of this decay channel by timing-coincidence analysis could give a better estimate on the ^{212}Bi contamination limit. In order to improve the efficiency of timing-coincidence analysis, ADCs with a time resolution of less than $0.1\,\mu$s are required. Further improvement on the efficiency can be achieved by the use of detectors enriched in ^{116}Cd. The ^{113}Cd content is a limiting factor of the energy cuts, especially regarding the $^{212}\mathrm{Bi} \xrightarrow{\alpha} {}^{208}\mathrm{Tl} \xrightarrow{\beta} {}^{208}\mathrm{Pb}$ coincidence. Reducing the ^{113}Cd content would allow a widening of the energy cuts down to 100 keV. Together with the faster ADCs, this would enhance the coincidence identification efficiency to almost 100 %, allowing a better estimate of the ^{212}Bi contamination and thus eliminating almost the complete ^{214}Bi background contribution.
Besides an improvement of the current set-up, two more possibilities to reduce the background arising from the natural decay chains are the following: A fabrication of detectors with an intrinsic ^{212}Bi contamination of least a factor 10 less would reduce the intrinsic contamination level down to an acceptable limit. The other possibility is the use of pixelated detectors that are capable of identifying timing-coincidences by a tracking of their decay signature with an efficiency of almost 100 %.
The low-energy part of the spectrum allows the investigation of the four-fold forbidden, non-unique β-decay of ^{113}Cd. The spectrum measured by four colorless passivated detectors has been compared to the theoretical model developed by [MAS06] using two different methods: A first comparison was performed by a χ^2-test. The results indicate that the total measured spectrum below 320 keV was not accurately described by the model. As the χ^2-test is not capable of including specific properties of the ^{113}Cd-decay, including its content within the detectors, the total detector mass and the half-life of ^{113}Cd, an alternative method has been developed to adjust the position of the theoretical model to the measured spectrum by normalization of the theoretical spectrum with the expected ^{113}Cd event rate. A comparison of the theoretical model with the measured spectral shape by the method of expected event rate showed good agreement of the two spectra in the energy region above 220 keV and a systematic larger event rate of the measured spectrum in the energy region below 220 keV. The differential signal between measured spectrum and theoretical prediction shows an exponential decrease with increasing energy. The origin of this additional background could either be electronic noise or another, yet unknown superimposed background. Therewith, the necessity for investigating the background contribution of the electronic components of the COBRA experiment is at hand. At this point of the discussion, no definite conclusions can be drawn to determine whether the spectral shape of ^{113}Cd is accurately described by the theoretical model or not due to the small amount of available statistics. This question could be answered by additional measurements with detectors enriched in ^{113}Cd.

If the measured spectrum is actually a superposition of ^{113}Cd and an additional background component, the effect of the additional background component on the measured spectral shape would decrease with increasing ^{113}Cd content of the detectors and could therewith be identified if the background is kept constant. A measurement that provides more statistics would illustrate the spectral shape of the additional background component more clearly and therewith possibly enable its identification.
In summary, the analysis of the background spectrum using timing-coincidence analysis and the investigation of the decay sequence $^{113}\mathrm{Cd} \xrightarrow{\beta} {}^{113}\mathrm{In}$ independently showed the necessity for measurements providing more statistics. Both investigations need to be enhanced by the use of different readout electronics, providing a better time resolution and producing less electronic noise. In addition to the measurements performed with the COBRA detectors, measurements with two different types of detectors, one type enriched in ^{116}Cd and one type enriched in ^{113}Cd, would further improve both analysis.

Appendix A

Statistical Distributions

Discrete Distributions

The Binomial Distribution

The binomial distribution is used to describe the probability $\mathrm{P}(r)$ for an event to occur exactly r out of n times, when the single probability for the event to occur is p. It is given by [BL98]

$$\mathrm{P}(r) = C_n^r \cdot p^r (1-p)^{n-r} \quad r = 0, 1, 2, ..., n \ , \tag{A.1}$$

$$C_n^r := \frac{n!}{r!(n-r)!}. \tag{A.2}$$

C_n^r is the number of possibilities to choose r out of n objects depending on the order. (for more informations on the determination of the best χ^2-value, see Appendix D) The binomial distribution is normalized to one. The expectation value of the binomial distribution is [BL98]

$$\langle r \rangle = \sum_{r=0}^{n} r\mathrm{P}(r) = np. \tag{A.3}$$

The variance is given by

$$\mathrm{V}(r) = \sigma^2 = \sum_{r=0}^{n} (r - \langle r \rangle)^2 \cdot \mathrm{P}(r) = np(1-p). \tag{A.4}$$

The Poissonian Distribution

If a very large number of events $n \gg 1$ is observed and the probability p for the desired event to be observed is very small $p \ll 1$ and accordingly, the number of desired events that are observed is very small compared to the total number of events, the number of terms in the sum in Eq. A.1 becomes very large. Accordingly, it is desirable to describe the probability to observe exactly r out of n events by a

distribution that only depends on the expectation value instead of summing over all events [BL98]. The Poissonian distribution is often used in cases where rare events are counted, such as nuclear reactions or particle decays.
The Poissonian distribution is the limit of the binomial distribution for very large n and very small p. It is given by [BL98]

$$\mathrm{P}(r) = \frac{\mu^r \mathrm{e}^{-\mu}}{r!} \quad r = 0, 1, 2, ... \qquad , \tag{A.5}$$

μ is the mean value of the distribution. The Poissonian distribution is normalized to one. The expectation value equals the mean value

$$\langle r \rangle = \mu. \tag{A.6}$$

The same holds for the variance

$$\mathrm{V}(r) = \sigma^2 = np = \mu. \tag{A.7}$$

Probability Densities

The Normal Distribution

If a very large number of events n is investigated and the probability r is large to observe a desired event, the normal distribution[1] is used to describe the probability to observe the desired event exactly r out of n times. It can be understood as a probability density and is given by [BL98]

$$f(x) = \frac{1}{\sqrt{2\pi}\sigma} \mathrm{e}^{-\frac{(x-\mu)^2}{2\sigma^2}}, \qquad x \in (-\infty\,,\,\infty). \tag{A.8}$$

μ is the expectation value and σ^2 is the variance. The normal distribution is the limit of the binomial distribution for large n and r. Moreover, it is also the limit of the Poissonian distribution for large mean values μ.
The normal distribution plays a major role among all statistical distributions: According to the central limit theorem [BL98], the probability density of the sum $\mathrm{w}{=}\sum_{i=1}^{n} x_i$ of a sample consisting of n independent random variables x_i with arbitrary probability density, expectation value

$$\langle x \rangle = \int_{-\infty}^{\infty} x\, f(x)\, \mathrm{d}x, \tag{A.9}$$

and variance

$$\sigma^2 = V(x) = \int_{-\infty}^{\infty} \langle (x - \langle x \rangle)^2 \rangle\, f(x)\, \mathrm{d}x \tag{A.10}$$

always approaches a Gaussian probability density with mean value $\langle w \rangle = n \cdot \langle x \rangle$ and variance $\mathrm{V}(w){=}n \cdot \sigma^2$ in the limit $n \to \infty$.

[1] The normal distribution is also known as Gaussian distribution.

The χ^2-Distribution

The χ^2-distribution is a probability distribution that is important for statistical tests such as comparison of two datasets, comparison of a dataset and a theoretical model or comparison of different theoretical models. If x_1, x_2, ..., x_n are independent random variables that individually obey a Gaussian probability density with mean value 0 and variance 1, the sum $u = \chi^2$ of the squared values x_i [BL98]

$$u = \chi^2 = \sum_{i=1}^{n} x_i^2, \tag{A.11}$$

obeys a χ^2-distribution $f_n(u) = f_n(\chi^2)$ with n degrees of freedom. The probability density is given by

$$f_n(u) = \frac{\frac{1}{2}(\frac{u}{2})^{n/2-1}\mathrm{e}^{-u/2}}{\Gamma(n/2)}, \tag{A.12}$$

where $\Gamma(x)$ is the gamma-function that is defined as

$$\Gamma(x+1) = x! \quad . \tag{A.13}$$

Its expectation value is

$$\langle u \rangle = \langle \chi^2 \rangle = n, \tag{A.14}$$

and its variance is

$$\mathrm{V}(u) = \mathrm{V}(\chi^2) = 2n. \tag{A.15}$$

Appendix B

Convolution

If two values, x and y are random values with the corresponding probability densities $f_x(x)$ and $f_y(y)$, the sum $w = x+y$ is also a random value with the probability density $f_w(w)$ [BL98]. This combined probability density can be determined by convolving the probability densities $f_x(x)$ and $f_y(y)$. The convolution is defined as [BL98]

$$\begin{aligned} f_w(w) &= \int\int f_x(x)\, f_y(y)\, \delta(w-x-y)\, \mathrm{d}x\, \mathrm{d}y \\ &= \int f_x(x)\, f_y(w-x)\, \mathrm{d}x \\ &= \int f_y(y)\, f_x(w-y)\, \mathrm{d}y\,. \end{aligned} \tag{B.1}$$

If $f_x(x)$ and $f_y(y)$ are Gaussian distributions, the convolution can easily be calculated with the help of the characteristic functions ϕ_j: The characteristic function of a distribution is defined as the expectation value of e^{itx} [BL98], which is the Fourier transformation of $f_j(x)$, j=x,y

$$\phi_j(t) = \int_{-\infty}^{\infty} \mathrm{e}^{itj} \cdot f_j(j)\, \mathrm{d}j \qquad j \in \{x, y\} \tag{B.2}$$

The characteristic function $\phi_w(t)$ of the convolution of $f_x(x)$ and $f_y(y)$ is simply the product of the characteristic functions $\phi_x(t)$ and $\phi_y(t)$ [BL98]

$$\phi_w(t) = \phi_x(t) \cdot \phi_y(t). \tag{B.3}$$

This yields the characteristic function of a Gaussian distribution with variance $\sigma_w^2 = \sigma_x^2 + \sigma_y^2$.
Moreover, the characteristic function of the convolution of two Poissonian distributions can be determined by Eq. B.3. This yields the characteristic function of a Poissonian distribution with the mean value $\mu_w = \mu_x + \mu_y$.

Discrete Convolution

For discrete distributions, a convolution is possible by replacing the integral in Eq. B.1 by a sum. The discrete convolution then reads [IMT]

$$\begin{aligned} f_w(w) &= \sum_{k \in D} f_x(x)\, f_y(w-x) \\ &= \sum_{k \in D} f_y(y)\, f_x(w-y)\,, \end{aligned} \tag{B.4}$$

where D is the whole definition range of $f_x(x)$ and $f_y(w-x)$. In case of a limited definition range, $f_x(x)$ and $f_y(w-x)$ are usually continued by zero.

Appendix C

The χ^2-Test

The χ^2-method is a test to determine the accordance of data (for example resulting from a measurement) with a certain hypothesis.
A set of measured values, $y_1, y_2, ..., y_n$ is observed that depend on exactly known variables x_i (i=1,2,...,n) such that $y_i = y_i(x_i)$. In order to determine whether this set of variables is in accordance with a theoretical probability density $y_{th}(x)$, the theoretical expectation value $\langle y_{th}(x_i)\rangle$ is determined for every variable x_i individually. The expectation values are then compared with the measured values, investigating if both are in acceptable accordance within the error ranges. The testing parameter is defined as [BL98]

$$\chi^2 = \sum_{i=1}^{n} \frac{(y_i - \langle y_{th}(x_i)\rangle)^2}{\sigma^2_{th,i}} \,. \tag{C.1}$$

$\sigma^2_{th,i}$ is the variance of the theoretical distribution at x_i. If the y_i are normal distributed, χ^2 obeys a χ^2-distribution (as described in Appendix A) with n degrees of freedom. If the y_i's are numbers of events n_i, such that $n_i = y_i$, and $n_{th,i}$ is the theoretical mean number of events, the variance $\sigma^2_{th,i}$ becomes $\sigma^2_{th,i} = n_{th,i}$ according to the Gaussian approximation. Then χ^2 reads [BL98]

$$\chi^2 = \sum_{i=1}^{n} \frac{(n_i - n_{th,i})^2}{n_{th,i}}. \tag{C.2}$$

This can only represent a χ^2-distribution if the numbers $n_{th,i}$ are large enough ($n_{th,i} > 10$), so that the Gaussian approximation applies reasonably well [BL98].
The quantity that decides whether the set of measured values is in agreement with the theoretical distribution is the χ^2-value divided by the number of degrees of freedom m

$$\chi^2_m = \frac{\chi^2}{m} \,. \tag{C.3}$$

The 90 %- and 95 % confidence levels for different χ^2-values and for different numbers of degrees of freedom have been tabulated by various authors, e.g., in [PSY].

In order to determine the best χ^2-value, Eq. C.1 has to be minimized. This step is not always analytically possible.

Appendix D

Numerically Finding the Best χ^2

In chapter 4.3.2, the χ^2-method has been applied to find the optimum position of the theoretical ^{113}Cd spectrum $f_0^{th}(x_i)$ proposed by [MAS06] with respect to the spectrum that was measured by the colorless passivated COBRA detectors during 2009. In this case, finding the best χ^2 was not analytically possible (this problem was already mentioned in Appendix C). For this analysis, the best χ^2-value has been determined numerically. The only free parameter is the normalization of the theoretical curve. For the purpose of determining the best χ^2-value, the normalization of the theoretical spectrum has been approximated by using the same area A underneath the curve as the measured spectrum. The parameter b was then introduced to vary the normalization of the theoretical curve.

$$f_{th}(x_i, b) = b \cdot A \cdot f_0^{th}(x_i), \tag{D.1}$$

where $f_{th}(x_i, b)$ is the renormalized theoretical spectrum and b is the parameter that was varied between 0.5 and 2.5 in steps of 0.001. Figure D.1 shows the variation of the χ^2-values with respect to the varying parameter b. When all χ^2-values are plotted against b, a parabola appears that has a minimum at $b = 1.492$ for a χ^2 of about 7000. This minimum constitutes the best χ^2-value.

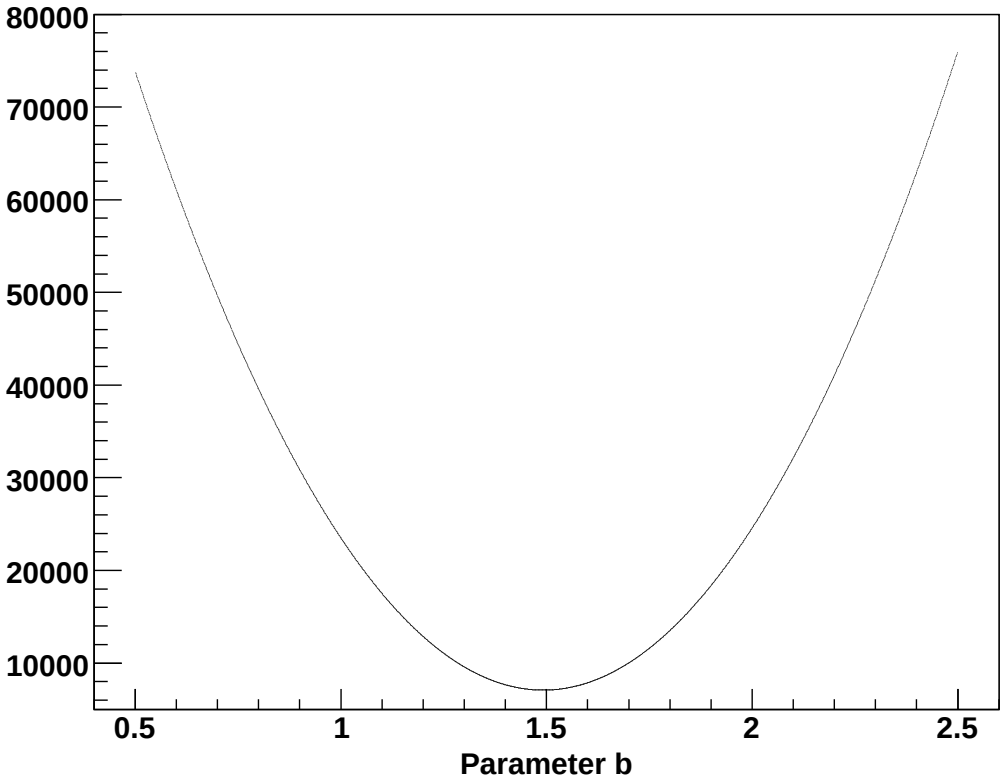

Figure D.1: Variation of the χ^2-value for varying normalization of the theoretical ^{113}Cd-spectrum. The spectrum has been normalized with the same number of events as the measured spectrum and then renormalized by a parameter b that was varied between 0.5 and 2.5 in steps of 0.001. The best χ^2-value coincides with the minimum of the parabola.

List of Figures

List of Tables

Bibliography

[AAA+01] Q. R. Ahmad, R. C. Allen, T. C. Andersen, J. D. Anglin, et al. Measurement of the rate of $\nu_e + d \rightarrow p + p + e^-$ interactions produced by ^8b solar neutrinos at the sudbury neutrino observatory. *Phys. Rev. Lett.*, 87(7):071301, Jul 2001.

[ABC+94] A. Alessandrello, C. Brofferio, D.V. Caminand, et al. Bolometric measurement of the beta spectrum of ^{113}cd. *Nucl.Phys.B Proc.Suppl.*, 35(80):394–396, 1994.

[ABD+87] Ugo Amaldi, Albrecht Böhm, L. S. Durkin, et al. Comprehensive analysis of data pertaining to the weak neutral current and the intermediate-vector-boson masses. *Phys. Rev. D*, 36(5):1385–1407, Sep 1987.

[ALE] http://aleph.web.cern.ch/aleph/aleph/newpub/physics.html.

[ARC] http://archiv.ub.uni-heidelberg.de/volltextserver/volltexte/2002/3005/pdf/04_KAPITEL4.PDF.

[AW93] G. Audi and A. H. Wapstra. The 1993 Atomic mass evaluation. 1. Atomic mass table. *Nucl. Phys.*, A565:1–65, 1993.

[B+07a] P. Belli et al. Investigation of beta decay of Cd113. *Phys. Rev.*, C76:064603, 2007.

[B+07b] T. Bloxham et al. First results on double beta decay modes of Cd, Te and Zn isotopes with the COBRA experiment. *Phys. Rev.*, C76:025501, 2007.

[BB36] H. A. Bethe and R. F. Bacher. Nuclear physics a. stationary states of nuclei. *Rev. Mod. Phys.*, 8(2):82, Apr 1936.

[BF07] T. R. Bloxham and M. Freer. Evaluation of pixellated CZT detectors for neutrinoless double beta-decay measurements. *Nucl. Instrum. Meth.*, A572:722–728, 2007.

[BJSJ98] Singh B., Rodriguez J.L., Wong S.S.M., and Tuli J.K. Review of logft values in beta decay. *Nuclear Data Sheets*, 84:487–563(77), July 1998.

[BL98] V. Blobel and E. Lohrmann. *"Statistische und nummerische Methoden der Datenanalyse"*. B.G. Teubner Stuttgart·Leipzig, 1998.

[CG98] C. Caso and A. Gurtu. The Z Boson: in Review of Particle Physics (RPP 1998). *Eur. Phys. J.*, C3:227–231, 1998.

[COB] http://cobra.physik.uni-dortmund.de.

[Col05] COBRA Collaboration. COBRA Progress Report 2005. 2005.

[Col06] COBRA Collaboration. COBRA Progress Report 2006. 2006.

[Col07] COBRA Collaboration. COBRA Public Report 2007. 2007.

[Col08] COBRA Collaboration. COBRA Public Report 2008. 2008.

[Col09] COBRA Collaboration. COBRA Progress Report 2009. 2009.

[Col10] COBRA Collaboration. LNGS Annual Report 2009, Sect: COBRA. 2010.

[D+09] J. V. Dawson et al. Experimental study of double beta decay modes using a CdZnTe detector array. *Phys. Rev.*, C80:025502, 2009.

[DFC+01] Guilhem Douysset, Tomas Fritioff, Conny Carlberg, Ingmar Bergström, and Mikael Björkhage. Determination of the ^{76}ge double beta decay q value. *Phys. Rev. Lett.*, 86(19):4259–4262, May 2001.

[DGG+62] G. Danby, J-M. Gaillard, K. Goulianos, et al. Observation of high-energy neutrino reactions and the existence of two kinds of neutrinos. *Phys. Rev. Lett.*, 9(1):36–44, Jul 1962.

[DGK+96] F.A. Danevich, A.Sh. Georgadze, V.V. Kobychev, et al. Beta decay of ^{113}cd. *Phys.At.Nucl*, 59(1):1–5, 1996.

[EHM87] S. R. Elliott, A. A. Hahn, and M. K. Moe. Direct evidence for two-neutrino double-beta decay in ^{82}se. *Phys. Rev. Lett.*, 59(18):2020–2023, Nov 1987.

[EIM] http://www.ams.unibe.ch/AMS_online/daten/mat_dent/2_wechselwirkungen.pdf.

[EVP] http://www.evmicroelectronics.com/pdf/material_prop.pdf, 2009.

[FC98] Gary J. Feldman and Robert D. Cousins. A Unified Approach to the Classical Statistical Analysis of Small Signals. *Phys. Rev.*, D57:3873–3889, 1998.

[FFI+01] S. Fukuda, Y. Fukuda, M. Ishitsuka, et al. Solar ^8b and hep neutrino measurements from 1258 days of super-kamiokande data. *Phys. Rev. Lett.*, 86(25):5651–5655, Jun 2001.

[Fur39] W. H. Furry. On transition probabilities in double beta-disintegration. *Phys. Rev.*, 56:1184–1193, 1939.

[G+97] M. Gunther et al. Heidelberg - Moscow beta beta experiment with Ge-76: Full setup with five detectors. *Phys. Rev.*, D55:54–67, 1997.

[GEA] http://geant4.cern.ch/.

[GER] http://www.mpi-hd.mpg.de/gerda.

[GJK+05] C. Goessling, M. Junker, H. Kiel, D. Muenstermann, S. Oehl, and K. Zuber. Experimental study of ^{113}cd β decay using cdznte detectors. *Phys. Rev. C*, 72(6):064328, Dec 2005.

[GM35] M. Goeppert-Mayer. Double beta-disintegration. *Phys. Rev.*, 48(6):512–516, Sep 1935.

[GM64] Murray Gell-Mann. A Schematic Model of Baryons and Mesons. *Phys. Lett.*, 8:214–215, 1964.

[Hei10] N. Heidrich. Diploma thesis: Monte-Carlo basierte Entwicklung einer Neutronenabschirmung fuer das COBRA-Experiment. 2010.

[Heu95] G. Heusser. Low-radioactivity background techniques. *Ann. Rev. Nucl. Part. Sci.*, 45:543–590, 1995.

[HME] http://www.klapdor-k.de/Theory of Experiments/HDMDBD/HeiMos.htm.

[HMO+94] M. Hirsch, K. Muto, Oda, et al. Nuclear structure calculations of beta+ beta+, beta+ / EC and EC / EC decay matrix elements. *Z. Phys.*, A347:151–160, 1994.

[Hos00] K. Hoshino. Result from DONUT: First direct evidence for tau-neutrino. 2000. Prepared for 8th Asia Pacific Physics Conference (APPC 2000), Taipei, Taiwan, 7-10 Aug 2000.

[ICC] http://icecube.wisc.edu/info/neutrinos/1989.php.

[IMT] http://www.imtek.de/emp/content/upload/vorlesung/2006/07_signal_mrm_zeitdiskrete_lti_systeme.pdf.

[IR49] Mark G. Inghram and John H. Reynolds. On the double beta-process. *Phys. Rev.*, 76(8):1265–1266, Oct 1949.

[KAE] http://atom.kaeri.re.kr/.

[Kie05] H. Kiel. Determination of the Half Lives of Rare Decays of Cd, Te and Zn Isotopes for the COBRA Experimentl. *PhD thesis, University of Dortmund*, 2005.

[KK87] H. V. Klapdor-Kleingrothaus. Proposal. *MPI-1987-V17*, 1987.

[KKDHK01] H. V. Klapdor-Kleingrothaus, A. Dietz, H. L. Harney, and I. V. Krivosheina. Evidence for Neutrinoless Double Beta Decay. *Mod. Phys. Lett.*, A16:2409–2420, 2001.

[KKK06] H. V. Klapdor-Kleingrothaus and I. V. Krivosheina. The evidence for the observation of 0nu beta beta decay: The identification of 0nu beta beta events from the full spectra. *Mod. Phys. Lett.*, A21:1547–1566, 2006.

[KKKDC04] H. V. Klapdor-Kleingrothaus, I. V. Krivosheina, A. Dietz, and O. Chkvorets. Search for neutrinoless double beta decay with enriched 76Ge in Gran Sasso 1990-2003. *Phys. Lett.*, B586:198–212, 2004.

[KMZ03] H. Kiel, D. Muenstermann, and K. Zuber. A search for various double beta decay modes of Cd, Te and Zn isotopes. *Nucl. Phys.*, A723:499–514, 2003.

[Koe] private communication with Tobias Koettig.

[Koe08] T. Koettig. Optimisation of Contacting and Energy Resolution of CdZnTe Detectors with Respect to Low Background Application. 2008.

[KSNS68] T. Kirsten, O. A. Schaeffer, E. Norton, and R. W. Stoenner. Experimental evidence for the double-beta decay of te^{130}. *Phys. Rev. Lett.*, 20(23):1300–1303, Jun 1968.

[Kuy05] F. Kuypers. *Klassische Mechanik*. WILEY-VCH Verlag GmbH & Co KGaA, Weinheim, 7 edition, 2005.

[Lan95] P. Langacker. Status of the standard model. *Nucl. Phys. Proc. Suppl.*, 38:152–163, 1995.

[Luk95] P. N. Luke. Unipolar Charge Sensing with Coplanar Electrodes - Application to Semiconductor Detectors. *IEEE Trans. Nucl. Sci.*, 42:207–213, 1995.

[MAJ] http://majorana.npl.washington.edu.

[MAS06] M. T. Mustonen, M. Aunola, and J. Suhonen. Theoretical description of the fourth-forbidden non-unique β decays of ^{113}cd and ^{115}in. *Phys. Rev. C*, 73(5):054301, May 2006.

[MAS07] M. T. Mustonen, M. Aunola, and J. Suhonen. Erratum: Theoretical description of the fourth-forbidden non-unique β decays of ^{113}cd and ^{115}in [phys. rev. c 73, 054301 (2006)]. *Phys. Rev. C*, 76(1):019901, Jul 2007.

[MK84] T. Mayer-Kuckuk. *"Kernphysik"*. B.G. Teubner Stuttgart, 4 edition, 1984.

[MNS62] Ziro Maki, Masami Nakagawa, and Shoichi Sakata. Remarks on the unified model of elementary particles. *Prog. Theor. Phys.*, 28:870–880, 1962.

[MS07] M.T. Mustonen and J. Suhonen. Microscopic quasiparticle phonon description of beta decays of ^{113}Cd and ^{115}In using proton neutron phonons. *Physics Letters B*, 657:38–42, November 2007.

[MS10] Mauro Mezzetto and Thomas Schwetz. Theta$_{13}$: phenomenology, present status and prospect. *J. Phys.*, G37:103001, 2010.

[Mue06] D. Muenstermann. Current status and recent results of the COBRA experiment. *PoS*, HEP2005:170, 2006.

[Mue07] D. Muenstermann. Construction of a Low Background Facility for the COBRA Experiment and its Performance. *PhD thesis, University of Dortmund*, 2007.

[N$^+$10] K. Nakamura et al. Particle Data Group. *J.Phys.G*, 37:075021, 2010.

[NA37] Seth H. Neddermeyer and Carl D. Anderson. Note on the nature of cosmic-ray particles. *Phys. Rev.*, 51(10):884–886, May 1937.

[NEM] http://www.imperial.ac.uk/research/hep/research/nemo2.gif.

[NUC] http://nucleardata.nuclear.lu.se/database/nudat/.

[P$^+$75] Martin L. Perl et al. Evidence for anomalous lepton production in e+ e- annihilation. *Phys. Rev. Lett.*, 35:1489–1492, 1975.

[Pau78] W. Pauli. Dear radioactive ladies and gentlemen. *Phys. Today*, 31N9:27, 1978.

[Pon58] B. Pontecorvo. Inverse beta processes and nonconservation of lepton charge. *Sov. Phys. JETP*, 7:172–173, 1958.

[PRSZ06] B. Povh, K. Rith, C. Scholz, and F. Zetsche. *Teilchen und Kerne. Eine Einfuehrung in die physikalischen Konzepte.* Springer-Verlag GmbH, 7 edition, 2006.

[PSY] http://psydok.sulb.uni-saarland.de/volltexte/2004/268/html/chivert.htm.

[RA00] G. W. Rodeback and J. S. Allen. Neutrino recoils following the capture of orbital electrons in A-37. *Camb. Monogr. Part. Phys. Nucl. Phys. Cosmol.*, 14:28–37, 2000.

[RC56] Frederick Reines and Clyde L. Cowan. The neutrino. *Nature*, 178:446–449, 1956.

[Ree09] C. J. Reeve. Data Analysis and Background Studies for the COBRA Neutrinoless Double-Beta Decay Experiment. *PhD thesis, University of Dortmund*, 2009.

[Ros] S. P. Rosen. MASS LIMITS ON MAJORANA NEUTRINOS FROM DOUBLE BETA DECAY. (TALK). Presented at the Workshop on Neutrino Mass: Cosmological, Theoretical and Experimental Considerations, Cable, Wisc., 2-4 Oct 1980.

[Sch97] Norbert Schmitz. Neutrinophysik. (22A9106), 1997.

[Sci79] F. Sciulli. AN EXPERIMENTER'S HISTORY OF NEUTRAL CURRENTS. *Prog. Part. Nucl. Phys.*, 2:41, 1979.

[SFM09] F J P Soler, Colin D Froggatt, and F. Muheim. *Neutrinos in particle physics, astrophysics and cosmology.* Scottish Graduate Series. CRC Press, Boca Raton, FL, 2009.

[SKD] http://www-sk.icrr.u-tokyo.ac.jp/sk/index_e.html.

[SV82] J. Schechter and J. W. F. Valle. Neutrinoless double-β decay in su(2)×u(1) theories. *Phys. Rev. D*, 25(11):2951–2954, Jun 1982.

[TOI] http://ie.lbl.gov/.

[VEN] http://internal.cobra-experiment.org/venom/index.html.

[Wei35] C. F. V. Weizsacker. Zur Theorie der Kernmassen. *Z. Phys.*, 96:431–458, 1935.

[WS54] Roger D. Woods and David S. Saxon. Diffuse Surface Optical Model for Nucleon-Nuclei Scattering. *Phys. Rev.*, 95:577–578, 1954.

[Zub] private communication with Kai Zuber.

[Zub01] K. Zuber. COBRA: Double beta decay searches using CdTe detectors. *Phys. Lett.*, B519:1–7, 2001.

[Zub04] K. Zuber. *Neutrino Physics*. Series in High Energy Physics, Cosmology and Gravitation. Institute of Physics, 2004.

[Zub10a] K. Zuber. Status of the COBRA double beta decay experiment. *J. Phys. Conf. Ser.*, 203:012070, 2010.

[Zub10b] K. Zuber. The status of the COBRA double-beta-decay experiment. *Prog. Part. Nucl. Phys.*, 64:267–269, 2010.

Danksagung

Zuerst möchte ich mich bei allen Menschen bedanken, die mich fachlich oder mental im Rahmen dieser Diplomarbeit unterstützt haben.
Mein besonderer Dank gilt:

- Frau Prof. Dr. Caren Hagner für die Betreuung, die wertvollen Diskussionen, die mein Verständnis der Kernphysik verbessert haben und natürlich für die Möglichkeit, an diesem interessanten Thema in ihrer Arbeitsgruppe arbeiten zu dürfen,

- Herrn Prof. Dr. Walter Schmidt-Parzefall für diverse Anregungen, die wesentlich die Qualität dieser Arbeit verbessert haben, insbesondere was die Diskussion des ^{113}Cd-Spektrums betrifft, und natürlich für die Übernahme des Zweitgutachtens dieser Arbeit,

- Herrn Prof. Dr. Kai Zuber für viele Anregungen bezüglich meiner Arbeit und für seinen großen Enthusiasmus bezogen auf das COBRA Experiment.

Darüberhinaus möchte ich mich bei der gesamten Arbeitsgruppe Neutrinophysik für die tolle Atmosphäre während der Arbeit bedanken, besonders auf Konferenzen, für regelmäßige Kuchenspenden, diverse lustige Abende und sehr nette und hilfreiche fachliche wie auch private Gespräche. Insbesondere bedanke ich mich bei:

- Christian Oldorf für die Betreuung meiner Arbeit, diverse Anregungen, die angenehmen Meetings und Workshops in Bonn, Prag, Dortmund und Erlangen und deren Organisation sowie das Korrekturlesen meiner Arbeit,

- Dr. Björn Wonsak für wertvolle fachliche Diskussionen, insbesondere bezogen auf Statistische Methoden der Datenanalyse und das Korrekturlesen meiner Arbeit, aber auch für ein sehr spaßiges "Kicker-Turnier" und die ebenso spaßige Vorbereitung darauf,

- "Dem Mädchenbüro" in der alten Konstellation bestehend aus Nadine Heidrich, Annika Hollnagel und Nina Cords für sehr viel Hilfe mit Linux, Root und C^{++}, für sehr viele nette Gespräche, diverse "Obstpausen" und Unmengen an Schokolade,

- Dem "Flodderbüro" bestehend aus Annika Hollnagel und Horsti (Jan Timm) für ebenfalls sehr nette Gespräche, noch mehr "Obstpausen" und noch mehr Schokolade und das Verständnis beim Zusammenschreiben meiner Arbeit,
- Annika Hollnagel für viele amüsante Spieleabende und Shopping-Touren,
- Martin Hierholzer und Daniel Bick für ihre große Hilfe mit allen möglichen Computerproblemen,
- Jan Lenkeit für das Korrekturlesen meiner Arbeit und für das Instandhalten unserer "Snackbox"– ohne die ich sicher verhungert wäre,
- Torben Ferber für fachliche Hilfe mit Erhaltungsgrößen und sein immenses Wissen zum Thema Gesundheit und Fitness,
- Christoph Göllnitz für viele Lacher und Seifenblasen,
- Hajo (Hans-Jürgen Ohmacht) für seinen positiven Einfluß auf den Zusammenhalt der Gruppe (besonders bei den Kicker-Abenden),
- Volker Braunert für viele kommunikative Tee-Pausen.

Desweiteren bedanke ich mich ganz herzlich bei der gesamten COBRA Kollaboration für zwei tolle Kollaborationstreffen in sehr freundschaftlicher Atmosphäre, welche mein Verständnis des experimentellen Aufbaus und des aktuellen Status' des COBRA Experiments verbessert haben, die tollen Gespräche, fachlicher wie auch privater Natur, und die überaus großzügige Verpflegung. Besonders danke ich:

- Tobias Köttig aus Dortmund für sehr viel Hilfe mit Root, dem COBRA Experiment allgemein, für die Erstellung von Simulationen, welche für diese Arbeit nötig waren und für seinen besonderen Beitrag zur heiteren Stimmung auf den Kollaborationstreffen,
- Oliver Schulz für die Hilfe mit meinen IT-Problemen im Dortmunder Netzwerk und für tolle Gespräche auf den Kollaborationstreffen.

Ein besonderer Dank gilt meiner Familie und meinen Freunden, die während der ganzen Zeit meines Studiums nie die Geduld mit mir verloren haben und immer an mich glaubten. Insbesondere danken möchte ich meiner Mutter für ihre Liebe, ihr großes Verständnis und ihre Geduld mit mir, vor allem in den letzten Jahren meines Studiums und dafür, dass sie mich in Momenten der Verzweiflung ermutigt hat nicht aufzugeben. Natürlich möchte ich mich auch für ihre finanzielle Unterstützung bedanken, ohne die mein Studium nie möglich gewesen wäre. Außerdem gilt ein besonderer Dank meinem Bruder Peti, der mich sehr oft mit seinem "Halt die Ohren steif" ermutigt hat und der in vielen Telefongesprächen sehr zur Erheiterung von mir und meinen Bürokollegen beigetragen hat. Außerdem möchte

ich meinem Vater danken, denn er hat mir die Physik im Kindesalter nahe gebracht und obwohl er viel zu früh gegangen ist, hat mir seine Liebe die Kraft gegeben weiterzumachen.
Unter meinen Freunden möchte ich besonders Janna Koch danken für so viele aufmunternde Abende, die mir viel Kraft gegeben haben und für ihr riesiges Verständnis für mich und dafür, dass ich insbesondere die letzten Monate so wenig Zeit für sie hatte. Außerdem danke ich Gabriele Swoboda und Fabian Reichert für viele aufmunternde Worte und eine wahnsinnig schöne Studienzeit, die mit niemand anderen hätte schöner sein können.
Ein besonderer Dank gilt meinem Freund Stellan, der mir mit seinem Verständnis und seiner unendlichen Liebe so viel Kraft gegeben hat und immer an mich glaubte, wenn mich der Mut verließ.

Hiermit versichere ich, die vorliegende Arbeit selbständig und ausschließlich mit den angegebenen Quellen und Hilfsmitteln verfasst zu haben.
Mit der Veröffentlichung dieser Arbeit und der Auslage in der Bibliothek bin ich einverstanden.

Hamburg, November 29, 2010

Stefanie Kietzmann